IN VIVO SERIAL PATCH CLAMP ROBOTICS FOR CELL-TYPE IDENTIFICATION IN THE MOUSE VISUAL CORTEX

A Dissertation
Presented to
The Academic Faculty

by

Gregory Leonard Holst

In Partial Fulfillment
Of the Requirements for the Degree
Doctor of Philosophy in Bioengineering

Georgia Institute of Technology

December 2016

IN VIVO SERIAL PATCH CLAMP ROBOTICS FOR CELL-TYPE IDENTIFICATION IN THE MOUSE VISUAL CORTEX

Approved by:

Professor Craig R. Forest, Advisor
George W. Woodruff School of Mechanical Engineering
Georgia Institute of Technology

Professor Todd Sulchek
George W. Woodruff School of Mechanical Engineering
Georgia Institute of Technology

Professor Edward S. Boyden
Media Arts and Sciences
Massachusetts Institute of Technology

Dr. Hongkui Zeng
Department of Structured Science
Allen Institute for Brain Science

Professor Garrett B. Stanley
Coulter Department of Biomedical Engineering
Georgia Institute of Technology and Emory University

Professor Suhasa B. Kodandaramaiah
School of Mechanical Engineering
University of Minnesota

Date Approved: December 16th 2016

To my loving wife Sarah,

and my precious daughters Lily, Rielle, and Marina.

ACKNOWLEDGEMENTS

This work is a result of the mental energy, passion, and vision of a team of colleagues and advisors who generously contributed their time and resources to support me throughout the project. First, I express my sincere gratitude to my advisor Prof. Craig Forest whose tireless efforts and sincere attention have provided the vision and the means for the success of this work. Much more than an academic advisor, he has also been a mentor, counselor, and a true friend.

Professor Ed Boyden and Dr. Hongkui Zeng have also been instrumental in guiding the direction of the project by contributing the vision of transforming the field from a highly experimental science into an informatic one through automation, and guiding our work to focus on the unsolved role of cells in layer 5 of the visual cortex. I'd also like to thank Dr. Zeng for hosting us in Seattle between May and December of 2014 where I received the essential training in surgical technique and advanced patch clamp electrophysiology that enabled the *in vivo* validation of the robot.

Professors Todd Sulchek and Garrett Stanley also generously contributed their time and unique perspectives to help focus and refine the aims of the project.

Thank you to Prof. Suhasa Kodandaramaiah who, as a fellow graduate student when I joined the lab, trained me in patch clamp experimentation and first envisioned the value of a fully-automated patch robot. His continuous advising and mentoring throughout the course of the project were critical to its success.

I'd also like to my fellow members of the Precision Biosystems Laboratory who were always available to help: Dr. Chris Phaneuf who taught me to use the CNC mill, Dr. Melissa Li, Dr. Nathan Hotaling, Curtis Saunders, Nikita Pak, Michael McKinnon, Caitlin Austin, Timothy Lee, Thomas Capocasale, Scott Thourson, Dan

Russakow, Mike Simpson, and Corey Laundry. Special mention also goes to William Stoy and Ilya Kolb who's skillful assistance, insightful advise, and optimism helped cheer me on through the hard times. Also, thank you to Bo Yang who performed many of the surgeries and whose keen insights helped make sense of the recordings.

In the Synthetic Neurobiology Group, Dr. Ian Wickersham and Prof. Annabelle Singer, and collaborators at the Allen Institute, Dr. Tim Jarskey, Dr. Jack Waters, Dr. Clay Reid, Dr. Severin Durand, Dr. Jim Burg, Dr. Peter Ledochowitsch, Dr. Adam Shai, Dr. Brain Lee, Dr. Johnathan Ting, and Dr. Soumya Chatterjee, all gave freely of their limitless expertise and experience. In particular, Dr. Lu Li, and Dr. Ulf Knoblich were patient mentors in surgical technique and electrophysiology, and Dr. Stacey Sorenson who performed several morphological analyses in connection with this work.

There were also a number of undergraduate researchers who contributed directly to the aims herein. Jamison Go, Coby Lu, and Aaron Fan developed the first prototypes of the fully-automated robot as their capstone design project and Max Stockslager, Thomas Capocasale, Michael Simon, Yuanda Li, and Dustin McGruder implemented the automated pipette inspection system for their capstone project. Cam Phillips, Andy Lustig, and Sage Duddleston contributed to the design and manufacturing of the custom Faraday cage, commercial pressure control system, and the compact automated pipette holder.

The expertise and drive of David Moeller were critical for commercial dissemination of the pressure control system to the community and I thank him for generously involving me in the process.

I am also grateful to the sacrifice and trust of the American people whose support through an NSF Integrative Graduate Education and Research Traineeship, various NIH grants, and the Georgia Tech Foundation provided the funding to enable this work.

I thank my parents, Shane and Mary, for their sacrifice and unfailing love, support, and confidence in me.

Finally, along with my deepest and most heartfelt gratitude, I dedicate this work to my wife Sarah, who has patiently suffered through nearly seven and a half years of graduate school while raising our three daughters and single-handedly managing our home. My undying love, devotion, and loyalty could never compare with the sacrifices she has made to allow me to follow my dream of pursuing a PhD. Her unfailing hope, optimism, grit, and love have been my mainstay during stormy times and she is a joy to my life forever.

I also dedicate this work to my children, Lily, Rielle, and Marina who bring a sweetness and a sparkle to life that nothing else can.

TABLE OF CONTENTS

LIST OF TABLES

LIST OF FIGURES

SUMMARY

Our ability to probe the immense complexity of the brain, with its approximately 80 billion neurons, is currently limited by the available tools to record and modulate neural activity within intact, functioning, neural circuits. We have yet to develop a complete catalog of all the types of neurons and their basic functions, and to identify the root causes of most nervous system disorders. To achieve a full understanding of the fundamental principles behind brain function, new tools must be developed to increase scale, resolution, and efficiency of neural recording.

Here we show the development of robotics tools to investigate the unique behaviors of cell types in layer 5 of the visual cortex of mice and transform the highly manual art of obtaining patch-clamp electrophysiological recordings *in vivo* into a systematic, automated procedure. The patch clamp technique is the current gold standard for recording the intracellular electrical activity of individual cells and has the highest resolution and specificity of any other technique. However, the manual methods used to control the position, pressure, and voltage of the glass recording pipette severely limit the throughput and the ability to perform multiple simultaneous recordings in vivo. This work shows the development of automation systems to precisely and repeatably prepare the recording pipette, position it in the brain, establish the recording, and conduct an entire electrophysiological experiment all without requiring the presence of a human operator. The robot has autonomously obtained multiple, consecutive recordings *in vivo* with the same quality and throughput as a highly-skilled human operator. Robotic hardware and software algorithms enable

parallel scaling for increased throughput, systematic operation, and rapid dissemination of challenging techniques. These tools will increase our capacity to rapidly identify new cell-type classification schemes across entire brain regions and discover the *in vivo* function and dysfunction of cells within the nervous system.

CHAPTER 1

INTRODUCTION

1.1 Motivation

The human brain contains over 80 billion neurons and 150 trillion synapses that together orchestrate our ability to think and sense the external world, form the basis of memory and consciousness, and are affected by a host of neurological and psychiatric disorders. Critical to increasing our understanding of the function and dysfunction of these cells are the technology and instrumentation we use to explore the anatomy, signal processing, and molecular biology of the living brain.

Since the discovery of electrically active cells by Luigi Galvani in 1791, scientists have used a wide array of equipment to understand the mystery of biological signal transmission and processing [118]. Galvani applied charges to exposed nerves using simple wiring and an "electric machine" eliciting muscle contractions in frogs. Galvani was one of the first electrophysiologists, someone who uses electrical engineering principles and systems to study the physiology of the nervous system. The modern equivalent of Galvani's experiments is the BackyardBrains project that has developed the hardware to allow non-scientists to wirelessly steer a cockroach by stimulating the nerves of its antennae to redirect its motion. The study of electrophysiology has led to groundbreaking advancements in medicine, including the treatment of paralysis from traumatic injury, determining the causes of neurodegenerative diseases, and the discovery of fundamental mechanisms behind neural processing. This success has spurred the development of new scientific tools and clinical treatments including cochlear implants to treat hearing loss, deep brain stimulation electrodes for addressing the symptoms of Parkinson's disease, implanted retinal electrode arrays to

treat blindness, pacemakers, and brain computer interfaces that allow quadriplegics to control physical and virtual systems. An entirely new field of therapeutics has been founded, electroceuticals, and will continue to have significant impact for individuals with nervous system disorders. This field is supported by the knowledge and experience of scientists who, for over 200 years, have been making the critical discoveries that allow engineers to design systems that target and compensate for nervous system deficiencies.

The tools for basic scientific discovery that form the foundation of the therapeutic work have also improved dramatically since Galvani's first discoveries. Edgar Adrian in 1926, used a capillary electrometer [3] as a custom amplifier to record some of the first millivolt signals within the nervous system. Later the use of glass microelectrodes to study pyramidal cells in the cortex was pursued by Renshaw et. al. [123] allowing the signals from individual neurons to be isolated from neighboring cells. Throughout the history of neuroscience, we see the resourcefulness and ingenuity of scientists as they apply emerging technology to solve major bioinstrumentation challenges. This culture among neuroscientists has driven a technological revolution in recent years where the development of molecular, imaging, electrical, and mechanical tools has enabled unprecedented control of experimental conditions and new breakthrough recording and stimulation modalities [22, 53, 48, 4]. These technologies enable scientists to stimulate neurons using ultra-precision microfabricated electrodes [127], allows robotic manipulation of glass electrodes for single cell recordings [69], enables heat-induced voltage control using magnetic fields [21], and even the ability to control the voltage within cells using light [12, 53]. The same microfabricated electrodes can be used to record from 500+ cells [128] while novel imaging modalities can record from 200+ cells simultaneously *in vivo*, 1000+ *in vitro* [135, 38] in a non-contact fashion.

Ultimately, the goal of deciphering the inner workings of the brain can only be

accomplished by developing new technologies that continue to increase the number of neurons that can be recorded simultaneously to build a complete map of brain activity (Brain Activity Map [5, 133]). Because of the highly parallel and highly interconnected nature of the brain, where a single cell can have over 1000 connections, it would be very difficult to reconstruct the function and role of an individual neuron if only a subset of the network is being recorded. With the proper tools, analyzing the brain could become as simple as using a logic analyzer to characterize the behavior of common digital circuits, but we are still far from this goal. In 2013, President Barack Obama enacted the Brain Initiative to fund the development of new tools that could meet this goal of simultaneously recording from every neuron in the brain. "If [the] exponential growth [Moore's Law] were to continue, future electrophysiologists would be able to record from all of the approximately 100 billion neurons in the human brain in 220 years" [133].

The usefulness of a complete map of neural activity cannot be overstated. In engineering we commonly refer to the work of Newton, Navier-Stokes, Euler, Laplace, Nyquist-Shannon, Ohm, and Maxwell who developed the fundamental equations and laws used to predict the behavior physical systems. To date, we still do not have the fundamental understanding of the physical laws that would enable us to predict the behavior of neurons in networks of more than a few cells. Our lack of understanding is one of the main limitations on our ability to design new treatments for addiction, injury, and disease. Using the map, we will be able to distill down, isolate, and accurately describe the laws that govern neural processing. With all the necessary fundamental laws and simplifying assumptions, designing a neural therapeutic could become as simple as it is to use the laws of thermodynamics to design an efficient air conditioner. It will likely include a mix of deterministic laws such as the Hodgkin-Huxley model as well as stochastic characterization to describe the variability within biological systems. Engineering genetic algorithm optimization is one example of a

system that incorporates this variability as an essential part of its function, and the same may hold true for neural activity. As we seek to understand the unchanging laws in neural network processing and single-cell computation, perhaps it is also essential to examine the variability and identify the laws that govern it [146]. In numerically modeled networks, for example, injecting variability is an essential part of achieving realistic behavior, but its role remains a mystery [2].

This aim of this thesis is to help scientists pursue the goals of recording from every cell simultaneously, determining the governing laws of neural networks, and developing new therapeutics, by discovering and implementing new automated techniques that address the challenges of recording from single cells in living, functioning, tissue. The following sections will first describe the patch clamp technique in detail, which is the focus of the current work, and provide short descriptions of the extracellular recording technique, voltage sensitive dyes, calcium indicators, and "sharps" recordings to provide a comparison of their respective advantages and disadvantages.

1.2 Comparison of Single-Cell In Vivo *Neural Recording Techniques*

1.2.1 The Patch Clamp Method

Invented by Nehr and Sakmann [126] in the 1980s, patch-clamp recording [47] quickly became the gold standard technique for measuring transmembrane voltages and intracellular currents in individual, electrically excitable cells such as neurons and cardiac cells. Its popularity is due to its unique ability to resolve not only the high-amplitude voltage spikes that occur during an action potential (AP), but also the minute millivolt changes that occur during synaptic signal signaling between connected cells [98, 15]. The cell integrates these synaptic inputs and generates an AP if the voltage increases above a certain threshold within the cell. The dynamics of these synaptic events, and neuronal activity in general, are implicated in many neurological diseases [138] and are studied extensively in brain slices [92] and *in vivo* [115]. It is also widely used for

basic research and for validating emerging methods for recording and stimulating cells [12, 119, 10, 19]. It receives its name from the interaction between the tip of the glass recording electrode and a small patch of cell membrane. It involves delicately resting a 1 µm diameter pipette tip against the cell to create a tight mechanical connection between the pipette tip and the cell membrane that also has high electrical isolation from the surrounding environment (>1 GΩ). In this configuration, it is possible to record the millivolt changes in voltage within a single neuron without environmental interference or crosstalk. It also enables physical access to the intracellular space to inject plasmids, dyes, voltage indicators, or to extract the intracellular contents, such as mRNA transcripts, which enables multiple analyses to be performed on the same cell [87, 122] critical for building descriptions of different cell types based on the combined correlation of their electrophysiological, morphological, and transcriptional properties.

The method to record intracellular voltages using patch clamping requires rupturing the patch of membrane covering the tip of the pipette after forming the 1 GΩ seal with the cell membrane. This allows access to the intracellular space while maintaining the seal between the membrane and the walls of the pipette (see whole-cell in Figure 1). This is the *whole-cell* configuration which is one of the most commonly used and will be the focus of this work. Other configurations such as inside-out or outside-out patch allow measuring currents through the patch of membrane itself, rather than from entire cell, to characterize the dynamics of a few or even individual ion channels embedded in the cell membrane. With this technique, the dynamics of individual ion channels can be isolated and studied [126, 47]. These configurations are obtained by retracting the pipette from the cell after forming the seal and then recording from the patch of membrane covering the tip of the pipette. Figure 1 shows these other configurations in more detail.

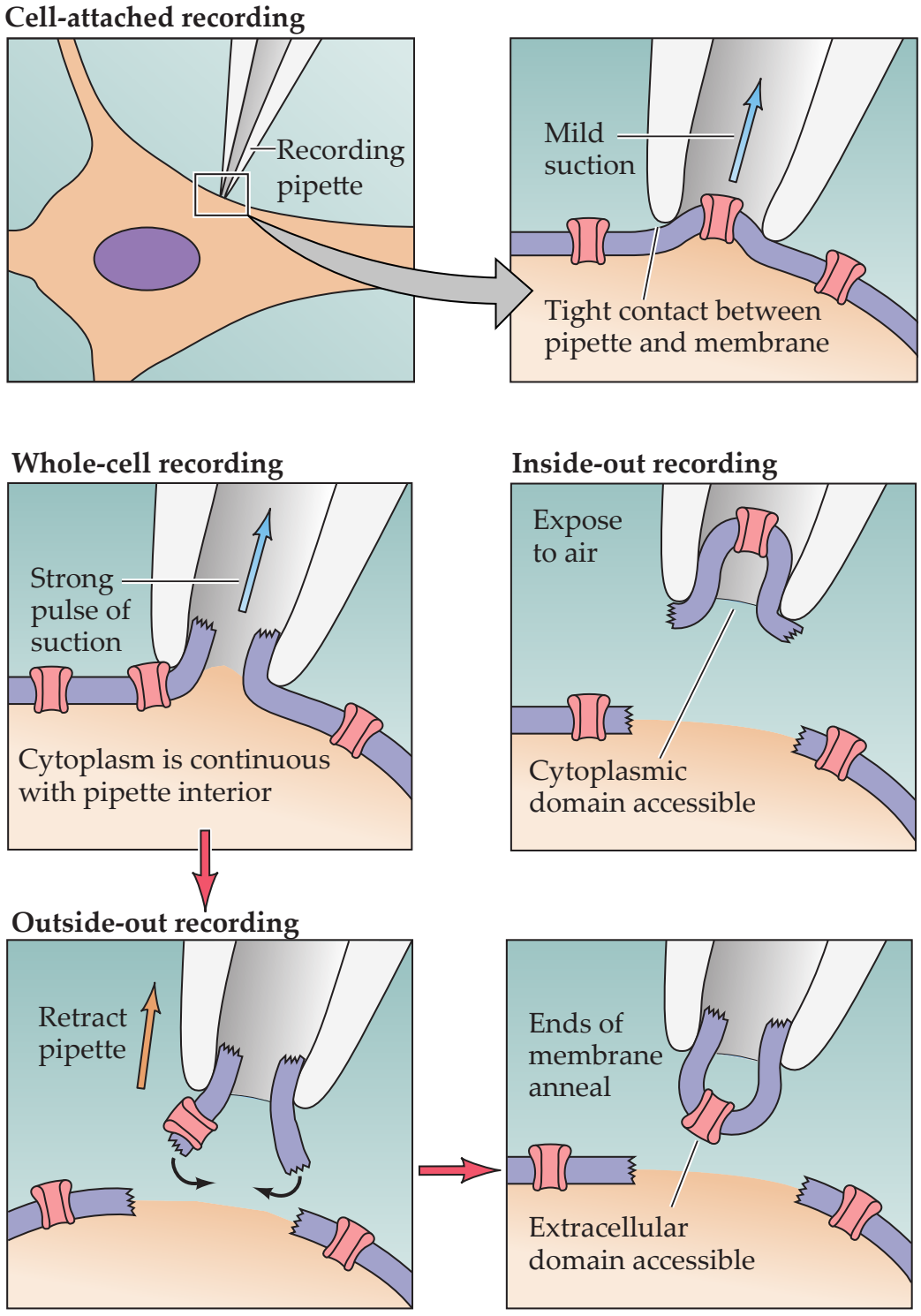

Figure 1: Four different configurations for patch clamp measurements of ionic currents. Reproduced from [121]. Copyright 2004, Sinauer Associates, Inc. Sunderland, Massachusetts USA.

Whole-cell recordings are widely used in cultured HEK cells, neurons, and cardiomyocytes, as well as in intact slices of neural tissue. The technique has also been extended to record from cells in *in vivo* in anesthetized animals [80, 71, 83, 67], awake head-fixed animals [100, 28, 111, 106, 143], and more recently, freely moving animals [79, 80] with unmatched recording quality.

The exquisite specificity and resolution of the patch clamp technique is offset by the difficulty and skill required to establish and maintain the recording, especially *in vivo*. Most *in vivo* electrophysiologists spend years training to learn what is considered the art of *in vivo* patch clamp. Quality recordings require exquisite surgical preparation, quality pipette microfabrication, precise biochemical preparation, manual dexterity and visual acuity. The combination of these challenges, their manual nature, and the inherent low yield limits the impact of this method in the field. However, despite these challenges, the field continues to publish widely using this technique. Until very recently, it was only possible to record from a single neuron *in vivo* using this technique in contrast to the improvements in extracellular and imaging methods that can now record from 100s of cells *in vivo*. The patch clamp recording technique will need to overcome significant challenges in order to contribute to the brain activity map at a level similar to the other methods. The primary limitation is the dependence on a human operator to physically, pneumatically, and electrically manipulate the glass recording pipette during an attempt. Secondary limitations that restrict the theoretical maximum number of cells that could be recorded simultaneously are the physical interference between multiple pipettes inserted into the brain, and the low success rate (20%). Up to 12 simultaneous recordings have been performed *in vitro* where the success rates are much higher (>80%) and the recordings are much more stable. This allows a human operator to serially manipulate each pipette and establish the recording before the previous recordings fail. *In vivo*, the recording durations are shorter and happen less frequently due to tissue motion so a

parallel approach is essential. However, the mental and physical requirements placed on a human operator prevents them from manipulating multiple pipettes simultaneously. Potentially, if the human were replaced by automated approaches, the only limitations would be low yield, the physical constraints, and cost. Recent progress is being made, however, to significantly reduce the cost of the amplifiers [48].

The process of obtaining a patch clamp recording begins by heating the center of a 1.5 mm diameter glass capillary using a platinum filament and pulling the ends of the capillary once the glass has softened causing the glass to neck down and separate into two pipettes. The pipette has a 3 mm long taper and 1 µm diameter tip (more details in Section 5.3.3). The pipette is then filled with fluid that is prepared so that it matches the internal chemistry of the cell. The pipette is threaded into a pipette holder and a silver wire is inserted inside the pipette and submerged into the fluid to provide an electrical connection with the amplifier. The pipette holder also forms a pneumatic seal with the pipette so that the pressure can be controlled which controls fluid flow out of the tip of the pipette. The pipette is placed under high positive pressure and positioned just above the surface brain that has been surgically prepared (see Section 5.3.1). The pipette is then inserted into the brain to the depth of interest, typically between 100 and 1500 µm. The high positive pressure ejects a plume of fluid during this step that prevents debris from the extracellular space, axons, dendrites, and glial cells, from contaminating the tip of the pipette. Once at depth, the pressure is lowered to maintain the cleanliness of the tip but allows the soma of the neuron to come in contact with the tip. The neuron hunting stage is then begun where the pipette is lowered in small steps (2 µm) and the electrical impedance of the tip of the pipette is closely monitored. This is measured by injecting a voltage square wave (20 mV) through the tip and the current is measured. If the amplitude of current passing through the pipette decreases more than 10-50%, this indicates that the tip of the pipette is being blocked, often by a cell membrane. At this point,

the motion of the pipette is halted and the positive pressure is released which will allow the membrane to make contact with the tip of the pipette and form the seal. Once the seal reaches an electrical impedance >1 GΩ, a brief pulse of suction causes the patch of membrane covering the tip of the pipette to rupture and connecting the inside of the pipette with the cytoplasm of the cell while maintaining contact between the membrane and the pipette. At this point, current may be injected to stimulate the cell, or currents passing through the membrane due to synaptic activity and APs and be recorded with high fidelity.

While the above process is the ideal, the pipette can still be clogged by debris, it may not find a cell in the region of interest, or fails to form a quality seal with the membrane. Tissue motion can disrupt the process and can also damage the recording even after successfully establishing. If the cell and pipette drift apart or too close together, this can degrade the quality of the recording by increasing the resistance between the fluid in the pipette and the cytoplasm, known as access resistance, or the seal can be damaged allowing the currents within the cell to leak between the pipette and the extracellular space, reducing the health of the cell and recording resolution. *In-vivo* whole-cell recordings can be quite stable despite these challenges [100, 79], but require significant effort to achieve and are still rare in literature compared to other techniques.

1.2.2 Sharps Recordings

Sharps recordings are similar to patch clamp in that they also use a glass micropipette although with a much smaller tip (70-200 nm, 10-500 MΩ). Rather than forming a seal with the membrane, the small tip is simply inserted into the cell and the currents recorded directly. Sharps electrodes are simple to insert, allow multiple serial insertions, and still allow molecular access to the cytoplasm. Cells can also have a good survival rate when retracted [83] for morphological reconstruction. However,

without forming a seal between the membrane and the pipette, the health of the cell quickly degrades due to a leak between the pipette and the membrane. This significantly reduces the recording duration *in vivo* (<10 min) where tissue motion easily disrupts the recording [34]. The resolution of sharps recordings is similar to patch clamp but the access resistance due to a high pipette resistance and the reduced isolation from the leak make it more difficult to obtain accurate measurements of the membrane voltage and currents. When sharps electrodes are inserted into the cell the spiking activity is largely unaffected by the additional leak currents but it does cause drift in the resting membrane potential of the cell when compared to patch clamp recordings [83]. This technique is optimal for preliminary studies in areas where it is difficult to obtain patch recordings and when high-resolution spiking activity is the feature of interest and single-cell morphological reconstructions are desired.

1.2.3 Extracellular Electrodes

Extracellular recordings involve inserting a sharp conductive object into the brain to record currents in the extracellular space. Modern microfabrication techniques have enabled scientists to record from hundreds of cells simultaneously by densely arranging multiple recording sites on a single electrode, in sharp contrast to the single cell ability of patch clamp electrodes [127]. Extracellular electrodes also have the advantage that they are easily inserted into the brain, instead of the complicated failure-prone patch clamp technique where attaching the electrode to the cell of interest is much more difficult, particularly *in vivo*. However, due to the lack of the isolation between the extracellular electrode and the cell, the amplitude of signals are in the microvolt range and cannot resolve subthreshold activity. Sorting signals from neighboring recording sites remains a major challenge when attempting to differentiate between signals from individual or multiple cells [82].

1.2.4 Voltage Sensitive Dyes

Scientists also employ high-speed fluorescence microscopy methods combined with voltage sensitive dyes (VSD) to monitor intracellular voltage [19, 7]. While it has the advantage of being non-contact method and can record from thousands of cells simultaneously, VSD recordings suffer from poor signal to noise when compared to patch clamp recordings, particular at depths greater than 500 µm where optical scattering and tissue motion *in vivo* reduce the resolution. Photobleaching and can also affects the signal integrity and the indicators can be toxic to the cell. VSD indicators do effectively transduce action potentials and subthreshold voltages [60, 119, 37, 16, 35, 117] but with lower sensitivity.

1.2.5 Calcium Indicators

Calcium indicators, whether dyes or genetically encoded, suffer from the same optical limitations of limited frame rate acquisition, light scattering, and photobleaching, as VSDs but they can effectively transduce action potentials (calcium dyes [7], genetically encoded calcium indicators [14, 103, 108]). However, they are unable to resolve subthreshold potentials. Calcium indicators also have poor temporal resolution because calcium influx is generally slower than the other ionic currents during an action potential and indicators tend to report a filtered version of the true membrane voltage [57, 22]. Combining VSDs and calcium indicators result in an effective complementary signal that can acquire both subthreshold and action potentials but still has limited temporal resolution and sensitivity [10]. Due to the low temporal resolution of imaging systems and the indicators themselves, scientists must also go to great lengths to accurately reconstruct the spike timing profile and it remains a significant challenge where highly accurate timing is critical such as in network mapping applications [46, 113]. Special care must be taken with calcium indicators to control for differential expression between cells and can report different the proportions of active

cells depending on the specific type of indicator used [22, 64].

1.3 Conclusion

Patch clamp recordings fill a unique role among the many single cell recording techniques and remains the gold standard technique for high-resolution recordings *in vivo*. The aim of this work is to address the challenges that limit its ability to contribute to the brain activity map seeking to simultaneously record from all neurons in the living brain. Towards this goal, we will investigate automation strategies to increase the speed, efficiency, and reliability of the recordings by combining engineering precision with decades of manual experimental technique to transform what is considered an art form, into a high-throughput, deterministic, robotic system. Ideally it would operate with the precision and intelligence of the world's best technicians combined with the relentless pace and exacting repeatability of a machine. Here we show the development and successful operation of such a system and demonstrate its utility by, for the first time, performing multiple serial intracellular patch clamp recordings *in vivo* without requiring any human interaction. This is a significant step in the transformation of a highly manual and labor intensive technique into a set of robust automated tools.

CHAPTER 2

FUNCTIONAL REQUIREMENTS

This chapter will discuss the main functional requirements that must be considered to address the challenges in the patch clamp method using an automated approach. First, the scope of the automation will be motivated and defined, followed by a discussion of the importance of reliability, yield, and recording quality. Each will include brief descriptions of the final performance of the robot that will be discussed in detail in later chapters. One of the key aspect of developing an automated patch clamp system is translating the performance criteria defined by electrophysiologists into design metrics and constraints. The yield, throughput, and quality of *in vivo* patch clamp experiments are rarely discussed in literature and many labs have slightly different standards of performance and quality, both of which lead to some ambiguity about the criteria which must be clarified.

Another goal of this work is to quantify the methods used in manual experiments to control the pressure on the pipette, position it in the brain, and make all the logical decisions made by the experimenter at different stages in the experiment. This not only enables the deterministic design of the automation hardware and algorithms, but also enables the discovery of the correlations between hardware performance criteria (e.g., pressure, precision) and *in vivo* performance (recording duration, access resistance).

2.1 Automation

One of the main limitations of *in vivo* patch clamp recordings is the time and effort required to obtain them. The three largest contributors are 1) training time, 2) low yield, 3) and the required continuous physical presence of the experimenter for the 4

- 6 hour experiments. All three of these limitations can be overcome by increasing the level of automation in the experiment. By training the robot to perform the experiment instead of a person, we can disseminate its intelligence digitally, instead of personally and eliminate training time. Typically, 6-12 months of training are required to learn to reliably perform *in vivo* patch clamp recordings. This limits adoption and creates additional overhead when personnel changes occur. The original autopatcher has already reduced the required training time to as little as 3 - 6 months and, more importantly, has transformed what was normally a highly skilled manual technique into a *transferable* software algorithm, permanently eliminating a portion of the required training time for new experimenters. A fully-automated system could furthe reduce the training requirements and we estimate that with the system presented here, that less than one month of training would be necessary to operate the robot. This does not include training for customizing the robot for different experimental protocols, but simply to learn to operate the robot in its current state.

This concept of automation was first developed by Kodandaramaiah et. al [69] who were the first to translate the manual procedures for *in vivo* patch clamp recordings into a set of robust algorithms and automated pressure and motor control. It automated the following steps in the experiment: pipette resistance check, regional pipette localization, neuron hunting, and gigasealing with a partial development of the break in step. The work presented here developing a fully-automated system is a direct extension of the original autopatcher and assumes the reader is familiar with those innovations [69]. In brief, the autopatcher is able to measure the resistance of the pipette as it is inserted into the brain and detect the resistance increase from making contact with the neuron and form the seal with the cell. The steps performed by the original autopatcher, and the remaining seven steps in a complete patch clamp trial, are shown in Figure 2. The fully-automated system presented here implements the same algorithms as the original, in addition to several new algorithms, and the

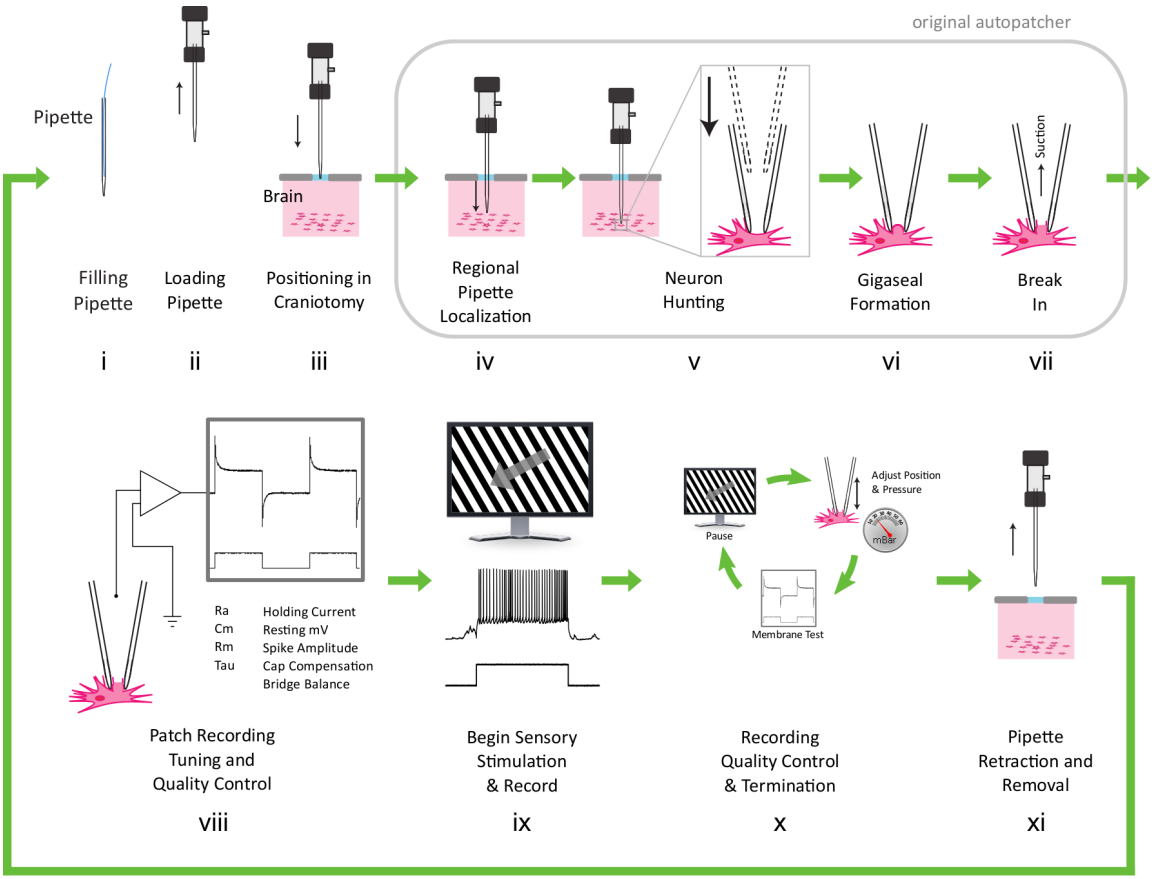

Step of Experiment	i	ii	iii	iv	v	vi	vii	viii	ix	x	xi	**Total**
Training Time (months)	0	0	0.5	0.5	2	1	1	0.5	0.5	0.5	0	**6.5**
Timing During a Manual Experiment (minutes)	0.5	0.2	2	1	3	2	1	5	0.5	5	0.5	**20.7**
Timing During a Fully Automated Experiment (minutes)	0.1	0.7	0	0	3	2	1	0.2	0	0.5	0.7	**8.2**

Figure 2: All the steps of a typical patch clamp experiment (i - xi). The grey box delineates the steps automated by the original autopatcher (iv - vii). The fully-automated system executes all of these steps (i - xi) and closes the loop (long green arrow) to achieve autonomous serial recordings.

reader is referred to that work for a full description. This thesis will focus on the innovations beyond those in the original autopatcher that are required to complete the loop (Figure 2 green arrow) and fully automate the experiment. This required developing seven completely new hardware subsystems (pressure control, automation control, pipette handling, pipette storage, length measurement, pipette filling, pipette holding) and includes software to automate the electrophysiological recording by imbuing the robot with sufficient intelligence to make the logical decisions and adjustments that normally require the training and experience of expert manual experimenters.

One of the goals of automating the experiment is to increase throughput. One metric to examine the efficiency of the process is by calculating the proportion of time spent during an experiment spent recording from neurons versus the time required to establish the recording. It requires approximately eight minutes to manually acquire a whole-cell recording, including changing the pipette and performing neuron hunting. It is slightly less for the fully-automated robot (five minutes) but because typical recordings are generally 15 - 60 minutes, additional speed improvements in the preparatory steps would seem not to have a large impact. However, when the yield is low (20%), the time required to prepare each trial becomes a significant portion of the experiment. Table 1 shows the proportion of time spent establishing the recording versus recording given different recording lengths, yield, and trial timing. The effect is especially noticeable when short recordings are performed.

Clearly, increasing yield and reducing the trial time would reduce the manual effort required and increase the efficiency, but controlling tissue pulsation, for example, to improve yield is a very difficult problem and has eluded experimenters for many years. We therefore pursued the possibility of completely eliminating the effort required of the experimenter by using a fully autonomous system. This would enable

Table 1: Table showing the amount of time spent recording versus the trial time to establish the whole-cell recording for various desired recording times, yield, and trial times. Every minute saved during a trial leads to approximately a 5% increase in recording time, assuming a 20% yield.

	Manual		Robot		
Trial Time (min)	8	8	5.5	5.5	5.5
Yield	20%	20%	20%	20%	10%
Recording Time (min)	15	60	15	60	15
Proportion of time spent recording	27%	60%	35%	69%	21%

operating several robots in parallel, amplifying throughput and alleviating the burden of managing a 4 - 6 hour experiment. This would completely offset the effects of low yield on the time of the experimenter. One could envision an array of robots, supplied with animals by a team of surgeons, gathering data autonomously without requiring an expert physiologist to be present. This would represent a major shift in the current paradigm for how patch clamp recordings are obtained. It would complement the current strategy of using manual experimentation to collect small data sets in a flexible manner, with the ability to collect large standardized data sets obtained by precise repeatable robots. This "big science" philosophy has been pioneered in neuroscience by the Allen Institute for Brain Science, and is proving to be essential in deciphering the immense complexity of the brain [81, 110, 1]. A fully-automated system will also enable single-cell *in vivo* pharmacology and high-throughput recordings from precious samples that are currently limited by staffing limitations. Increasing automation will also have a profound effect on increasing repeatability and reducing biases.

Because there are many different types of patch clamp experiments (cell attached,

inside-out, whole-cell, two photon guided, in vivo, in vitro), and many diverse experimental goals (sensory response characterization, morphological profiling, behavioral response) it would be very difficult to build a robot that incorporates every possible protocol. To limit the scope, we focused our efforts on developing a fully automating the blind *in vivo* patch clamp robot and demonstrating the feasibility of a fully-automated approach while characterizing the response of neurons in layer 5 of the mouse visual cortex in response to visual stimuli. This will provide the structural foundation that can be extended and adapted to other techniques.

The remaining tasks the robot must perform to completely remove the human from the loop in a patch clamp experiment are:

- Pipette storage
- Pipette handling
- Pipette filling
- Pipette holding
- Wire threading
- Accurate pipette tip positioning
- Determine the moment of break-in
- Break-in
- Initial recording quality control
- Amplifier tuning
- Current injections
- Begin & terminate sensory stimulus
- On-line quality control
- Error handling
- Pipette removal

These are in addition to those already implemented in the original autopatcher. The robot in this work successfully performs all these tasks, hands free, and is capable of performing 40 patch clamp attempts in 3.5 hours (5.3 min/trial), not including time spent recording. It has performed the first *in vivo* serial patch clamp recordings completely without human interaction with adequate yield and high recording quality.

2.2 Reliability

Patch clamp recordings are fraught with pitfalls in every step of the experimental protocol. As a consequence, technicians are continuously troubleshooting surgical

protocols, equipment malfunctions, pipette geometry, and optimizing their technique. They must quickly identify problems through testing, experimentation, intuition and experience. Many of the problems are also invisible or very difficult to measure and can exhibit non-specific symptoms. In order to be willing to incorporate new hardware into their methods, especially a complex automation system, users would have to have near perfect confidence in its reliability, proven over many experiments to be sure that it would not require additional troubleshooting and operational effort to use. To garner that confidence, the robot must have a similar or lower error rate than a human operator, particularly if the robot is to operate unattended. This requirement has a dramatic effect on the design decisions and development of the robot. Because all the tasks performed by the robot are sequential, the overall success rate is the product of the success rates of each individual task. Consequently, to reach even an *acceptable* overall success rate, each task must be executed flawlessly. This high level of polish is somewhat unique in a research prototype, but is one of the main design principles that is critical for a successful patch clamp robot. Early in the development process we discovered that subsystems that functioned with <90% success rates were inadequate once multiple systems were integrated in series. Subsystem success rates >90% later proved sufficient for the purposes of this study.

Table 2 shows the reliability of the of two versions of the robot that successfully obtained recordings and the result of the combinatorial probabilities. A skilled experimenter can manually perform these tasks very reliability after sufficient training (estimate >95%). For experiments using the robot where 30 pipette insertions are made and a success probability of 83.9% in these preparatory steps, there is a 99.4 % chance that at least one pipette will have an error according to the cumulative binomial probability. Even if the success probability was increased to 99.6%, then the probability that at least one pipette will have an error is only reduced to 10%. Given the variability in *in vivo* experimentation, we decided that the ability to recover from

a failure would be more effective at improving reliability than trying to identify and control the source of all possible errors. Most of the errors in these preparatory steps can be identified during the pipette resistance check stage where a wire threading failure and a pipette filling failure will give an infinite resistance, and a pipette tip positioning error can be identified by a drop in resistance upon insertion if the tip is broken by contact with bone or if the resistance increases when the pipette is clogged by the dura or a blood vessel. The recovery process simply involves replacing the pipette, which is one of the functional requirements discussed in Section 2.1. Using this strategy, the system can recover from all but the pipette handling errors, which can be reduced through proper robot calibration. The robot operation closely resembles the error handling processes used when failures occur during manual experiments but with higher throughput and repeatability. The robot on average has an error and recovers for 29.2% of pipettes, including pipettes that are rejected because their resistance is outside the usable resistance range (18%). The errors from filling, wire threading, and bad pipette resistances are not included in the yield calculations in Section 2.3.

The error rate from positioning the pipette tip in the craniotomy is one of the more critical aspects of the fully-automated system. The craniotomies prepared for version one of the robot were approximately 500 µm in diameter as compared to 250 µm for version two. This larger size reduced the probability that the pipette tip would come in contact with bone and break, leading to a higher positioning success rate, but when version one is used with 250 µm diameter craniotomies, the success rate is significantly lower ($\sim$ 50%). The measured success rate for version two (92.9%) requires much higher positioning precision and will be an essential requirement for any automated *in vivo* patch clamp system. This precision significantly reduces pipette breakage, clogging, and bleeding. Also, a smaller craniotomy size increases the stability of the recording as observed by expert experimenters and by those incorporating additional

Table 2: Reliability measurements of the two versions of the fully-automated robot shown in Figures 5 and 7. A skilled experimenter can manually perform these tasks with >99% reliability after sufficient training. *estimate. **craniotomies were approximately 500 µm in diameter so the positioning error would rarely cause the pipette to break. The craniotomies for V2 were approximately 250 µm in diameter to increase the recording stability which resulted in higher breakage rate despite the increase in positioning precision.

	Robot Ver1 (Figure 5)	**Robot Ver2 (Figure 7)**
Pipette Handling	99%*	98.8%
Wire Threading	96.3%	99.5%
Pipette Filling	manual	94.4%
Positioning Pipette Tip	98.8%**	90.4%
Total	**94.2%**	**83.9%**

automation [30, 28]. The quantification and successful implementation of a design that meets this functional requirement is one of the major contributions of this work. It is discussed in detail in Section 3.5.

Occasionally, other errors occur that require human intervention such as bleeding in the craniotomy or the need to refresh the ACSF on the surface of the brain. These and other exceptional events could be handled automatically, but the cost and complexity should be carefully considered in each case before attempting automation especially if the error only requires momentary attention or when the automation task would be prohibitively challenging.

2.3 Yield

The yield of the robot is crucial for efficiency reasons (less time spent changing pipettes from failed attempts) and for achieving quality recordings. For every pipette that is inserted into the brain, there is a probability that it will find and record from a neuron. If this probability, or yield, is low, then more penetrations will be made into

Table 3: Comparison of yield percentages at each stage of autopatching. The overall yield of manual patch clamp recordings averages around 20%. (* unknown data, tip positioning performed manually)

	Unbroken Pipettes	**Not Clogged**	**Detected Cell**	**Gigaseal**	**Whole-Cell**	**Total**
Original Autopatcher [69]	*	81%	93%	51%	82%	32.9% (24/73)
Fully-Automated Robot	90.4%	66%	95%	26%	68%	9.9% (30/303)

the brain, causing tissue damage, bleeding, and swelling which can affect recording quality. In some cases, such as for biocytin staining or GFP plasmid transfection for morphological reconstruction, only a single penetration is attempted so that the tissue is pristine for high-quality reconstructions.

The fully-automated robot has an average probability of obtaining a whole-cell recording in 9.9% (30/303) of trials compared to 20% [100] and 28.8% (17/59) from previous reports of manual experiments, and 32.9% (24/73) from the original autopatcher robot [69]. The yield was calculated from experiments where at least one whole-cell recordings was obtained, eliminating experiments that failed due to poor surgical preparation or non-optimal pipette geometry [100, 30]. This yield does include, however, all of the user and hardware errors that occur during a typical experiment using the fully-automated system and is therefore a realistic measure of the actual practical yield.

The yield in manual experiments often varies within one laboratory and between different laboratories (10 - 50%) [100, 69, 71] and is very operator dependent. For comparison, the average yield of the original autopatcher in our hands is between 15 - 20% versus the original 32.9%. These overall yields can be broken down into multiple individual failure rates measured at each step of the experiment (shown in

Table 3). In the fully-automated robot we see higher rates of broken pipettes and clogging, and a lower rate of successful gigasealing resulting an overall lower yield (Fisher's Exact test $p<0.05$). The increased pipette breakage and clogging is likely due to the variability in the placement of the pipette tip within a very small 200-300 µm craniotomy (see Section 3.3). A larger craniotomy would reduce the number of broken and clogged pipettes. It can also be a function of surgical quality. Damaged tissue, blood clots, and bleeding increase the incidence of clogged pipettes.

The low gigaseal rate is the most common failure mode for any patch clamp experiment and is typically attributed to problems with pipette geometry or surgical quality which could easily explain the difference observed here. Other possible causes include mechanical vibration, drift, or tissue motion. During a series of experiments using only the automated pipette holder where pipettes were filled and inserted manually, we observed at 29% whole-cell yield, comparable to the original autopatcher, indicating that the addition of the robot arm, pipette filler, and storage carousel may be the source of the reduced gigaseal rate. In future work, it would be important to test whether the pipette filler introduces contamination or whether storing the pipettes in open air contributes to this lower yield. This could be tested by inserting freshly pulled pipettes into the storage carousel just before use and compare that yield with pipettes that have been stored over several hours. Overall we see that the robot is approaching the yield of manual experimentation and note that because the system is fully automated, the per pipette yield becomes less of a priority due to the significant reduction in effort required to obtain the recordings.

Additional improvements to the hardware and algorithms, as well as improvements in pipette geometry and surgical technique [70] will likely continue to increase this yield. For example, if the design of pipette positioning system was improved to be more accurate it would reduce the number of clogged and broken pipettes would increase the yield to approximately 13%. It is also likely that pipettes that are clogged

during descent can go undetected and lead to gigaseal failures.

Despite the overall lower yield per pipette, the fully-automated robot was still able to record, on average, from 2.5 cells per experiment (30 cells in 12 experiments) which is similar to the throughput of manual patch clamp experiments and the original autopatcher (2.9 cells per experiment, 47/16). Throughput is a challenge even in manual experimentation and is one of the main reasons that *in vivo* patch clamp recordings are not more widely used. *In vivo* experiments also require larger data sets to find significance due to spontaneous noise and variation, requiring additional experimental effort. This is where automation is likely to have the largest impact through parallelization.

Some scientists claim a 70% yield in vivo when performing manual experiments, although these are the minority. This indicates that there are possibly additional algorithms and hardware that could further enhance the performance of patch-clamp robots. Although the autopatcher algorithm elegantly and simply captures a significant portion of the situations encountered by the robot *in vivo*, we may be able to add additional tests (e.g., pipette checks) and algorithms that incorporate the expertise employed in these high yield experiments and account for every eventuality during experimentation. Although this may increase the complexity of the robot, these improvements over time can be refined quantitatively using a repeatable robot. By incorporating the high yield techniques in software, they would also be easily transferable in the community.

2.4 Recording Quality

Recording quality is perhaps an even more important performance metric than yield, especially for a high-throughput robot where low yield can be overcome by speed. Access resistance, pipette resistance, and seal resistance are all very important metrics for obtaining high signal-to-noise ratio recordings and the resting membrane potential,

membrane resistance, and action potential amplitude are all indications of the health of the cell. Both of these factors must be of a certain quality for the recorded voltages to be considered physiological and publishable. These thresholds are: 1) a resting membrane voltage of the below -55 mV for most pyramidal neurons, 2) the peak of the action potentials should overshoot 0 mV, 3) a holding current less than $\pm$200 pA, and 4) an access resistance below 50 MΩ [100, 30, 71]. Any significant drifts or irreversible change in these metrics indicates an unstable recording. For experiments investigating a behavior or sensory stimulus, stable recordings longer than 15 minutes are generally necessary.

In vivo recordings are more difficult to establish and maintain because of tissue motion caused by heartbeat and breathing which can disrupt the seal between the membrane and the pipette. This often degrades the health of the cell and reduces the resolution of the recording. The access resistance between the amplifier and the cell may also increase over time if organelles or remnants of the ruptured membrane block the tip of the pipette. This also reduces the resolution of the recording and occurs much more often *in vivo* than *in vitro*. Acceptable access resistances *in vivo* are below <50 MΩ [71, 100, 30, 24, 29] and <15 MΩ for *in vitro* [135]. Others have employed rapid position feedback control to follow the movement of the tissue with the pipette actuator to increase the stability of the recordings [34].

The health of the cell and the access resistance can also be affected by the physical stability of the pipette. In most electrophysiological systems, the actuators can position the pipette with sub-micrometer resolution and are specifically designed to have low drift (<1 µm/hr). This is essential to prevent the pipette from drifting into or away from the cell causing stress in the membrane and on the seal with the pipette. This stress can lead to blockages in the tip of the pipette and increase the access resistance. The degree of physical stability in the system is also visible in the average length of the recordings. We found that for the robot to acquire high-quality, stable,

long duration recordings required less than 1 µm of drift. Section 5.4.1 discusses the stability and quality of the recordings produced by the robot in more detail. To summarize, the robot had an average recording duration of 19.8 minutes with recordings up to 110 minutes, similar to other reports, as well as similar resting membrane voltages, holding currents, and significantly improved access resistance as compared to the original autopatcher. These recordings were of sufficient duration and quality to conduct experiments in layer 5 of the visual cortex in mice and characterize their visual response.

CHAPTER 3

FULLY-AUTOMATED PATCH-CLAMP ROBOT

3.1 Introduction

Here we describe the design and development of the fully-automated patch clamp recording robot that is capable of performing 40 serial recording attempts *in vivo* without any human interaction. It represents a major step in the transformation of the manual "art" of patch clamping into a fully-automated informatic science by removing the human from the loop and overcoming many of the critical design challenges that have limited the adoption and impact of the patch clamp method over the last 30 years. In this chapter, a short overview of the final design of the robot will be followed by a discussion of the overall hardware architecture and the detailed development of each subsystem will be shown.

Figure 3 shows a schematic view of the entire experimental setup including the traditional electrophysiology equipment, mouse, and the new automation systems.

The pressure control system developed in this work is responsible for supplying and controlling the four pressure states used in the original autopatcher algorithm, replacing the syringes in the original system and enabling analog computer control of each pressure. The automation controller was developed to control eight of the nine motors in the system that allow pipette holding, wire threading, pipette filling, pipette storage, and pipette manipulation. It also controls the Peltier cooling system on the filling station that chills the fluid to be dispensed into the pipette. It also controls the pneumatics and a custom syringe pump required to dispense the fluid. It distributes the motor control and pneumatic control requirements across three embedded microcontrollers that communicate with the master computer over a standard

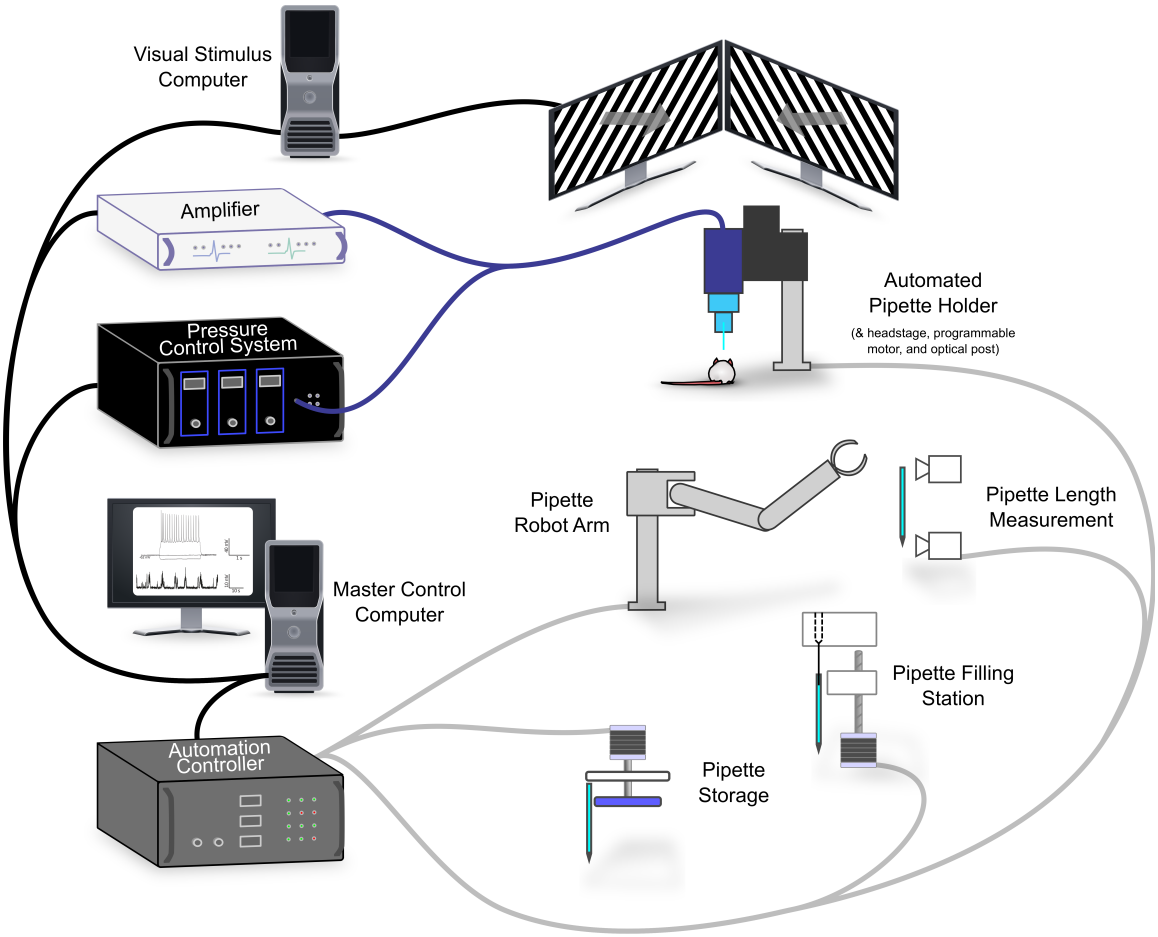

Figure 3: Overview of the patch clamp robotic hardware that performs fully-automated *in vivo* serial patch clamp recordings. The pressure control system, automation controller, pipette robot arm, pipette storage system, pipette filling station, pipette length measurement system, and automated pipette holder (light blue) were developed in this work to enable full automation.

serial communication protocol.

The master computer coordinates all of the various subsystems using a hybrid event-driven state-machine software architecture to control the visual stimulation during the recording, perform amplifier compensation, inject current into cells, retrieve pipettes from storage, fill pipettes, measure the length of the pipette, position pipettes in the craniotomy, thread the silver wire, and perform all the steps of the patch clamp experiment (e.g., neuron hunting, gigasealing) by controlling the pressure control system, performing data acquisition, and moving the pipette programmatically.

We developed several early prototypes to help identify the most significant challenges in the design. The patch pipette is highly sensitive to vibration, temperature changes, electrical noise, and mechanical drift and these initial prototypes helped elucidate the subtle interactions between the traditional patch clamp hardware and the new robotic hardware and their relative impact on the performance.

3.2 Hardware Architecture

One of the first design decisions was to determine the correct arrangement of the motors and subsystems to automate the remaining tasks in the experiment. The tasks consist of several pick-and-place and threading operations, some requiring high mechanical and pneumatic precision. Originally we pursued an integrated design approach where all the functions would be tightly integrated to reduce the number of degrees of freedom and make the system more compact. Figure 4 shows the cluttered space immediately surrounding the mouse. After discovering several challenges in the integrated design, we pursued a segregated approach allowing individual optimization of each subsystem and reduced negative interactions. The overall architecture plays a critical role in the success of the robot by dramatically affecting the performance, flexibility, modularity, robustness, and development time. It also has a large impact on

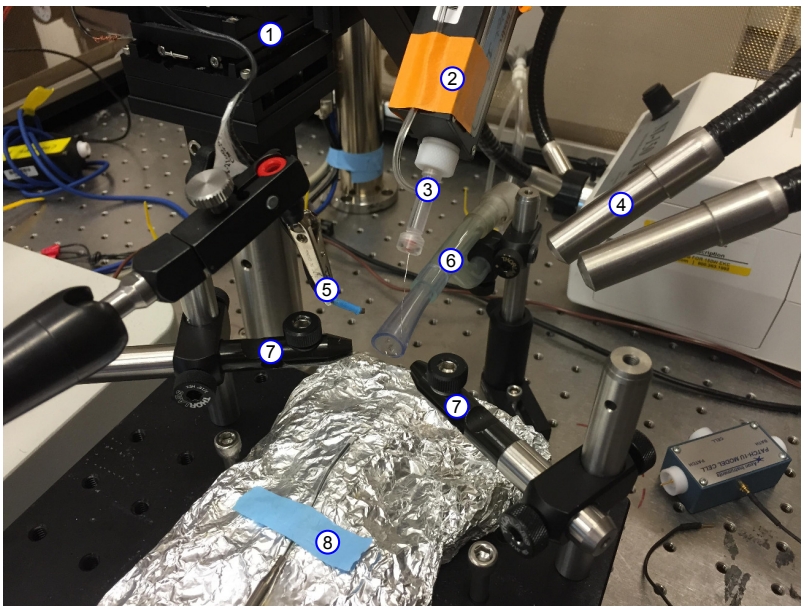

Figure 4: Photograph of a typical patch clamp recording station showing the tight spacial constraints. Many experiments typically include additional equipment such as a two-photon microscope, whisker stimulation hardware, or computer monitors to deliver visual stimulation which requires that any additional automation hardware must have a minimal footprint. A thin metal headplate, is surgically implanted and cemented to the skull of the mouse and secured between the headplate clamps to stabilize the skull during recordings.

the subsystems discussed in later sections which are heavily dependent on the pipette handling strategy and require significant redesign when the architecture changes.

3.2.0.1 Integrated Approach

The first prototype of the robot was a fully-integrated system that could perform fully-automated recordings combined all the necessary hardware onto the same optical post as the patch clamp amplifier headstage and pipette (Figure 5). We hypothesized that this integrated and compact design would be the simplest solution, requiring the fewest number of motorized axis and meet the tight space constraints surrounding the mouse. Figure 4 shows the density of the recording accessories that are typically present in the 100 mm space surrounding the head of the mouse. While this architecture was able to record from many neurons, it lacked the positional precision (see Section 3.3), mechanical stability necessary (see Section 5.4.1), and operational

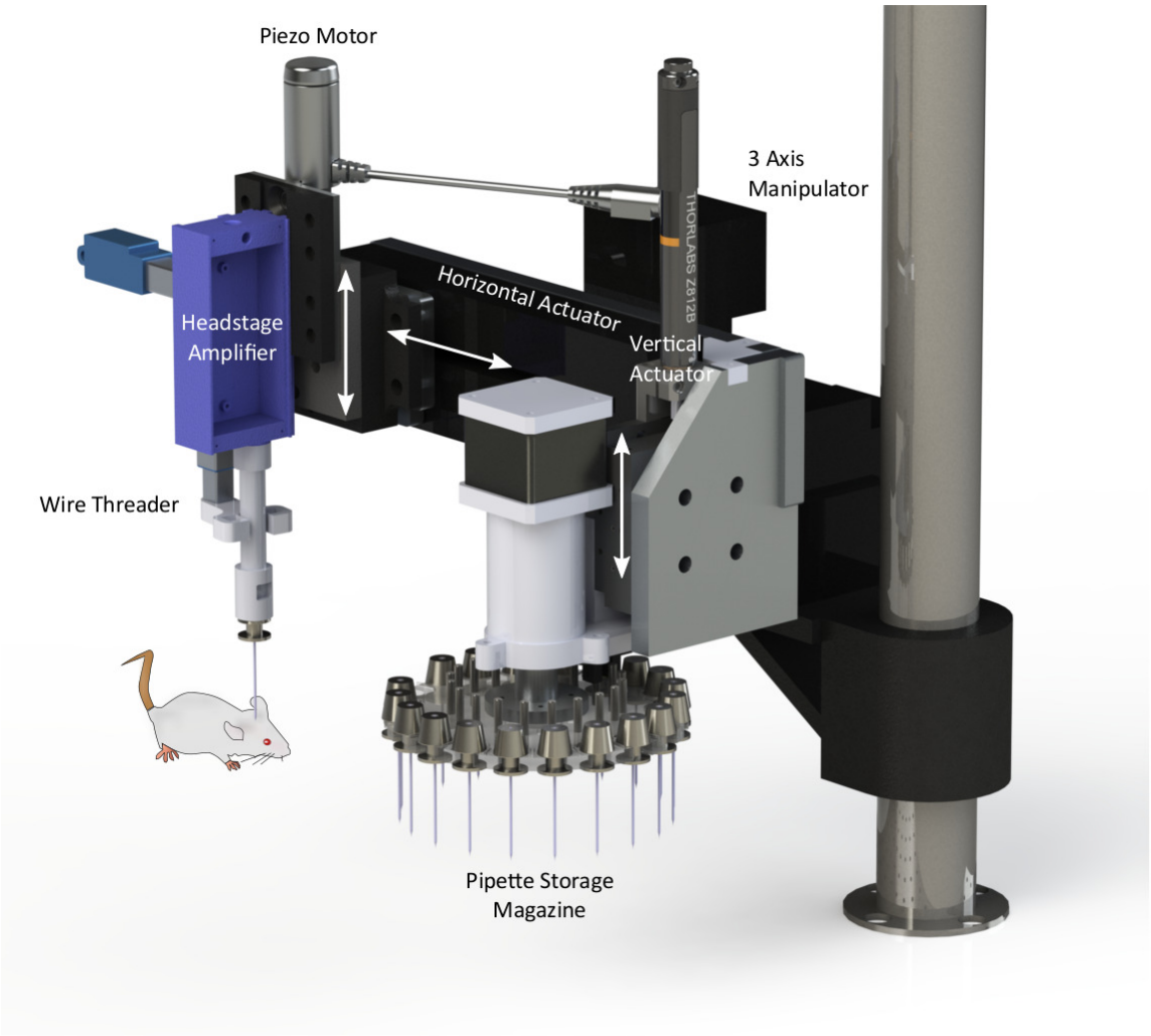

Figure 5: Rendering of the hardware architecture of the first version of the fully-automated patch clamp robot. It is roughly based on the design of a CNC tool changer using tapered collets to accurately position the pipette in the wire threader and for positioning in the craniotomy. First, the horizontal actuator moves the amplifier headstage and wire threader to the pipette storage magazine. Then, the vertical actuator raises the magazine up to insert a pipette into the threader and the horizontal motor returns to position the pipette above the mouse. The piezo motor lowers the pipette into the brain and after the recording is complete, the cycle repeats. The magazine rotates to the next pipette for the next trial. The 3 axis motor is used to manually align the tip of the first pipette with the craniotomy at the beginning of the experiment. The precision in the tapered steel collets ensure that the subsequent pipettes are also automatically aligned with the craniotomy.

robustness for high throughput, high yield, and long duration recordings.

With the pipette handling actuators, storage carousel, length measurement system, and other hardware integrated onto the same structural frame, we discovered that every one of those systems would have to meet the high stability requirements (<1 µm/hr drift) required for stable recordings. This significantly increases the costs of the components and this approach quickly becomes unwieldy as new systems are added to accommodate new features (e.g., pipette filling). The system eventually reached a point where any additional heat, vibration, cable strain, or electrical noise would prevent it from obtaining and sustaining long duration recordings. This core design flaw of integrating all the hardware was reflected in the performance of this prototype. This system did obtain 33 *in vivo* whole-cell recordings but only averaged 4.1 minutes in length, insufficient for a typical *in vivo* study. In addition, troubleshooting was made significantly more difficult because as each new feature is added it exponentially increases the number of possible interactions between systems, requiring characterization and mitigation. This effort, added to the troubleshooting already inherent in patch clamp experiments, simply added to the burden and reduced the performance *in vivo*. An integrated approach could eventually be the most optimized system after sufficient development but should be pursued after the basic automation tasks are successfully implemented in an independent fashion to show feasibility and identify the most critical design parameters.

Upon deploying the integrated robot *in vivo*, we noticed several failure modes during the recordings that were possible indicators of the lack of mechanical stability. Figure 6a shows a recording where a discrete event, disrupted the quality of the recording (blue arrow). In 55% (n=6/11) of a subset whole-cells obtained using the robot, a similar discrete event caused a loss of the recording. This could be due to high access resistance caused by a bad break in or due to a mechanical disturbance. These events occurred on average 7.2 minutes into the recording (σ = 5.3 min) thus

preventing the robot from recording for the 20 minutes necessary to characterize the intrinsic and sensory evoked behavior. To determine whether the discrete disturbance was due to external mechanical sources, we measured the position of the pipette using an attached conductive target and a capacitive probe (Lion Precision CPL190, C1-A Probe, <30 nm resolution). We did not observe any discrete mechanical disturbances while the robot was powered down, indicating that external disturbances not likely a cause. This also confirmed that the vibration isolation table was sufficiently isolated from the building and, importantly, the heavy construction equipment operating across the street.

During dry runs of the robot in operation, we did not measure any discrete pipette displacements during the recording phase of operation. This does not, however, rule out the robotic hardware because it was not possible to instrument every component in the system or run through every operational state of the robot. Ideally, we would have measured the position of the pipette during an intracellular recording where a discrete disturbance might have been observed directly by both the capacitive probe and the patch amplifier to positively determine the cause. However, the capacitive probe introduces too much electrical noise into the recording for it to be used during an experiment. We concluded that rather than continue to search for the root cause in this complex, highly interacting design that was very resistant to the modifications needed for conclusive testing, we would separate and isolate each subsystem to better control and measure the individual effects on the performance *in vivo*.

We also measured the drift in the mechanical structure of about 3 µm/hr which is more than normally acceptable but probably not severe enough to shorten the recordings so dramatically. We determined that the drift was in part caused by relaxation in the manual dovetail manipulators used to position the entire structure. This relaxation occurred whenever the robot moved the headstage to the pipette storage carousel and the weight distribution changed. After replacing the dovetails

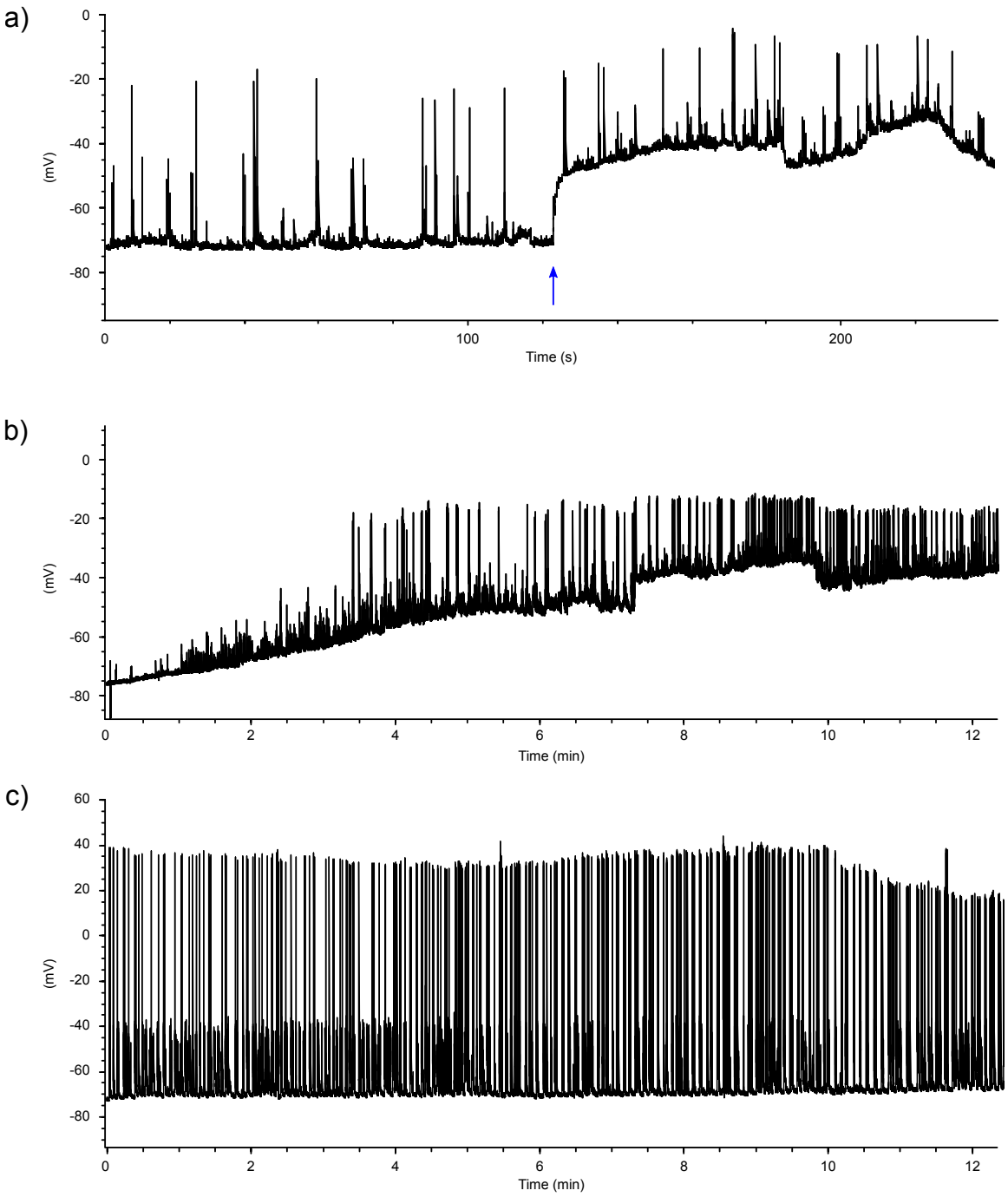

Figure 6: (a) Is a representative intracellular recording obtained using the integrated robot design (Figure 5). It suffers from high access resistance due to poor break-in and was disrupted by an unknown cause in a discrete manner (blue arrow). Similar discrete events were observed to disrupt 55% of the recordings made with this robot (6/11) preventing any recordings longer than 9 minutes. (b) Is an intracellular recording also obtained using the integrated robot that exhibited drift in the resting membrane potential and poor access resistance. (c) Is a recording obtained using the new robot design (Figure 7) exhibiting excellent stability and low access resistance. This improvement was a result of a number of changes in the overall architecture and subsystem designs.

with a rigid static structure and using the dovetails to position the mouse relative to pipette rather than the inverse, the stability improved to 2 µm/hr. The remaining drift in the system had dozens of other potential contributors (e.g., cable strain, motor thermal effects, air temperature and convection) from every component in the integrated design. This also contributed to the decision to pursue the segregated strategy where individual subsystems could be added and removed to conclusively identify sources of drift, vibration, and electrical noise.

3.2.0.2 Segregated Approach

Our next approach was to isolate as much of the automation hardware from the main optical post as possible to eliminate interactions between the hardware and the neural recordings and increase the stability of the pipette. It was also designed to be modular and flexible enough to accommodate new hardware as needed without forcing significant architectural changes. This quickly became important as we added the pipette filling and length measurement hardware and would be essential if the robot were to be combined with other techniques such as automated RNA extraction. Figure 7 shows an overview of the main components of the final design. The recording amplifier and pipette holder (Figure 7a) are isolated from the robot arm, filling station, and storage carousel (Figure 7b,c,d). The pipette length measurement system is not shown. This physical isolation dramatically reduced the complexity of the engineering analysis and experimental measurements required to design and troubleshoot the system.

Figure 6c shows the result of these improvements on the stability of the recordings. The average recording time at high-quality levels increased immediately from 4.1 minutes (n = 12, range 0 - 8.8 min) to 7.7 minutes (n = 27, range 0 - 30 min) during that set of experiments, and the discrete disturbances disappeared from the recordings. Later improvements in surgical technique, algorithm adjustments, and

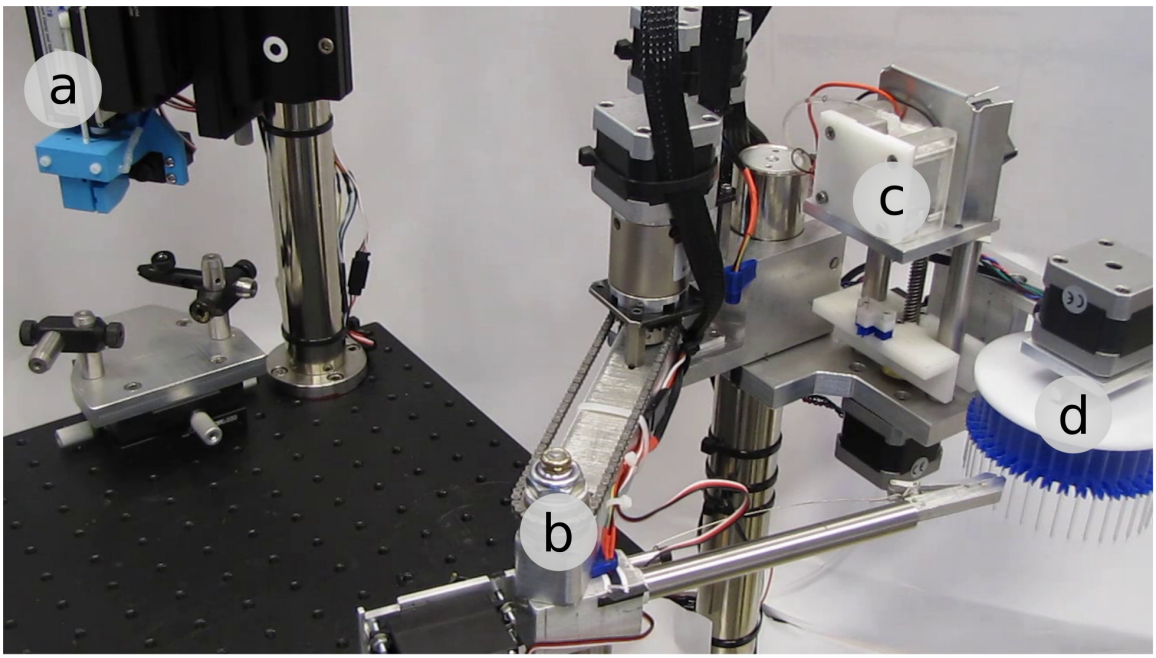

Figure 7: Photograph of the final version of the fully-automated patch clamp robot. (a) Includes the headstage, programmable linear motor (not visible), and the custom automated pipette holder (blue). (b) Is the two degree of freedom RR robot that moves the pipettes between the storage carousel (d), filling station (c), automated pipette holder (a), pipette length measurement module (not shown), and the sharps disposal container (not shown). The pipette filling station (c) consists of a stepper motor and lead screw that linearly actuates a shuttle that threads the pipette over a capillary filled with intracellular solution. A separate pressure control system pressurizes the capillary and dispenses 1.5-4 µL of intracellular solution into the pipette. The intracellular solution is cooled to 4 C by a Peltier cooling module, heatsink, and fan. (d) The pipette storage carousel can hold up to 40 pipettes and is rotated by a stepper motor.

pipette geometry increased the average recording time to more than 20 minutes (n = 40, range 0 - 110 min) indicating we had achieved a very stable system. These stability improvements were the result of a number of design changes required to implement the segregated approach so the ability to determine the relative contributions of each change was impossible. The segregated approach also reduced the complexity of each subsystem allowing standard components to be used and independently developed. This also resulted in an overall increase in the reliability of the robot, critical for a system of this complexity.

The value of the segregated approach can be illustrated by an example where the vibration from the brushless DC fan used as part of the cooling system that chills the intracellular solution in the filling station was transmitted through the optical post supporting the robot arm, through the vibration damping optical breadboard, and up through the optical post supporting the pipette. The vibration was clearly visible in the voltage fluctuations recorded by the headstage. The solution was to separate the fan from both optical posts and mount it on the Faraday cage with structural support to position it 3 - 5 mm away from its original location. This allowed it to perform its cooling function while isolating mechanical vibration. This type of mitigation is not possible with an integrated approach where relocating the fan might cause interactions with other systems.

We measured the drift of the segregated system to be 0.6 µm/hr, sufficient for stable recordings. Interestingly, we also measured the drift after turning on the two computer monitors inside the semi enclosed space of the Faraday cage and the black-out cloth and found that the drift was between 8.4 and 12 µm during the first hour indicating a significant thermal expansion effect and a long time constant to reach steady state. After this point, the animal heating pad, monitors, and motor controllers were all left running continuously to maintain steady state temperatures across the mechanical structure.

3.3 Pipette Holding

The traditional pipette holder shown in Figure 8 performs multiple critical functions during patch clamping. It acts as the electrical, pneumatic, and mechanical interface between the delicate glass pipettes and the macroscopic environment. It connects the fluid inside the pipette to the patch amplifier, provides mechanical stability, and also forms a pneumatic seal with the pipette to allow pressure control. These are expensive

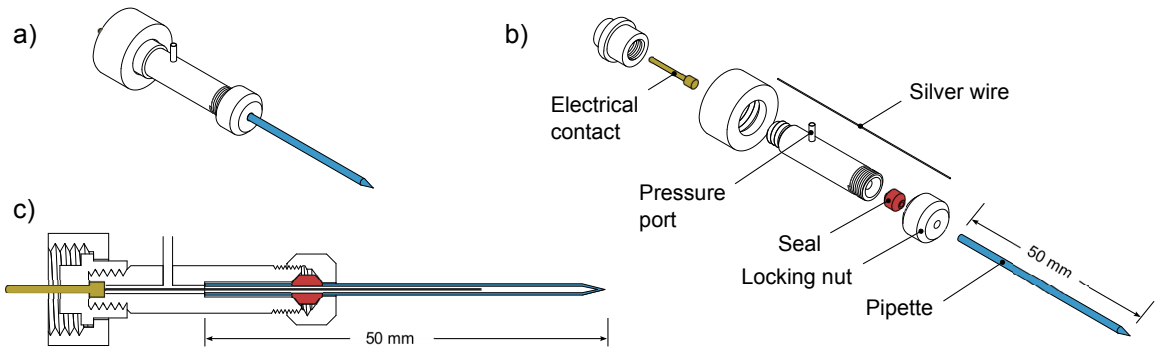

Figure 8: (a) A schematic of the pipette holder traditionally used in patch clamp experiments. (b) Exploded view. (c) Cross-sectional view. The glass pipette is colored blue, the silicone seal is red, and the gold electrical contact is yellow.

devices ($100 ea.) and the functions are very interdependent in the design. For example, the pneumatic seal also acts as the mechanical constraint to physically restrain the pipette which results in very imprecise position repeatability. The basic design of the holders has largely remained unchanged due to their high reliability and small physical footprint which allows multiple pipettes to be arranged in close proximity for multiple simultaneous recordings. They generally consists of a machined cylindrical polycarbonate body, a cylindrical silicone seal shaped like a revolved trapezoid, a gold connecting pin, 50 mm of silver wire, two threaded end caps, and one threaded nut to physically connect it to the amplifier. The holders are also have a port where tubing is connected to allow control of the pressure on the pipette (see Section 3.10). To insert the pipette into the holder, the user fills the pipette with intracellular solution using a microfil (Warner Instruments MF28G67-5, or Eppendorf Microloader), then carefully threads the back end of the capillary (ID 860 µm) over the silver wire (OD 200 µm), being careful not to bend the wire or scrape the sharp edges of the glass on the wire. The user typically has to navigate slight bends and imperfections in the wire to prevent bending the wire during threading. The pipette is then inserted through the silicone seal and fully seated into the holder. Then the locking nut is tightened which compresses the seal around the pipette which simultaneously

seals and mechanically restrains the pipette. The pipette filling, wire threading, and pipette insertion steps require several days of training, manual dexterity, and visual acuity to prevent damage to the pipettes and to become efficient.

In addition to its essential functions, the holder is also designed to be as narrow and short as possible so that the length of wire extending out of the recording headstage is minimized. This reduces noise in the recording by reducing the length of wire acting as an antenna. The polycarbonate body provides electrical isolation and separation to reduce capacitive coupling with nearby conductive materials, also reducing noise. The pipette holder can be completely disassembled for cleaning and to replace the silver wire and seals. Salts from the intracellular solution frequently collect inside the holder along with silver and silver-chloride particles dislodged from the surface of the wire by the sharp glass edges of the pipette. These contaminates often lead to clogged pipettes and prevent successful recording attempts so cleanliness is essential. This can be difficult to troubleshoot because the contaminates are often invisible without using a microscope.

3.4 Automated Pipette Holding

While the traditional holders are very effective, they require a delicate touch when changing pipettes, and don't lend themselves well to automation. Inserting a glass pipette (OD 1.5 mm) accurately into a small hole (1.75 mm), forming a pneumatic seal with the pipette, and threading a freely cantilevered silver wire into the pipette require a high degree of precision and control. In addition, because the seal provides the mechanical constraint, which is inherently imprecise, the experimenter must manually manipulate and visually align the tip of each pipette within the 100 µm diameter area of the craniotomy for each recording attempt. This pipette insertion process and visual alignment typically takes 3 - 7 minutes per pipette when performed manually.

One approach to automate the process would be to develop a computer vision

system and two 6 degree-of-freedom robotic manipulators to replicate the same motion and stereo vision feedback control that a human employs to insert the pipette. However, this would be prohibitively expensive and complex to implement and would unlikely reach the same level of robustness and flexibility required for the many different types electrophysiological experiments [31, 13]. The system would have to measure the position in space of both the craniotomy, silver wire, microfil, and pipette requiring both high optical power (200x) and a large working envelope (approximately 200 x 200 x 200 mm). In addition, because of the close proximity to the mouse, such a system would have to be designed to produce low electrical noise and not affect the mechanical stability of the pipette (drift <1 µm/hr, minimal vibration, minimal dynamic thermal gradients).

We decided to take a simpler approach to enable robust pipette positioning, pneumatic sealing, and wire threading using precision mechanisms that require fewer actuators and sensors. The biggest challenge in the design of such a system is identifying and isolating interactions between the hardware that performs each task. Several iterations of the design will be discussed in detail, illustrating the interactions between the hardware systems that affect the overall performance of the system.

Our initial design was based on the system used to align cylindrical machining tools to the axis of the spindle in milling machines and lathes. It uses a collet that is compressed around the cylindrical body of the tool by forcing it into a tapered feature on the spindle. They can repeatably align the tool to within 12 µm of the spindle axis over multiple removal and insertion cycles. Figure 9a-b shows our 3D printed collet, mating taper, linear actuator for driving the mating taper over the collet taper, the silicone seal, and a magnetic wire threading mechanism. As the linear actuator descends, a magnet applies a downward force on the ferromagnetic bead attached to the silver wire, pushing it through a wire guide hole and into the pipette. Simultaneously, the actuator forces the mating taper into contact with the

taper on the collet which compresses the collet radially around the pipette providing mechanical constraint. As the collet compresses around the pipette it simultaneously compresses the silicone seal (Figure 9c) around the pipette. The collet compression eliminates the need to tighten a locking nut to physically restrain the pipette and compress the seal. Overall, the design is compact, mostly non-conductive, and only requires one simple linear actuator.

However, the design suffers from several major flaws. The first, shown in Figure 9d, shows the silver wire buckling inside the body of the pipette holder as the ferromagnetic bead exerts a compressive force on the wire while attempting to push it through the guide hole. There was sufficient friction between the wire and the guide tube to exceed the buckling force of the thin silver wire. After the wire buckles, the holder must be completely disassembled, the wire straightened, and reassembled requiring up to 30 minutes per failure. This type of failure is unacceptable during an *in vivo* experiment where time is of the essence. If the wire is perfectly straight and the guide tube very smooth, the wire could thread reliably but the design was too sensitive to unpredictable friction effects and failed often. Another drawback to this design is that for every millimeter of wire that the wire is threaded into the pipette, there is a corresponding millimeter of additional length that must be allocated to maintain contact with the sliding connector. Therefore, for an equivalent length of wire inserted into the pipette, this design will have a wire twice the length of than a traditional pipette holder as well as additional length from the sliding contact for a total of three times the inserted length. This significantly increases the noise in the recordings.

Threading the pipette into the collet also presented additional challenges. As the pipette is inserted, the sharp edges of the glass catch on the plastic collet, the silicone seal, and the inside walls of the holder (Figure 9e,f). When these edges came in contact with the holder it could resist extremely high insertion forces causing pipette

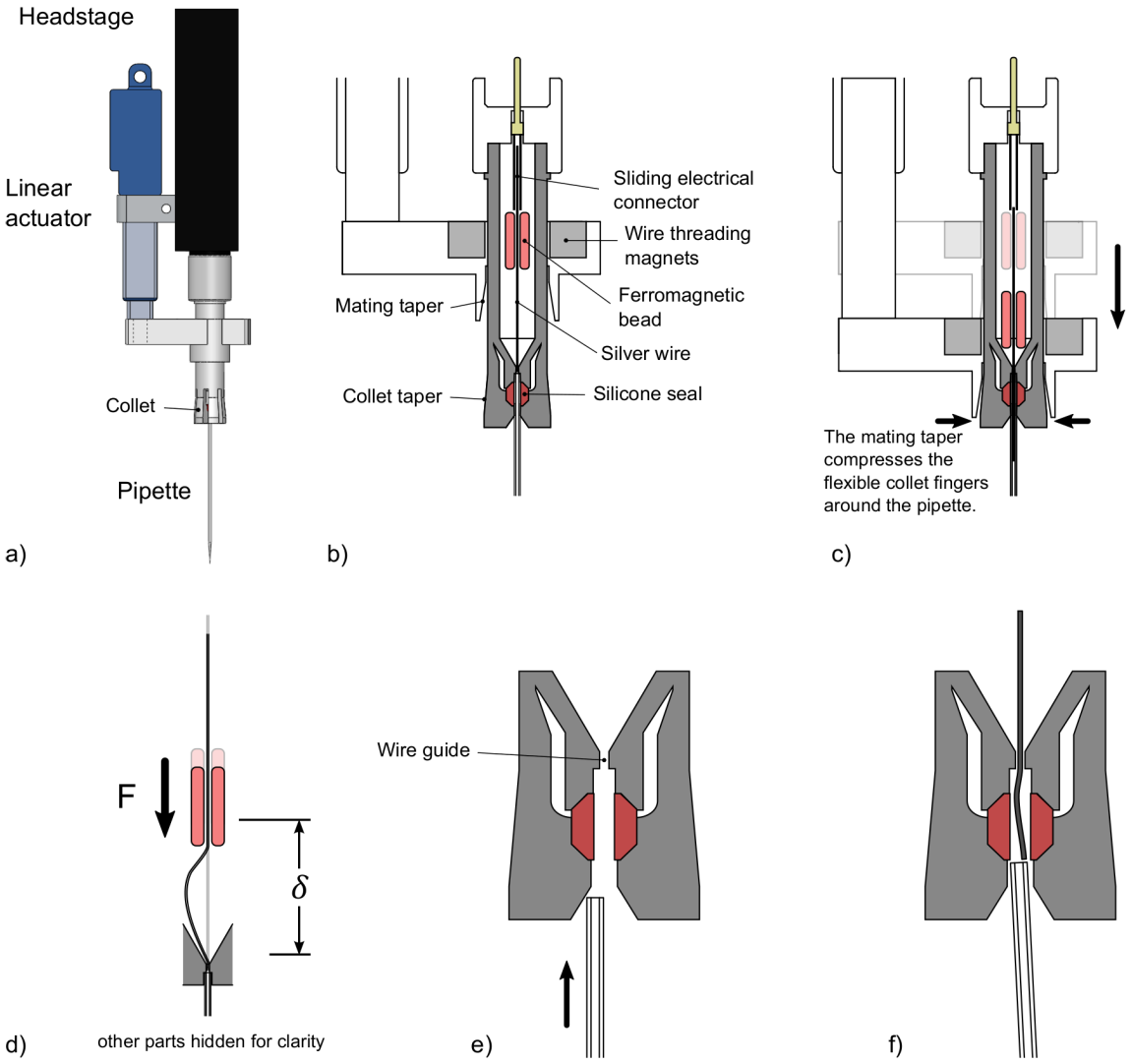

Figure 9: Schematic showing the function of the first pipette holder prototype. (a) The assembled design. (b) Labeled cross section of the holder. In (c) the linear actuator lowers the magnets and mating taper, inserting the silver wire and compressing the collet. The magnets exert a force on the ferromagnetic bead, pushing the wire into the pipette. The sliding electrical contact maintains an electrical connection with the amplifier as the wire is threaded. (d) Shows a common wire buckling failure. Because the total threaded length of the wire is under compression (δ), it buckles easily even with the minor friction forces at the wire guide. The holder must be completely disassembled to straighten the crushed wire. (e) Shows the sharp edges on the pipette getting caught on the wall of the collet and on the silicone seal (f) during insertion. These prevent the pipette from seating completely against the wire guide. (f) Shows also shows the silver wire buckling and failing to thread if the pipette is not inserted completely, another catastrophic failure.

breakage before insertion could occur. A human can feel an increase in insertion force and in response, change the insertion angle or realign the pipette to reduce friction. Because the robot did not sense these problems or have a way to adjust for them, the pipette was often not fully seated in the holder. This subsequently causes a catastrophic wire threading failure where the end of the wire would come in contact with the back of the pipette and buckle as it is extended out of the guide tube (see Figure 9f), again requiring complete disassembly. No amount of increased precision in the alignment during insertion or geometrical optimization was sufficient to prevent the sharp edges from catching on the seal or the collet itself. As a consequence, this design was discarded. We also discovered that despite the elegant nature of the design of only having one linear actuator perform the sealing, mechanical constraint, and the threading tasks, it restricted our efforts to optimize and troubleshoot the design because they couldn't be independently varied without affecting the performance of the other systems. This pipette holder design and the prototypes of the integrated approach were developed by Jamison Go, Aaron Fan, and Coby Lu as part of their senior capstone design project [40].

Our second design sought to address these issues by changing the arrangement of the collet (see Figure 5 for the complete system). This design was also the integrated design discussed previously. Each pipette is manually inserted into a machined collet in a fashion similar to those found on tool changers for CNC milling machines (Figure 10). O-rings built into the collets provide the axial alignment with the tapered feature on the collet. This tapered feature aligns with the taper in the pipette holder. The collets are retained in the holder using neodymium magnets to provide passive retention, removing the need for additional motors or mechanisms. The collet precisely positions tip of the pipette within the craniotomy using the mechanical precision of the collets rather manual visual alignment for each pipette in a manual experiment (see Section 3.5). It uses the same wire threading mechanism as before but the linear

actuator no longer performs multiple functions, it simply threads the silver wire. The pneumatic seal is provide by three o-ring seals; two are axial seals around the pipette and one is a face seal between the collet and the holder.

To load a pipette, the user first manually inserts the pipette through the collet where the two internal o-rings aligned it with the axis of the collet taper. The collet is then inserted into the tapered socket of the holder and retained by the magnets. The linear actuator in the figure then lowers the "wire threading magnets" which pushes the wire into the pipette as before. The robot was able to thread the wire with approximately a 90% success rate which was sufficient to obtain recordings, but it did reduce the overall throughput and performance.

The most challenging part of this design is in the fabrication of the pipette collets. Of the dozens that were manufactured in-house (using a Haas OM-1 vertical mill), only 10 were sufficiently precise to meet the required tolerances for accurate pipette tip positioning. All the machine shops we contacted to out-source the fabrication declined to offer quotes for the design due to the tight tolerances. They suggested contacting higher precision companies that use more expensive machining tools, such as twin spindle Swiss-type lathes, which would easily increase the cost of the collets to $250 - $500 each. For a robot with 40 pipettes it would cost a minimum of $10,000. This is clearly an unsustainable manufacturing bottleneck that would significantly reduce adoption and impact.

In addition to requiring multiples of high precision and expensive parts, this design also led to contamination issues stemming from the manual threading of the pipette through the collet. When passing through the center of the collet, the sharp edges of the glass scrape the inside of the collet introducing metallic particles and evaporated salts into the pipette solution. In the case of these carbon steel collet prototypes, the pipettes also collected rust. This contributed to a high number of clogged pipettes in the experiment.

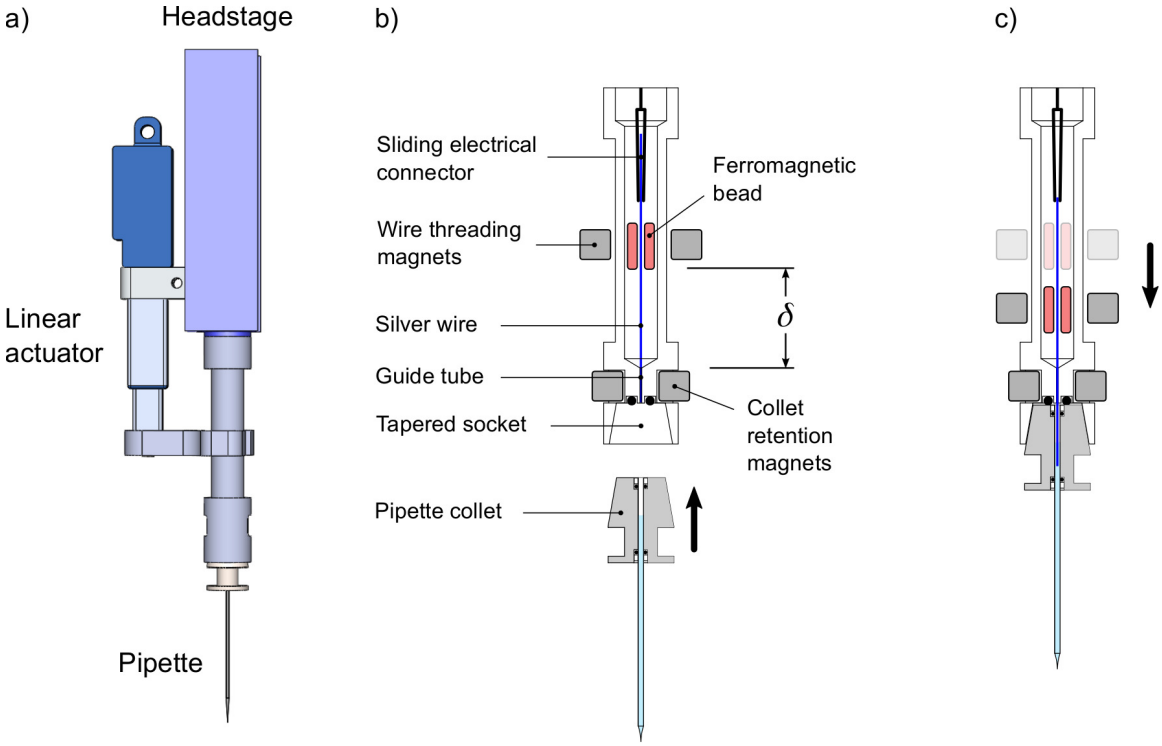

Figure 10: Schematic showing the operation of the steel collet based pipette holder. (a) Overview of the main components. (b) Detailed schematic showing the pipette collet, with a pipette already inserted, being inserted into the pipette holder and retained by the collet retention magnets. (c) After the collet is inserted, the wire threading magnets are lowered using the linear actuator to exert a force on the ferromagnetic bead, which pushes the wire into the pipette. This design solves the pipette insertion problems of the first prototype (Figure 9) and reliably aligns the pipettes with the wire guide tube. However it continues to suffer from a long wire compression distance (δ) that reduces reliability. The pipette collets, while functional, required extremely tight manufacturing tolerances ($\pm$6.5 µm) to achieve a pipette tip position repeatability of $\pm$100 µm which proved insufficient. This design did record from many neurons although the duration and quality were poor.

The use of neodymium magnets and steel collets, in addition to the ferromagnetic bead, also increased the electrical noise in the recordings from approximately 30 pA to 50 pA peak-to-peak through capacitive coupling and their close proximity to the silver wire. This is an even greater problem in cases where there are radiative sources of noise within the Faraday cage such as the monitors used to display the visual stimuli to the mouse. Normally radiative sources can be themselves shielded or relocated outside the Faraday cage, but for sources such as the monitors, shortening the length of the headstage wire or providing intermediate shielding are the only solutions.

We also discovered in our *in vivo* recording attempts that because the pressure control tubing was connected to the body of the pipette holder, the air was forced to pass through the wire guide tube to reach the pipette. With the silver wire threaded through the guide tube, it further restricted air flow and increased the time constant of the pressure dynamics, effectively reducing the quality of the break in attempts. This meant the robot could find and seal onto cells, but struggled to establish healthy whole-cell recordings. They often had high access resistances indicative of partially ruptured seals from too low of break in pressures (see Section 3.10). Unfortunately, due to the space occupied by the magnet retention system, o-ring, and guide tube, there was no additional physical material left in the body of the pipette holder to add an additional path for the pressure to reach the pipette.

For these reasons, this design was ultimately discarded although it did obtain 33 whole-cell recordings and helped us discover the critical design criteria for a successful automated pipette holder. We endeavored in the next design to 1) prevent contamination by eliminating all contact with the back of the pipette during insertion, 2) eliminate all conductive materials, 3) reduce the length of silver wire, 4) reduce the length of silver wire under compression during threading to prevent buckling (δ in Figures 9d,10b,11d), 5) improve the pipette tip positioning precision without increasing the cost of the system, 6) enlarging the pressure port to avoid restricting air flow, and

7) further isolate the different functions of the pipette holder to allow independent system optimization in the design.

The final, fully functional automated pipette holder design is detailed in the following sections and is the centerpiece of the design in Figure 7a. Figure 11 is a detailed view of the internal mechanisms. It performs the wire threading task with high reliability, provides a robust pneumatic seal, minimizes contamination, and provides even higher pipette tip position precision, and most importantly successfully acquired dozens of high-quality electrophysiological recordings.

Rather than using a collet system for precisely aligning the tips of the pipettes with the craniotomy, this design uses a vertically oriented v-groove kinematic constraint with a motorized clamp that opens and closes to allow the pipette to be inserted by the robot arm in Section 3.7. It also positions the tip of the pipette with higher precision than the collet design (see Section 3.5). Torsional springs provide the passive clamping force necessary to retain the pipette and allows the motors to be completely powered down during a recording, preventing the generation of electrical noise. The v-groove design also removes the need for multiple high-precision parts and was simple enough to be 3D printed. This significantly increases the scaling potential and reduces the cost of the system. It also uses a new wire threading mechanism (discussed in the next section) that significantly increases the reliability and maintainability.

This design also addresses the other previously identified issues. It reduces contamination by only requiring the pipette to be inserted 4 mm through an o-ring until it reaches a hard stop against the wire guide tube. The sharp edges of the glass only come in contact with the o-ring itself which is easily cleaned and doesn't catch on the sharp edges of the glass due to its flexibility and rounded geometry as opposed to the sharp geometry of the trapezoidal silicone seal used previously.

While the acrylonitrile butadiene styrene (ABS) 3D printed design was very effective, it is somewhat porous, has poor surface finish which introduces some variability

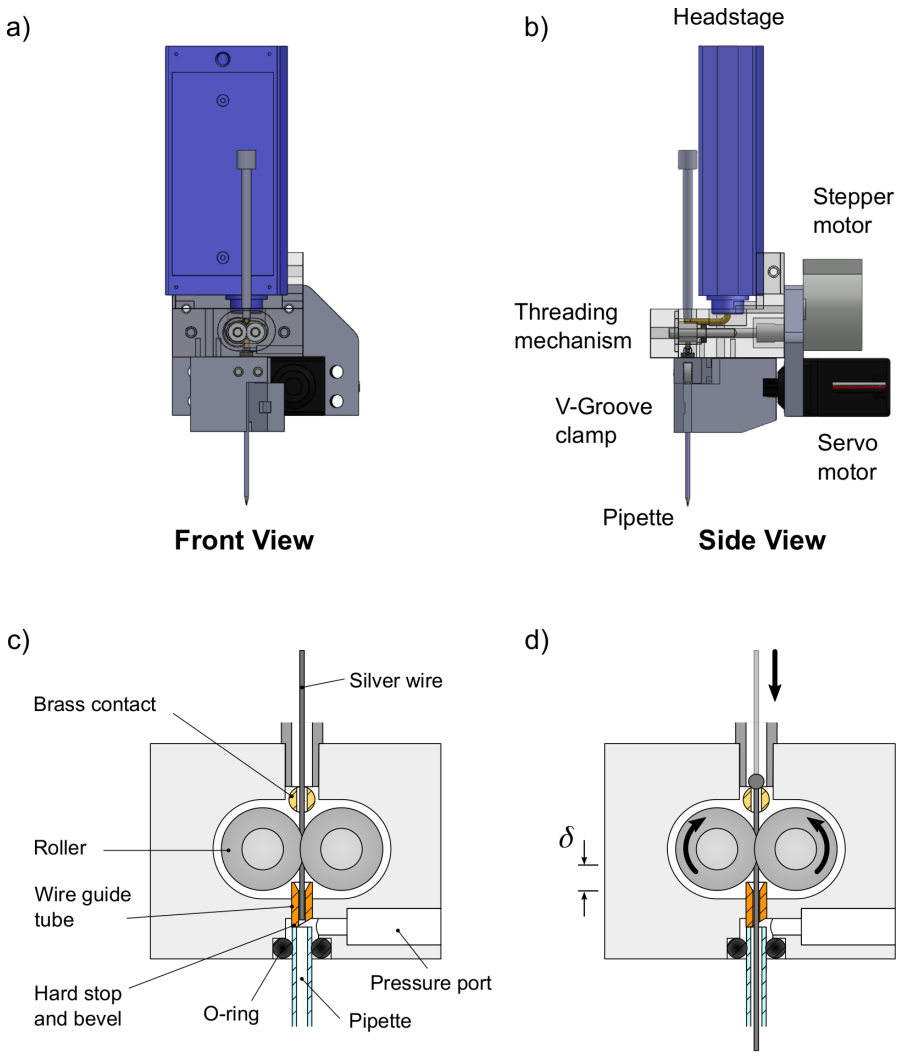

Figure 11: (a) A front view of the automated pipette holder attached to the recording headstage. (b) A side view of the holder showing the major components. First, a pipette is inserted into the v-groove and the clamp is partially closed by the servo motor. This aligns the pipette with the o-ring before insertion. The pipette is then inserted 4 mm into the o-ring using the programmable motor until it touches the hard stop. At this point, the v-groove clamp closes completely, physically restraining the pipette and providing precise pipette tip placement (c). Finally, the roller wheels in the threading mechanism are turned by the stepper motor and drive the wire down into the pipette until a solder ball on the end of the wire connects with the brass contact and the wire is fully threaded (d). The v-groove clamp is attached below the threading mechanism but is omitted for clarity in (c) and (d).

in the pipette tip position, is very sensitive to temperature changes causing drift, and is not mechanically stiff which allows it to flex and shift position when placed under small loads by the robot arm. These issues would be resolved by using a machinable, dimensionally-stable, ceramic material (e.g., Macor).

When deployed *in vivo* with pipettes manually inserted, this pipette holder achieved a good whole-cell recording yield (29.0%, n=20/69) similar to that obtained with the original autopatcher. After adding the remaining automation systems and software, the yield was reduced (9.9%, n=30/303), likely due to non-optimal pipette geometry or poor surgical preparation, which can affect the formation of the gigaseal, and due to the very small craniotomies (200-300 µm) which increases the rate of clogged and broken pipettes.

3.4.0.1 Wire Threading

Our first iterations of the wire threading mechanism had a small diameter guide tube that aligns the end of the silver wire with the center of the pipette, but the tube also causes the wire to buckle due to friction against the wire (Figure 8d), particularly if the wire is not perfectly straight and smooth. The design in Figure 10 eventually did function with 90% reliability after reducing the friction and using perfectly straight wires but was ultimately discarded in favor of our final design in Figure 11c-d. This design extrudes the wire into the pipette using a roller drive mechanism that has a much shorter wire compression length δ so the wire rarely buckles. This dramatically reduces the failure rates from threading and is now 99.6% reliable (in 530 trials). It is composed of two 6.35 mm diameter silicone rollers affixed to 3.175 mm shafts made of acetal homopolymer. The silicone rollers were also effective at trapping silver chloride particles that detach from the silver wire and become embedded in the rollers. This potentially helps reduce clogging although the rollers must be cleaned periodically for this to be effective. One of the rollers is driven with a small, low power stepper motor,

and the opposite roller is driven by friction against the first roller. The shafts are supported by simple journal bearings in the ABS plastic transmission housing with the shaft spacing chosen carefully to cause enough compression and friction between the rollers for them to rotate together and enough friction on the silver wire to drive it down into the pipette. If the wire threading mechanism is blocked for some reason, such as from a broken pipette, the silver wire simply slips between the rollers until the blockage is cleared, rather than buckling. This fail-safe mechanism is very tolerant to user error, allows imperfections in the straightness of the silver wire, enables simple wire replacement. It is also designed to allow the silver wire to be any arbitrary length to accommodate shorter or longer pipettes without requiring modification. This allows the use of wire specific to their application rather than requiring one with a special attached ferromagnetic bead, sliding contact, or a fixed length as in the previous designs. The rollers in the threading mechanism also eliminate the need for a sliding electrical contact and is replaced by the brass contact with a 500 µm hole in the end through which the wire is threaded. This allows the total length of the silver wire to be reduced to a traditional length and reduces noise in the recordings. After the recording, the rollers retract the wire from the pipette until the wire is fully retracted from the pipette but the end of the wire is still positioned within the guide tube, ready for the next insertion (Figure 11c).

As in previous designs, the wire guide tube (ID 500 µm) was positioned against the back of the pipette and has a smaller inner diameter than the inner diameter of the pipette to ensure that as the wire is extruded, it would not touch the sharp edges of the glass. This prevents scraping the surface of the wire and generating silver chloride particles that settle in the tip of the pipette and cause clogs. It also prevents threading failures by avoiding high friction between the wire and the edges of the glass. However, in our second design, the guide tube created a significant air restriction that ultimately reduced the yield and quality of the recordings. This is

another example of the tight interactions between systems. To reduce the restriction and isolate functions, a bevel was added to the guide tube and a separate port was added to direct air to the back of the pipette without forcing it to travel through the wire guide tube. This sufficiently reduced the air restriction and contributed to a dramatic performance increase (more details in Section 3.10). Part of the end of the guide tube was left flat to act as a hard stop against the back of the pipette. This was necessary to accurately position the tip of the pipette in the axial direction and ensure it reaches the correct depth in the tissue. A computer vision system measures the length of the pipette relative to this back edge compensate for variation in pipette length (see Section 3.6).

3.5 Precise Pipette Tip Positioning

One of the most critical aspects of a patch clamp recording is positioning the tip of the pipette in the correct region of the brain. If recording in the cortex, targeting the correct layer is essential and typically less than ±50 µm of error is tolerated in all directions. The whisker barrels in mice, for example, are approximately 100 µm in diameter, requiring higher precision, and each cortical layers ranges in thickness between 100-300 µm. Many subcortical regions of interest can be much smaller.

In addition, to improve tissue stability a very small diameter craniotomy is optimal (200-500 µm). If the pipette tip comes in contact with bone at the edges of the craniotomy, the tip will break and if the pipette is under pressure it can eject fluid and air at rates high enough to damage the tissue. If the pipette tip comes in contact with the dura at the edges of the craniotomy, it can clog the pipette. We initially chose a maximum target position error for the robot of ±100 µm positioning error in X and Y at the tip of the pipette with 95% confidence (±2 σ) and 50 µm in Z. These precision tolerances are different than the positional *stability* requirements discussed in Section 3.5.3.

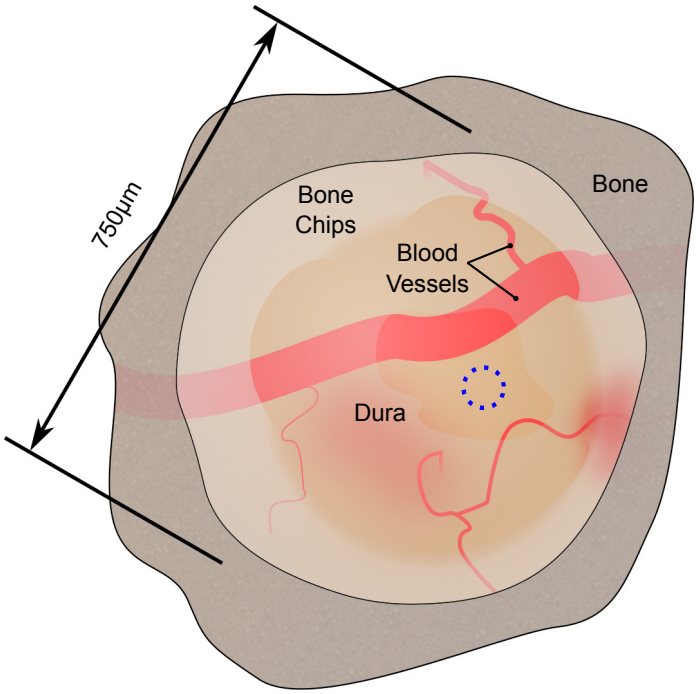

Figure 12: Drawing of a typical craniotomy. The blue dashed circle represents a 60 µm diameter target region. Inserting pipettes into bone or bone chips causes tip breakage and tissue damage. Inserting through the dura causes pipette clogging. Insertion through blood vessels also clogs pipettes and causes bleeding.

In the beginning of an experiment with the fully-automated robot, the robot inserts the first pipette into the holder and then the user visually aligns the tip of the pipette with the desired location in the craniotomy. The robot then continues with a patching attempt and retracts the pipette when complete. The pipette is then replaced ideally with the tip in the exact same position as the first. However, due to variation in X and Y, it won't be inserted into the exact same tract. To allow hands free operation, the robot must be able to position the tip of the subsequent pipette into nearly the same location. However, there is some error associated with the system, both random and systematic. The two main sources are variation due to the fabrication of the pipettes and variation in the physical constraint of the pipette holder.

3.5.1 Pipette Tip Manufacturing Error

Due to variation in the manufacturing process, there is variability in the position of the pipette tip relative to the central axis of the pipette. When the pipettes are pulled, the bearings supporting pipette are not perfectly coaxial. This tends to pull the pipette tip off-axis during the melting process. To characterize this error we measured the distance between the central axis of the pipette tip using four microscope cameras positioned orthogonally as shown in Figure 13. Each pair of facing cameras acquires a microscope image of the walls of the capillary and of the tip of the pipette.

Figure 14a,c show the view from a set of facing cameras. By combining all four cameras, the X and Y position error between the pipette axis and the tip can be calculated. The cameras were calibrated by inserting a pipette so that the walls of a glass capillary would be visible in both cameras and the central axis is found in both images and labeled as the reference axis. In this measurement, the tip of the pipette is beyond the view of the lower camera. There are slight angular offsets between the axis of the pipette and the vertical axis of the cameras which is measured and corrected

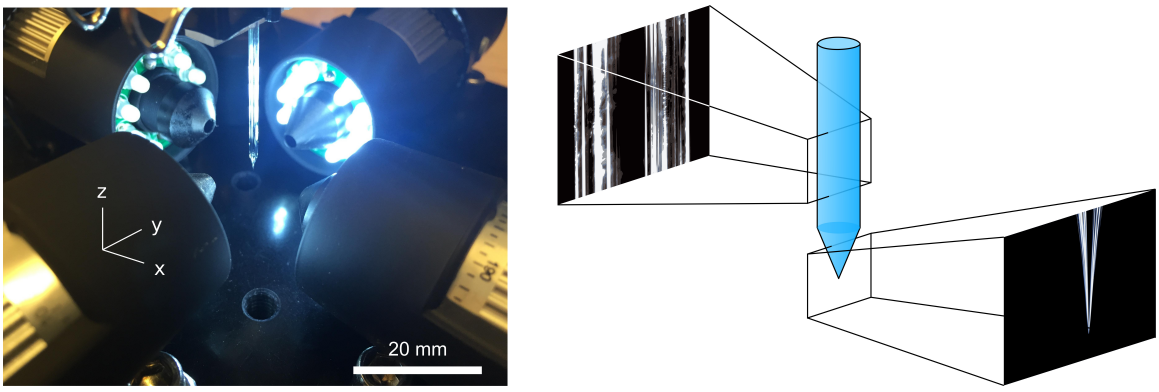

Figure 13: Photograph of optical measurement system measuring both the diameter and tip position of the pipette in the X and Y directions. The schematic on the right shows two cameras imaging the pipette to obtain the position in the Y direction. The other two cameras for the X direction are omitted from the schematic for clarity.

in the final calculations. This results in measurements of θ_{R_up}, x_{R_up}, x_{R_down}, and θ_{R_down} as shown in Figure 14. They define a true reference axis in both fields of view (red dashed line in Figure 15a,b). Later we use this relationship to measure the position of the pipette tip with respect to the axis of the pipette in view of the upper camera. This removes any variation in the measurement from the position of the pipette relative to the cameras.

The images were processed using canny edge detection with a 0.3 high threshold and 0.12 low threshold and then a best-fit regression was performed on the outermost white pixels representing the outer walls of the pipette. The algorithm also performed a histogram filter to avoid using the outermost pixels that were not within 40 pixels of column bin that contained the majority of white pixels. This eliminated pixels that were from an interior edge when there existed a vertical gap in the outermost edge. The pipette tip was found using the outermost white pixels in the canny image and the same regression to find best-fit lines for the taper (Figure 14). The pixel row position of the tip was found by searching for the white pixels with the lowest row number. The column pixel position was found by interpolating between the two best fit lines at the row number found previously. This proved to be a robust

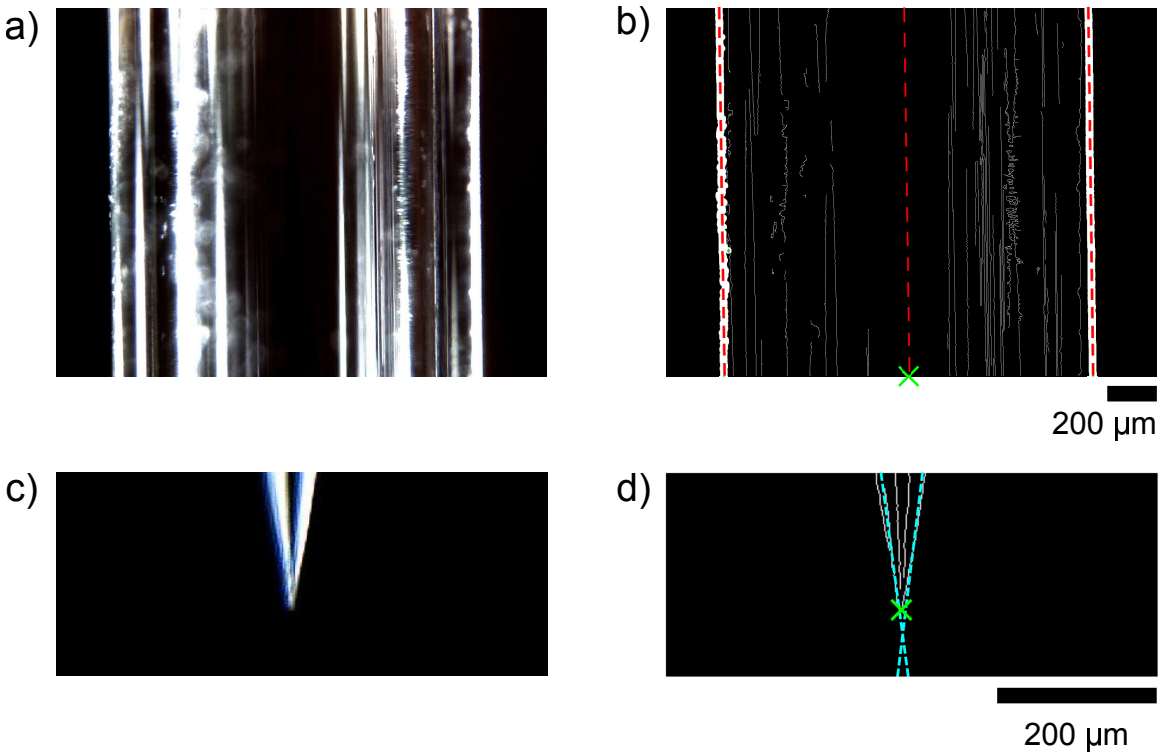

Figure 14: Microscope images of (a) the walls of the pipette and (c) the tip of the pipette. (b) Shows the processed image of the pipette walls performed using Canny edge detection and linear regression on the outermost white pixels to identify the outer edges of the pipette. (d) Shows the processed image of the pipette tip to identify the edges of the taper. The tip was located by finding the white pixels with the lowest row number (Y position in the frame) and taking the midpoint between the two best fit lines on the tapers at that row of pixels. This gives the X position of the tip in the frame.

method for finding the position of the tip in the image and was an improvement over the Hough line transform because of the averaging effect of the regression. It also reduced sensitivity to multiple parallel edges in close proximity that would give high counts in the transform for lines that crossed between the parallel edges. To avoid singular results from the regression due to the near-infinite slopes of vertical lines, the pixel data was rotated 90 degrees before performing the regression and then rotated back 90 degrees and overlaid on the image data (red and cyan dashed lines in Figure 14). The regression method was more accurate and less discretized in this case than the Hough line transform [59].

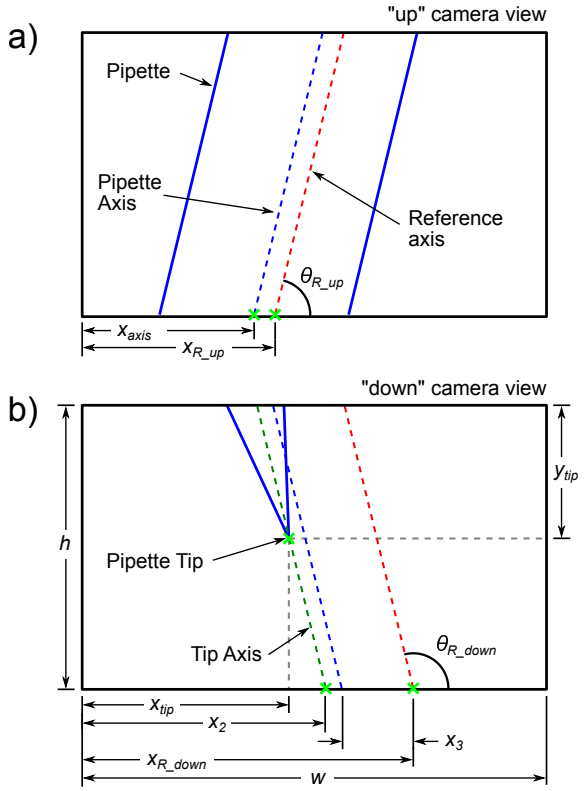

Figure 15: Schematic showing the variables used to calculate the distance between the axis of the pipette walls and the tip of the pipette. Measuring the pipette axis in (a) corrects for lateral and angular misalignment between cameras. A pipette is first placed in view of both cameras such that the walls of the capillary are visible in both cameras. The center axis of the capillary is found in both images from simultaneous image capture and subsequent image processing. This defines the reference axis in both images. All subsequent images measure the position of the pipette axis and corrects for any errors caused by variation in pipette position. Using the calibration angles and positions, the tip position relative to the pipette axis can be calculated.

Once the walls of the capillary and the tip of the pipette were found in the two images, the measurement had to be corrected using the calibration factors and reference axis found previously.

The X component of error is defined as the distance between the green dashed line and the blue dashed line in Figure 15b. If the pipette tip was exactly coaxial with the capillary, the tip would lie on the dashed blue line.

The error is calculated by

$$error = x_{R\_down} - x_3 - x_2 \tag{1}$$

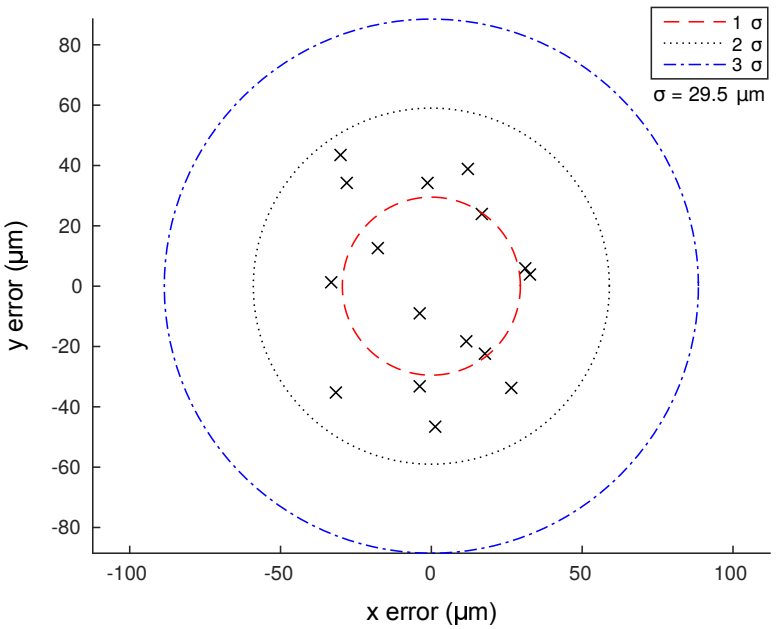

Figure 16: Plot showing the measured X and Y positions of the tips of the pipettes relative to the axis of the capillary. This error is caused by manufacturing variation in the pipette puller. 2σ is approximately 4% of the total diameter of the pipette.

$$x_3 = (x_{R\_up} - x_{axis})\frac{P_{down}}{P_{up}} \tag{2}$$

$$x_2 = (h - y_{tip})tan(\frac{\pi}{2} - \theta_{R\_down}) \tag{3}$$

P_{down} and P_{up} are the magnification powers of the two cameras. These powers were measured using a microscope calibration slide and scale the offset distance measured between x_{axis} and x_{R_up} to transform it into length scale of the lower camera. The error in the Y direction is calculated using the same equations and the other pair of cameras. Combined, the X and Y error give the total radial distance from the axis of the pipette to the tip of the pipette. These calculations assume that the angular difference between the reference axis and the measured pipette axis are negligible. We estimate the error in the measurement system to be approximately ±3 µm (resolution is 1.4 µm/pixel). Figure 16 shows the measured tip positions of 16 pipettes relative to the axis of the capillary wall. With a standard deviation of 29.5 µm, this is a large portion of the ±100 µm error allowance (2σ= 59 µm, for 95% confidence).

3.5.2 Collet Design Position Error

For the steel collet pipette holder design, we analyzed the effect of manufacturing tolerances in the collet on the position error of the pipette measured with respect to the capillary walls to isolate the error from error of the tip. The most significant error due to manufacturing was the Abbe error introduced by minor variations in the manufacturing of the o-ring glands with respect to the axis of the collet taper (see Figure 18h,i). To fabricate the collets (steps shown in Figure 18a-g), steel bar stock is placed vertically in a vertical CNC milling machine and the top o-ring gland is milled along with the outer taper of the collet without moving the stock. This ensures that the o-ring gland and taper are concentric to within the manufacturing tolerances of the machine (±0.005 mm, OM-1 Haas). However, the bottom o-ring gland cannot be milled in the same operation because it is on the opposite side of the part. After separating the partially finished collet from the stock, it is inserted into the milling machine upside down and the opposite gland is milled. To maximize the accuracy of the secondary operation, a sacrificial soft vise jaws were milled to receive the partially finished collet with high accuracy. However, this industry standard practice for fixturing still contributed approximately ±12.5 µm of error. Figure 17 illustrates the fabrication steps and the effect of the manufacturing error on the tip position.

The combined error from the manufacturing of the first gland (5 µm) and the fixturing error (∼12.5 µm) results in an angular error of 0.089 degrees which corresponds to an 81 µm error between the tip of the pipette and the center axis of the taper of the collet (Figure 17 ε_3). Figure 18 shows the measured error. Two orthogonally placed microscopes and similar image processing techniques discussed previously were used to measure the positional repeatability of the walls of the pipette. The total measured error is approximately ±80 µm with 95% confidence ($\sigma = 48.9$ µm). The collets

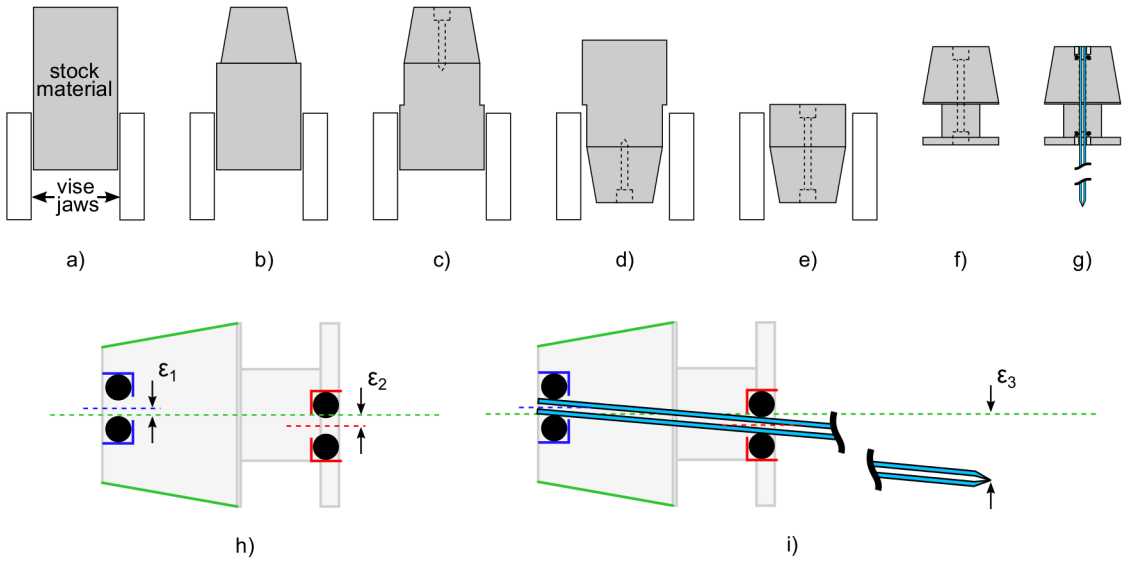

Figure 17: (a)-(f) Show the fabrication steps required to make the pipette collets. Between steps (c) and (d), the collet is removed from the vise and reinserted upside down. This step can introduce 12 µm of error, ε_2, between the axis aligned with the taper (green) and the axis aligned with the o-ring gland on the reverse side (red). ε_1 is the potential error due to manufacturing variation in the milling machine. ε_3 is the combined total position error of the pipette tip relative to the axis of the taper. This error is a projection based on the angular misalignment between the two o-rings and the axis of the taper.

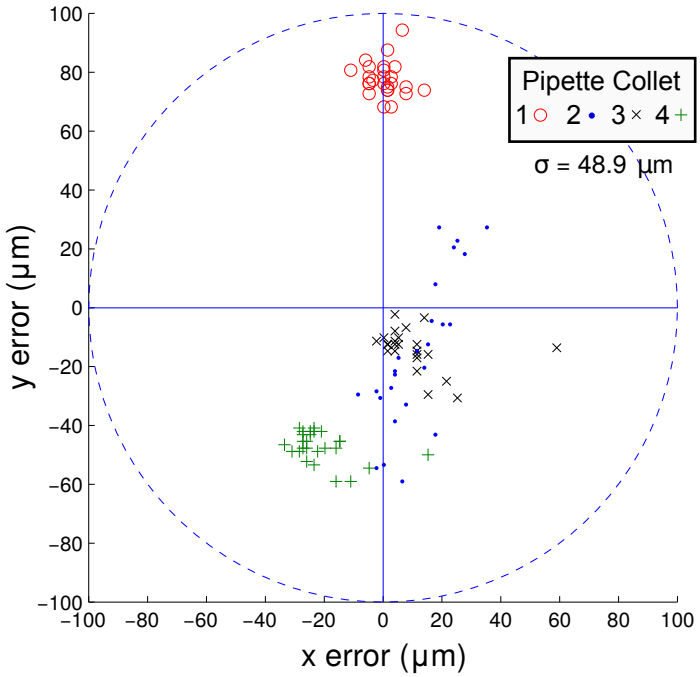

Figure 18: Plot showing the measured X and Y positions of the walls of the pipette between pipette insertions. Between each measurement, the pipette collet was removed from the holder, a new pipette and collet inserted, and another position measurement was made. The collets were not rotated during the exchange and were inserted in an random order fashion; the same collet was never removed and then immediately replaced. There are systematic errors from manufacturing processes in the collets as well as random errors from insertion into the tapered feature. The dashed circle represents the 200 µm diameter craniotomy

were inserted and removed from the pipette holder several times to measure the repeatability. In addition, because the collets were not rotated between insertions into the holder, the repeatability of the tapered mating surfaces for each collet also be extracted ± 26.4 µm ($\sigma = 13.2$ µm). This seemed sufficiently accurate to fall within a typical 200 - 500 µm diameter craniotomy but combined with the error from the pipette tip, the total error is ± 114 µm ($\sigma = 57$ µm).

This gave us some confidence in the repeatability of the collet positioning system so we proceeded to develop the rest of the supporting hardware to enable fully-automated trials. Upon completion, we tested the performance of the robot and found that due to the small size of craniotomies used, the pipettes would often clog

on debris in the craniotomy such as the dura and blood vessels. Approximately 38% of the pipettes would clog upon insertion, severely limiting the throughput and requiring frequent pipette changes. Manual alignment during a traditional experiment avoids these obstacles in the craniotomy and can achieve clogging rates below 10-20%. By using larger craniotomies, we reduced the number of clogged pipettes when using this design, but this increased the amount of exposed brain tissue which increases tissue pulsation due to heartbeat and breathing. This also reduces the success rate of gigasealing which was approximately 10% for all inserted pipettes for this design. It also reduces recordings stability as shown by the reduced average recording duration (4.1 min). For any given 200 µm diameter circular area, there are also several blood vessels on the surface of the cortex (Figure 12) that the pipette could pierce, causing bleeding and tissue damage [153].

3.5.3 V-Groove Position Error

To increase the positional accuracy of the pipette holder, we developed the v-groove constraint design shown in Figures 7a, 11, and 19. The v-groove design improves the accuracy of the system from ±80 µm to ±30 µm and dramatically reduced clogging from 38% to 18% (n = 437 and n = 142 trials respectively). The v-groove constraint requires a single precision part in contrast to the dozens of high-precision collets of the previous design. In this case, a 3D printed v-groove was sufficiently precise to position the pipettes with less than half the variability of the collet design (σ = 15.4 µm, a 68.4% reduction). Figure 20 shows the position repeatability of the v-groove. The v-groove also acts to align the pipette before insertion into the o-ring. As the clamp is partially closed, the v-groove aligns the pipette with the o-ring even if there is some variability in its initial position. This enhances the robustness of the pipette handling system by being tolerant of a certain degree of variability.

The total positioning error of the final design can be broken down into three

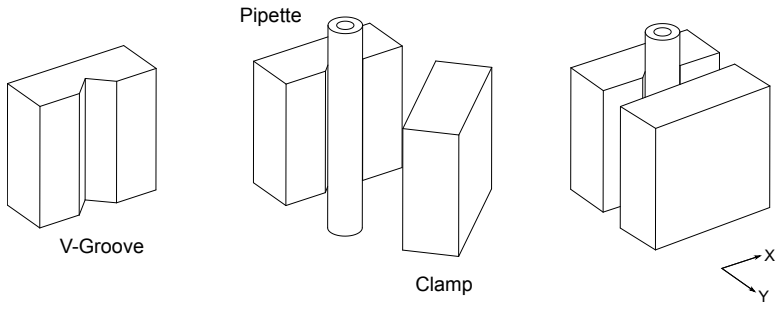

Figure 19: Schematic of the v-groove pipette constraint. The clamp is closed by torsional springs (not shown) and opened by a cam mounted on the shaft of a servo motor (see Figure 7).

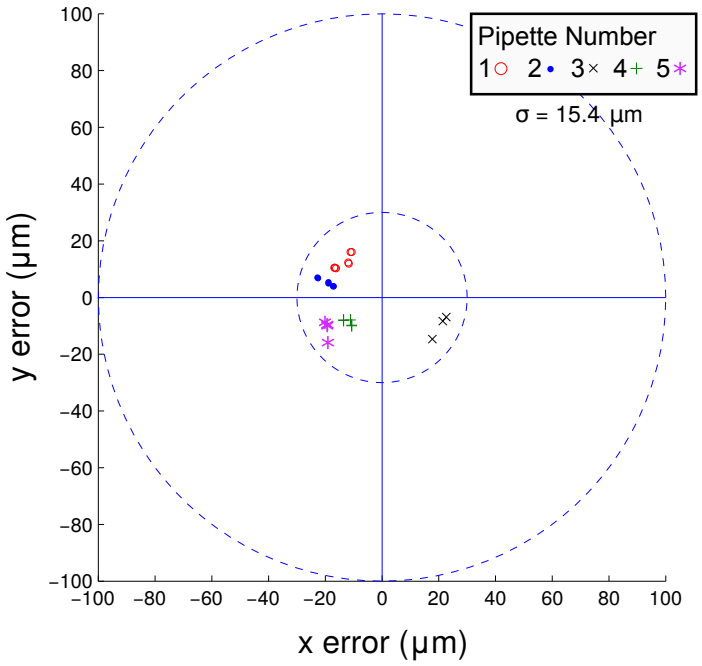

Figure 20: Plot showing the higher precision of the v-groove pipette holder. These measurements were taken with respect to the walls of the pipette. The 200 µm diameter circle represents the size of the craniotomy and the 60 µm diameter circle represents the size of the target region.

main segments: 1) repeatability of the v-groove constraint, 2) the variability in the pipette diameter and runout, 3) the manufacturing variation causing variation in the location of tip of the pipette. Other less significant sources of error include drift due to thermal expansion within the structural loop between the pipette tip and the brain of the mouse as well as creep in the plastic materials. The pipettes vary in diameter between 1.48 mm and 1.54 mm which corresponds to a systematic error of ±20 µm for a 90 degree v-groove. To control this error, pipettes were sorted by diameter into 0.02 mm bins limiting the error to approximately ±7 µm. The pipettes also have an elliptical cross section which can contribute to the error with a maximum difference in major diameter and minor diameter of 10 µm which gives approximately a ±3.5 µm error. Combining the error due to the v-groove and the pipette tip error and neglecting the diameter and runout error, the total error is ±66 µm with 95% confidence ($\sigma = 33$ µm). If we consider the uncertainty surrounding the true standard deviation of both errors given our sample standard deviations, the upper confidence interval for the standard deviation with 95% confidence the is $\sigma_{max} = 50.2$ µm(Chi distribution). Therefore, we can be 95% confident that 95.5% (2σ) of our pipettes will fall within a craniotomy of diameter 200.8 µm. However the cumulative effect of this 95.5% probability over the 30 trials in a typical experiment leads to the probability of at least one failure of 79%. It is therefore likely that at least one pipette will fall outside this diameter. With a 350 µm diameter craniotomy (3σ) we have a 99.7% probability that the pipettes will all fall within the craniotomy and a 26% probability of at least one failure during the experiment. These estimates assumes that the errors are normally distributed. In practice using craniotomies between 250 and 350 µm, we do see 1 - 2 failures where pipettes are clogged by the dura or break from contact with the bone chips around the periphery. This analysis does not include the probability of inserting the pipette into a blood vessel within the craniotomy window.

We also measured the creep in the ABS pipette holder when inserting the pipette

after the clamp had been in the open position for several weeks (Figure 21 orange). These measurements were performed using the same orthogonally positioned microscopes, with similar image processing techniques, and time lapse photography at a rate of one image every 20 seconds. The Hough line transform was too discretized for accurate sub-pixel edge tracking so a regression based algorithm was used to find the walls of the pipette as in Figure 16. The figure shows the stress relaxation of the ABS plastic after the force required to open the clamp is removed (7 N). During a typical pipette change, the clamp is opened and under load for 1.5 minutes which causes sufficient viscoelastic flow that the pipette will relax approximately 4 µm after the clamp is closed around the next pipette (blue). This requires approximately 40-60 minutes to stabilize. This far exceeds the desired <1 µm/hr drift requirement. However, this design was able to obtain 39 whole-cell recordings, including the data in Chapter 5, many of which were longer than 30 minutes, indicating a sufficiently stable system. One simple solution would be to close the clamp after removing the pipette during the 1.5 min pipette change so the force to open the clamp is only applied for a few seconds. The clamp could then be opened just before inserting the next pipette. This would help reduce the drift due to creep.

The drift likely contributes to the lower yield obtained with the robot as compared to the original autopatcher and also reduces the average recording duration. It was sufficient in this work as a proof-of-concept design and enabled the validation of the wire threading reliability, v-groove clamp precision, pressure control improvements, and automated pipette handling. This pipette holder could be further improved by replacing the ABS plastic with a dimensionally stable ceramic material (e.g., Macor) to eliminate creep, reduce thermal expansion effects, and increase the stiffness of the clamp. It would also increase the precision of the v-groove constraint and remain non-conductive for optimal noise performance.

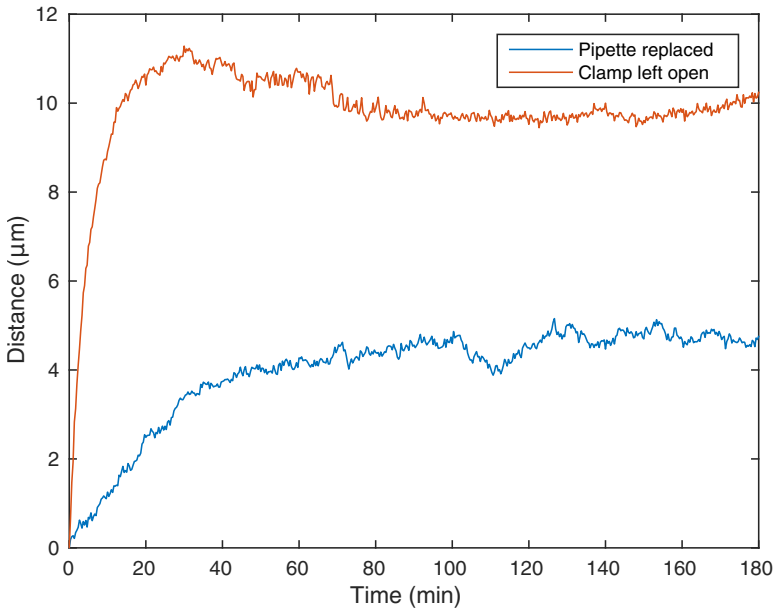

Figure 21: Plot of the creep of the pipette over time after inserting it into the v-groove clamp after the clamp had been left in the open position for several days (orange). The blue plot replicates the conditions during a typical pipette change. The drift was measured in the X and Y directions since these will be the most affected by creep due to Abbe error. The creep in the Z direction should be negligible.

3.5.4 Conclusions

We have established the need for high-precision pipette tip placement to be better than ±66 µm, showing a significant effect on clogging rates, and developed a v-groove constraint design that reduces the error in positioning the capillary walls to ±30 µm. The largest remaining source of error is the pipette manufacturing tip offset of ±60 µm between the center axis and the tip of the pipette which remains to be addressed and is similar to estimates made by others [28]. We characterized the probability of at least one failure due to placement of the pipette tip in a typical experiment of 79% for a 200 µm diameter craniotomy and 26% for a 350 µm diameter craniotomy which was similar to the 1-2 failures per experiment seen in practice. Several straightforward improvements also hold promise for reducing creep, thermal sensitivity, and increasing the precision of the v-groove. Overall, the design was sufficiently precise and stable to obtain the data presented in Chapter 5.

3.6 Pipette Length Measurement

Pipettes can vary significantly in length if not centered exactly on the heating filament when manufactured. This is normally accomplished using a physical hard stop. However, this assumes that the capillaries are uniform in length. The ends of the capillaries when cut leave behind sharp fracture edges that are only partially rounded during fire polishing. In addition, the overall cut length can vary from batch to batch. Rather than increasing the precision of the pipette manufacturing steps, we designed an on-line measurement system to compensate automatically for pipette length variation. This is performed by measuring the length of each pipette using two microscopes arranged as shown in Figure 22 and the resulting length is used to offset the programmable motor so that the tip of each pipette starts at the same Z height. Because the Z height of the brain is set manually with the first pipette, the difference in length between the first pipette and the subsequent ones is what constitutes the Z offset. This is added or subtracted to the distance to the surface of the brain that the motor will move. This ensures that the tips of all subsequent pipettes are at the same Z location as the first. It uses image processing techniques similar to those in Section 3.3. The robot arm inserts the pipette into the compliant clips that position it within the focal plane of the microscopes allowing precise length measurement. The resolution of the measurement system is 0.9 µm/pixel (∼200x magnification) with a measurement standard deviation of $\sigma = 8$ µm (n = 6 measurements). The retention brackets and compliant clips are mounted on the same frame as the cameras to minimize the size of the structural loop between the camera and the pipettes, ensuring that they are always in the same relative position despite insertion and removal forces and vibrations from the robot arm. The compliant clips are flexible enough to prevent pipette breakage and increase the reliability of the robot.

Alternatively, there are ways to detect the position of the surface of the brain

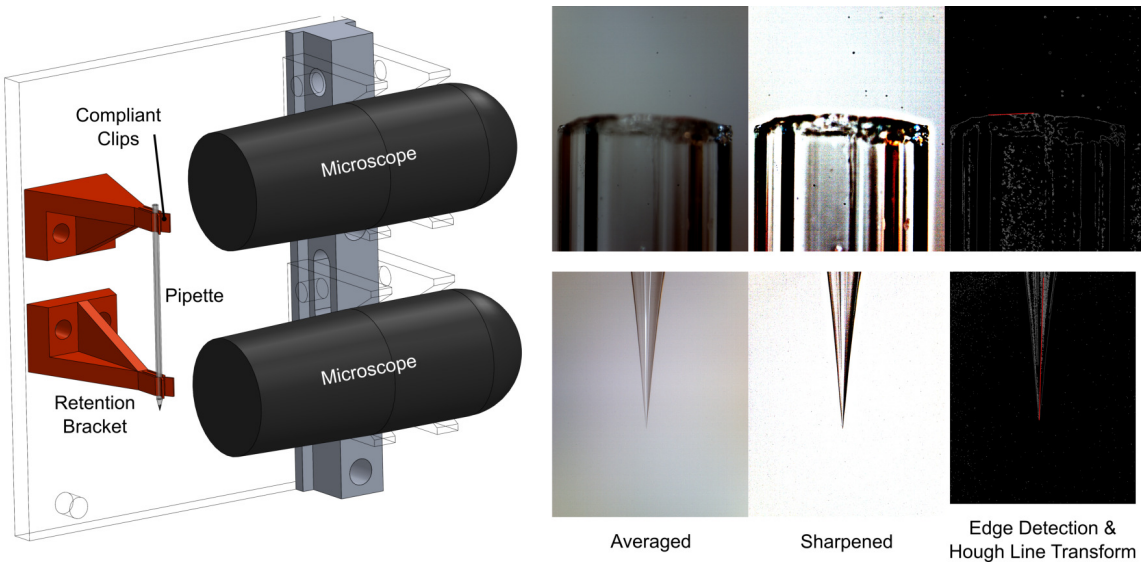

Figure 22: Rendering of the pipette length measurement system and the image processing steps to measure the length of the pipette. The extreme end points (high or low) of the red lines in the edge detection images are considered the "end" of the pipette in the measurement. The line transform makes the measurement more robust by requiring linear structure in the pixels to be considered part of the pipette. A white backdrop was used to enhance the contrast in the images against the black edges of the pipette. The robot arm in Section 3.7 inserts and retrieves the pipette from the compliant clips.

by observing the resistance increase from contact with the dura or heartbeat modulation [28]. However, if there is an error in these sensing modalities (e.g., due to tissue damage) and the surface is not detected, the pipette will be lowered until the next obstacle is detected possibly causing major tissue damage if not prevented by a redundant algorithm or limit. This risk of catastrophic failure will likely limit the robustness of this approach. For this reason, we pursued the optical measurement system shown which proved to be very reliable and precise.

3.7 Pipette Handling and Automation Controller

The design of the pipette handling system is largely determined by the overall architecture of the system. In the first version of the robot (Figure 5), the pipette handling system consisted of one stepper motor to rotate the pipette storage carousel, one linear brushless DC motor (100 mm travel) to move the headstage horizontally, motor that inserts the pipette into the brain, and one that raises the carousel to insert the collet into the pipette holder. However, the integrated and simplified nature of the design negatively affected the *in vivo* performance of the robot. With the segregated architecture, a new pipette handling system was developed to bridge the gap between the pipette holder and the storage area. The advantage of using a robot arm with multiple degrees of freedom (DOF) is that it allows the peripheral modules (storage, filling, length measurement) and the automated pipette holder to placed almost arbitrarily within the working area of the robot. The working area is shown in Figure 23. It also allows incorporating additional modules such as the length measurement module that was added after the initial design was implemented, which is more difficult with an integrated design.

Commercial robot arms are available that could manipulate pipettes (Baxter: Rethink Robotics, Universal Robots). However there are none available with the right combination of precision (<200 µm repeatability), footprint, or cost. In addition, the

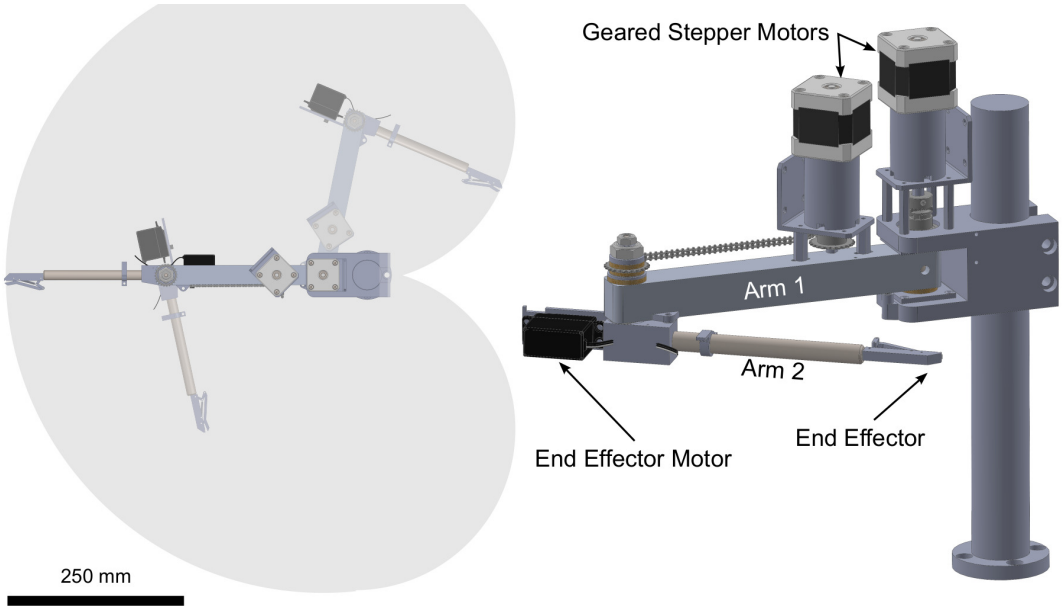

Figure 23: Pipette handling robot with two rotational degrees of freedom. Left: top view of the working area (grey) of the robot arm. Right: rendering of the robot arm.

robot arm must be compatible with the low noise and vibration free environment of the Faraday cage and vibration isolation table. To mount the robot arm on the table would likely require an option to power off the robot during recordings to prevent the high current supply to the robot from emitting noise into the cage. This option is not commonly used in industry and could be problematic, requiring multiple startup and shutdown cycles during an experiment. If the robot is mounted off of the air bearing table, then it must be able to adjust the path of the pipette when the table moves due to changes in weight distribution or air pressure. These challenges and order of magnitude increases in cost led us to develop the simple two DOF robot arm which gave us full control over the power options, footprint, workspace, and flexibility. The overall cost of this robot arm is approximately $2,500 as compared to $22-50K for bulkier commercial systems.

The robot arm in the final design is driven by two stepper motors (NEMA 17, 200 steps/rev) with 99.51:1 planetary gear reducers. The arm is operated open loop and has a full-step resolution at the end effector of 72 µm. The full extended length

of the arm is 457 mm. The repeatability was greatly enhanced by reducing friction using Teflon thrust bearings in each joint. The main bearings for the joints were conventional ball bearings chosen to withstand the torque exerted by the force required to insert the pipette at full extension. The planetary gear train included sufficient flexibility so that the arm would yield before breaking the pipette for small displacements (2 mm). If the arm experienced a torque greater than an certain threshold, a friction clutch in the elbow of the arm would slip or a brass pin at the shoulder would shear to avoid damaging the gear train or causing injury.

The robot is programmed using a vector graphics illustration application which was ideal given the 2D nature of the robot, shown in Figure 24a. The user can draw the obstacles in their working area to scale in the drawing and also draw the exact path for the robot to follow. The paths are translated by a custom interpreter that translates the X and Y coordinates of each point in the paths into ϑ_1 and ϑ_2 angles that the robot uses to follow that path with the end effector. Because of the symmetry of the robot, there are two sets of angles ($\pm$) that could correspond to a single X and Y point as shown in Figure 24b. The user can specify which configuration to use in the drawing program based on their physical constraints. The path shown in Figure 24a is translated into angular positions shown in Figure 24c and exports the firmware which can then be copy and pasted into the code that is flashed to the embedded microcontroller that controls the simultaneous motion of both stepper motors to follow the prescribed paths. The program also exports an animated GIF image for visual feedback of the paths interpreted from the drawing. This program made path planning and adjustment much more efficient.

The calculation of the angles given a set of X and Y points and the desired configuration ($\pm$), or Reverse Displacement Analysis, is the following. c_2 is defined as

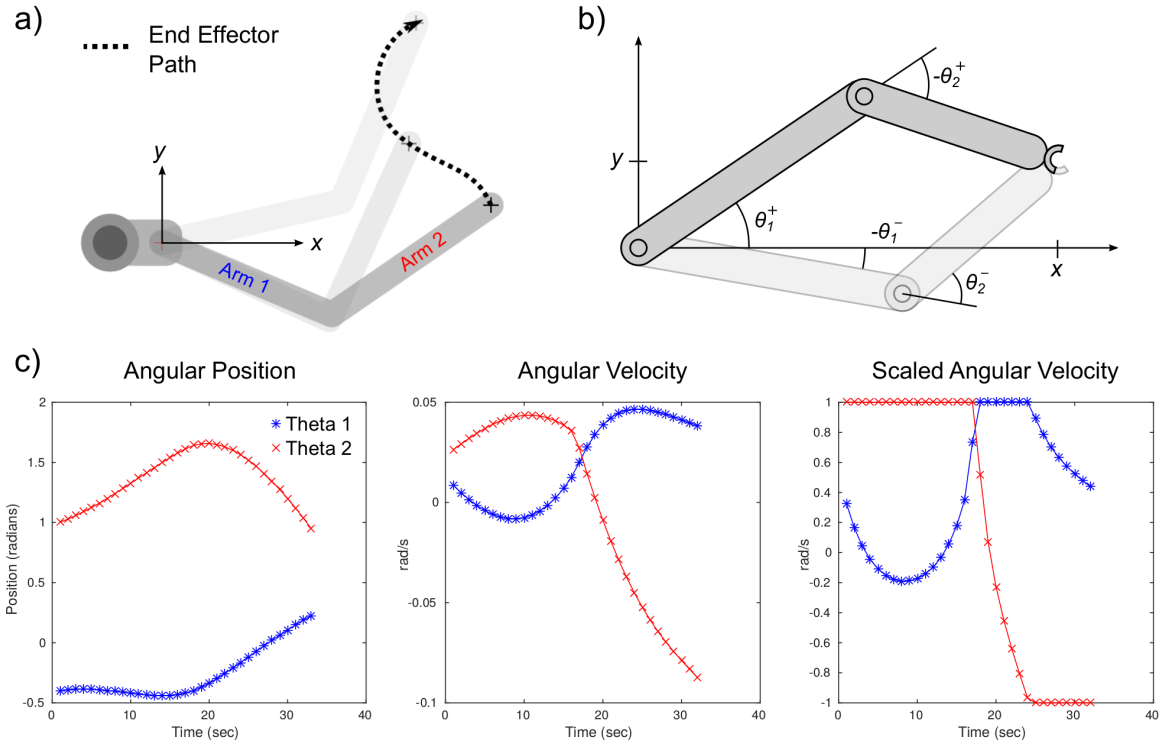

Figure 24: (a) Dotted line is the path drawn for the end effector to follow. (b) Shows the two configurations of the robot arm for a given end effector location. (c) Reverse displacement calculations that transform the Cartesian points in (a) into angular positions for the robot arm controller.

$$c_2 = \frac{x^2 + y^2 - l_1 - l_2}{2 l_1 l_2} \tag{4}$$

where l_1 and l_2 are the lengths of arm 1 and arm 2 in Figure 23 and x and y are the X and Y positions of the end effector relative to the shoulder joint. s_2 is defined as

$$\pm\, s_2 = \pm\sqrt{1 - c_2} \tag{5}$$

the solution for θ_2 is

$$\theta_2^{\pm} = atan2(\pm s_2, c_2) \tag{6}$$

Finally, θ_1 can be calculated by defining c_1 and s_1 and solving

$$c_1 = \frac{x(l_1 + l_2 c_2) + y l_2 s_2}{l_1^2 + l_2^2 + 2 l_1 l_2 c_2} \tag{7}$$

$$s_1 = \frac{y(l_1 + l_2 c_2) - x l_2 s_2}{l_1^2 + l_2^2 + 2 l_1 l_2 c_2} \tag{8}$$

$$\theta_1 = atan2(s_1, c_1) \tag{9}$$

$\theta_1^{\pm}$ is calculated using the corresponding $s_2^{\pm}$ and $c_2^{\pm}$.

In addition to the analysis of the ideal robot, the real robot incorporates simple on-line backlash measurement and compensation, simultaneous embedded motor stepping control, and full self-calibration essential for a functional robot arm.

The robot arm, by its design, has a very high stiffness in the vertical direction and the pipette insertion force is entirely supported by the bearings. To support possible use of the design for pipette holders positioned at an angle, the motors were chosen to have sufficient torque (4.7 Nm) to supply the insertion force required at the end effector (2 N) if, in the worst case, the pipette holder was completely horizontal

resulting in the insertion force being supplied entirely by the motor torque (worst case, 0.91 Nm).

The end effector is actuated using a servo motor and a two crank rocker kinematic mechanisms in series that provides near infinite mechanical advantage for gripping the pipette. The motion is transferred from the motor positioned at the elbow of the arm to the end effector using a stainless steel wire in tension. A return spring opens the end effector once the tension force is removed. Using this design, a high clamping force could be transmitted to the end effector. This is essential in the cluttered environment near the pipette holder where high torque motors and gear trains required to achieve high clamping forces would be too large. This design enables a large power density with a small footprint near the pipette. The cross section of the end effector is only 90 mm^2 enabling insertion into environments too small for manual operators such as in experiments with arrays of 12 or more pipettes [116]. One of the other limiting steps in performing multiple simultaneous recordings is the time required to change pipettes for each trial which could be alleviated by adaptations of this robot arm. By adding additional degrees of freedom to the end effector, the robot could accommodate various pipette arrangements.

The automation controller consists of three embedded microcontrollers (Atmel 328P, AtmelMega1280) with embedded firmware for controlling the valve timing, syringe pump, Peltier, and lead screw of the pipette filler, the motor on the storage carousel, the two stepper motors and end effector of the robot arm, and the wire threader and pipette clamp motors. Each system also has its own automated calibration routine and power down state to eliminate noise in the recording. The dozens of functions performed by these systems are controlled through serial communication with the master control computer (see Figure 3). A fourth microcontroller also controls the valves, analog pressure levels, and the BNC relay within the pressure control system. It includes firmware that allows the break in pressure ramp to be

interrupted when a resistance change has been detected by the break in algorithm and a command is sent from the master control computer to the pressure control system (discussed in Section 4.2.3). This results in a 30 ms response time between the resistance measured by the amplifier and when the valve is switched to atmospheric pressure. The preliminary results of this algorithm show improved access resistances using this method. This result is discussed in more detail in Section 5.4.1.

3.8 Pipette Filling

A pipette filling station must perform several basic functions: 1) thread the pipette over a microcapillary that dispenses the fluid, 2) dispense 1 - 5 µL of solution, 3) maintain the temperature of the stock solution near 0° C. It is also subject to a few constraints. It must avoid contaminating the pipettes to prevent clogs, have a speed similar to that of a human, and prevent bubbles from forming inside the tip of the pipette during filling. There doesn't currently exist a system for automatically filling pipettes.

The typical approach for filling pipettes is to thread a long microfil (World Precision Instruments, Sarasota, FL, MF28G67-5), or microloader (Eppendorf, Hauppauge, NY, Microloader) down inside the pipette and dispense fluid while the microfil is retracted to reduce the surface area of the microfil that is submerged in the fluid. The retraction is purported to reduce contamination by preventing the solution from washing off any contaminates on the surface of the microfil. The threading process, similar to the wire threading previously discussed, is a minor annoyance when done manually and a fair challenge for an automated system to perform automatically. The microfil is quite flexible due to its small diameter and easily buckles when placed in axial compression. The friction forces between the microfil and the sharp edges of the glass cause the microfil to buckle and prevent effective filling. Using rollers similar to the wire threading mechanism (see Section 3.3) would resolve this issue but

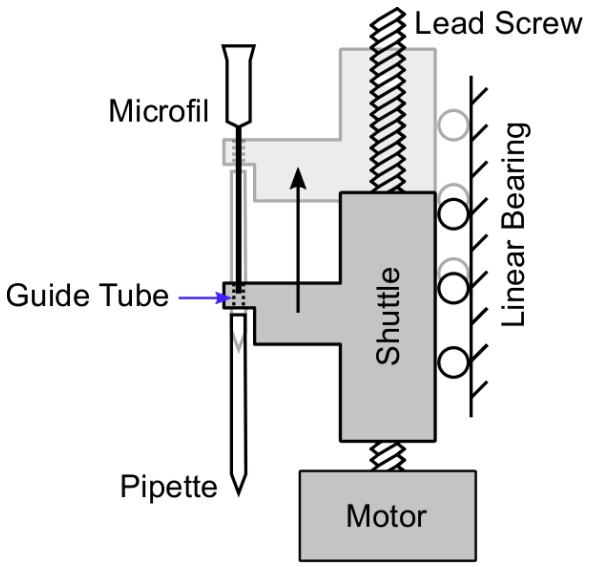

Figure 25: Figure showing the main moving components of the pipette filler. The cooling block surrounding the reservoir of the microfil, Peltier element, heatsink, fan, and pipette retaining clip are not shown for clarity.

it could also introduce contaminates. In addition, the microfil is too short to allow a roller mechanism to be positioned above the low friction guide tube (PEEK, ID 0.5 mm) and still reach the tip of the pipette. Nearly the entire length is inserted into the pipette. Despite placing the microfil in compression, it only buckled occasionally (6.6%) during experiments resulting in unfilled pipettes. An unfilled pipette is easily detected and removed by the robot and does not cause a catastrophic failure so this design was deemed sufficient.

To provide the linear motion to thread the pipette over the stationary microfil, a stepper motor and lead screw actuate a shuttle vertically on a sliding bearing as shown in Figure 25. Moving the pipette is simpler than moving the microfil, cooling block and the entire Peltier cooling assembly that maintains the fluid at 4° C.

The chemistry of the solution that is dispensed into the pipette is designed to match the intracellular pH, osmolarity, and concentration of the most common ions inside a neuron. In particular, adenosine triphosphate (ATP) and guanosine triphosphate (GTP) are added to enable accurate measurements of synaptic plasticity and to

maintain stable recordings. However, they are assumed to degrade quickly at room temperature in aqueous solutions (ATP - 50% degrades in "days" [50] or "several hours" [151], GTP 2% loss in four days in air) and the solution is conservatively kept on ice for the duration of the experiment. Therefore, the robot should keep the solution near 0° C. This is accomplished by using a 60 watt Peltier cooling element, heatsink, and fan (Adafruit, New York City, NY, 1335). It cools the intracellular solution to 2° C at steady state with the fan operating at a 70% duty cycle. However, the fan itself generates sufficient mechanical vibration to inject noise in the recording even with the most flexible standoffs. It was removed from the heatsink and mounted on a separate structural loop (Faraday cage) while still positioned immediately next to the heat sink with a small gap between them. Air reflectors direct the heated air away from the recording area and the cooling air was redirected from outside the Faraday cage to avoid disrupting the steady state temperature environment within the cage, thus reducing pipette drift.

To dispense 1-5 µL of fluid out of a microfil requires both pressure and volume displacement control. Figure 26 shows a schematic of the system. Originally we attempted a simple pressure-only control strategy but pressure control alone was insufficient. It is complicated by the need to withdraw the fluid from the capillary up into the reservoir after dispensing fluid (see Figure 27a (aspirating) and b (complete)). This prevents the dead volume in the capillary from remaining at room temperature. As the fluid is withdrawn using a pressure gradient, the fluid resistance through the capillary drops dramatically as air fills the capillary due to a much lower viscosity (1.8×10^{-5} kg/m-s vs. 1.7×10^{-3} kg/m-s for water) and causes the fluid to quickly be aspirated up out of the microfil and into the tubing, resulting in the loss of the intracellular solution (Figure 27c). This two order-of-magnitude difference in viscosity translates to a two order-of-magnitude increase in flow rate. The equation for laminar flow in a pipe is

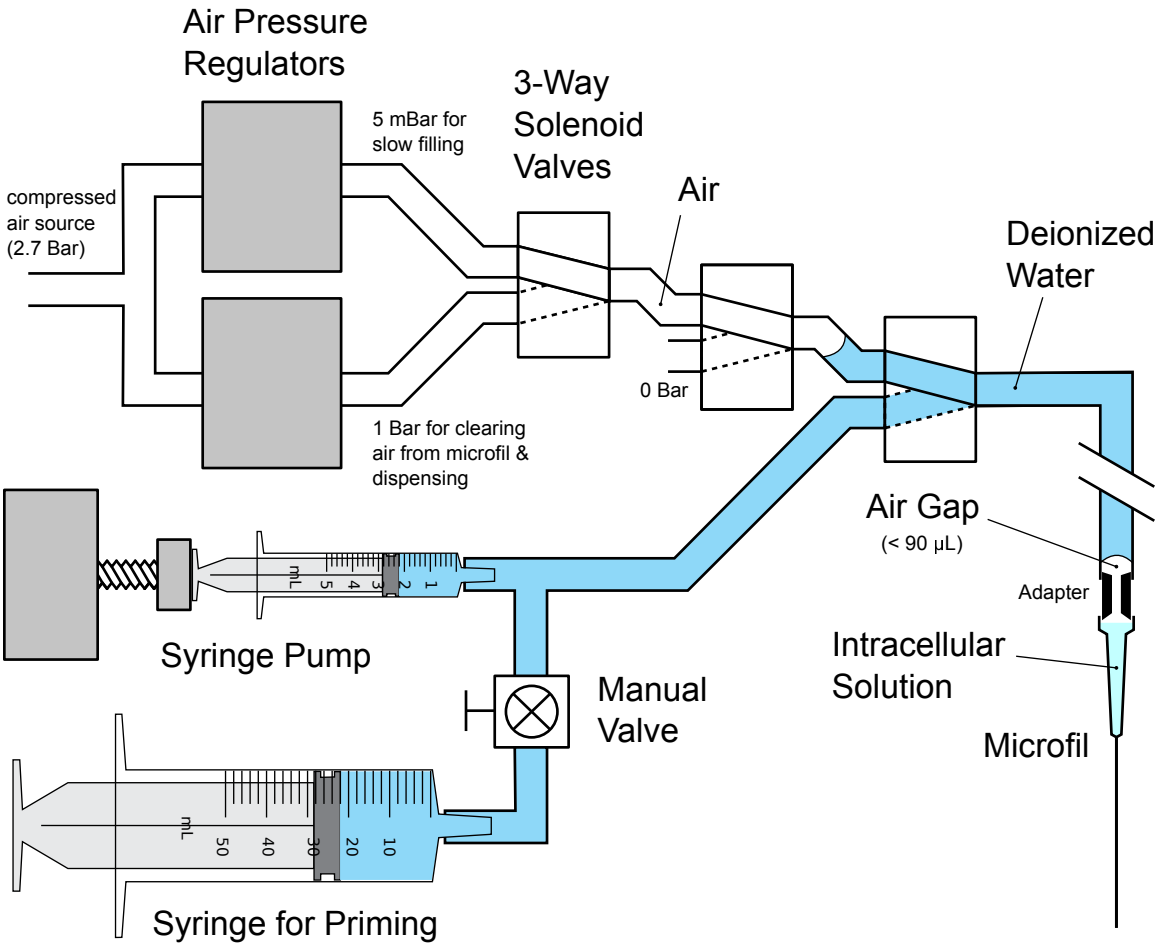

Figure 26: Schematic of the intracellular solution dispensing system. The fluid is dispensed through a combination of volume displacement from the syringe pump and pressure control from the regulators and solenoid valves. Over the course of the *in vivo* experiments it filled pipettes with 94.4% reliability.

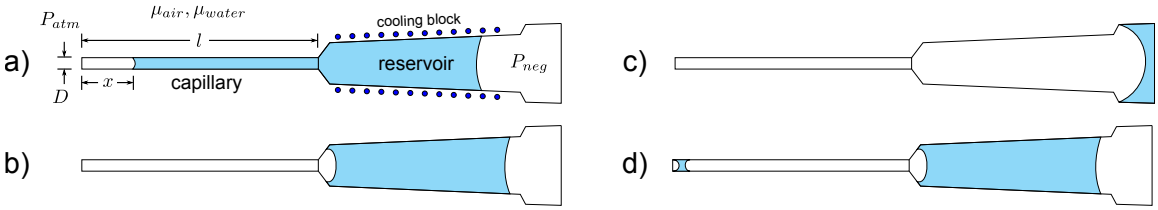

Figure 27: Schematic of the fluid dynamics within the microfil. (a) Shows the variables used to calculate the speed of the air-fluid interface. (b) Shows the ideal aspiration volume where all the fluid is positioned within the cooled reservoir and not at air temperature in the capillary.

$$Q_T = \frac{\pi D^4 \Delta P_T}{128 \mu l} \tag{10}$$

where Q is the flow rate, D is the diameter of the capillary, ΔP is the pressure drop across the capillary ($P_{atm} - P_{neg}$, constant in this case), l is the length of the capillary, and μ is the viscosity of the fluid. Variables are also shown in Figure 27.

To characterize this behavior, we modeled the position of the air-fluid interface as a function of time since we intended to use timed control of solenoid valves to apply the negative pressure. The flow in the capillary is laminar (Reynolds number ¡ 4) and we assumed negligible inertial effects. We also assumed that the fluid resistance in the reservoir was negligible due to a difference in internal diameter of nearly 10x. Because the pressure drop in a pipe scales inversely with the diameter to the fourth power with a constant flow rate, its pressure drop is 10,000x less than the capillary, all else being equal. We also assumed the flow rate was equal in both the air-filled and fluid-filled lengths of the capillary.

$$Q_T = Q_w = \frac{\pi D^4 \Delta P_w}{128 \mu_w l_w} = Q_a = \frac{\pi D^4 \Delta P_a}{128 \mu_a l_a} \tag{11}$$

Q_T is the total flow rate, Q_w is the flow rate through the length of the capillary filled with fluid, Q_a is the flow rate in the length of the capillary filled with air. l, l_w, and l_a are the lengths of the entire capillary, fluid filled section, and air filled section of the capillary respectively. This leads to a relationship between the pressure drops

across the fluid and air filled lengths

$$\Delta P_w = \Delta P_a \frac{\mu_w l_w}{\mu_a l_a} \tag{12}$$

and given that

$$\Delta P_T = \Delta P_a + \Delta P_w \qquad l_w = l - l_a \qquad l_a = x \tag{13}$$

and substituting into equation (12), rearranging gives

$$\Delta P_w = \frac{\Delta P_T}{1 + \frac{\mu_a x}{\mu_w (l-x)}} \tag{14}$$

Substituting equation (14) into equation (11) and combining with equation (10) yields

$$Q_T = \frac{\pi D^4 \Delta P_T}{128} \left(\frac{1}{\mu_w l + (\mu_a - \mu_w) x} \right) \tag{15}$$

Given that

$$Q_T = DV = D\dot{x} \tag{16}$$

where V is the average velocity of the fluid. By substituting equation (16) into equation (15) and integrating we arrive at a closed-form solution for the approximate position of the fluid-air interface as a function of time with a constant aspiration pressure.

$$(\frac{\mu_a - \mu_w}{2})x^2 + (\mu_w l)x - \frac{\pi D^3 \Delta P_T}{128} t = 0 \qquad 0 \leq t \leq t_l \tag{17}$$

$$x - l = \frac{\pi D^3 \Delta P_T}{128 \mu_a l} (t - t_l) \qquad t > t_l \tag{18}$$

which can be solved by finding the roots of x given a value of t. The relevant roots are where $x > 0$ and $x < l$. t_l is the time where the fluid-air interface has reached the end of the capillary and the entire capillary is now filled with air.

The probability density function in Figure 28b is calculated by assuming that l is normally distributed, which is similar to having an unknown volume to be aspirated, caused by drops on the tip of the capillary. The aspiration volume B is approximated by

$$B = \frac{\pi D^2}{4} x(t_{final}) \tag{19}$$

This assumes a constant duration t_{final} for negative pressure to be applied programmed into the pressure controller. The probabilities from the PDF of the normal distribution of l are mapped to the corresponding volume calculated using equations (17),(18) and (19) to generate Figure 28b and the change of variables technique.

Figure 28a shows the position of the fluid-air-interface x in the capillary as the fluid is drawn up into the reservoir under a constant negative pressure. The sudden jump in speed at 1.7 seconds is where all the fluid has been withdrawn and the air can now quickly flow through the capillary. If the negative pressure isn't released immediately, the entire reservoir is aspirated up into the tubing supplying the pressure and is lost (Figure 27c). While accurate millisecond timing control is certainly feasible, the time required to withdraw the fluid can be quite variable. After dispensing fluid in the pipette, a small drop of fluid will occasionally remain on the tip of the microfil which is then drawn into the capillary, increasing the time required to fully evacuate it Figure 27a. This variable fluid volume is problematic when trying to time the pressure control valves. Figure 28b shows the probability density function for the actual volume aspirated using pressure control, assuming that the volume of fluid that needs to be evacuated from the capillary is normally distributed and the negative pressure was applied for a fixed duration. The red line marks the volume of the capillary itself and anything above it has aspirated air into the reservoir. While some air is acceptable as shown in Figure 27b, it must be controlled. Figure 28b shows how the increase in flow rate skews the upper tail of the distribution, signifying that there is a high probability overall of aspirating too much air, resulting in catastrophic failures shown in Figure 27c. This sensitivity increases the risk of sample loss and reduces the reliability of the filler. A Monte Carlo simulation of the process with a normally distributed drop volume predicts 42% of aspirations will result in aspirating twice the required volume. This shows that pressure control is an unreliable and sensitive technique for situations with highly variable fluid resistances even with millisecond pressure control.

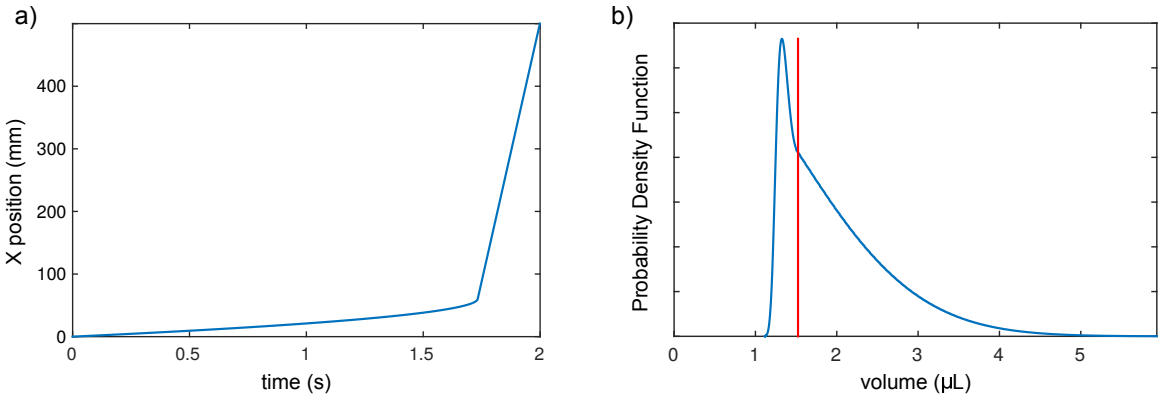

Figure 28: (a) Shows the position of the fluid-air interface within the capillary as a function of time under a constant aspiration pressure. At 1.73 seconds, all the fluid has been aspirated out of the capillary and air can move freely through, resulting in a much higher flow rate. (b) Shows the probability density function for the total volume aspirated by applying negative pressure to the microfil for a fixed duration. The variability is due to variation in the volume of fluid in the drops on the tip of the microfil that remain after filling a pipette. The red line shows the ideal aspiration volume using the fixed duration method.

A better approach is to aspirate the fluid using a fixed volume displacement to withdraw the fluid. A custom syringe pump was built for this purpose (Figure 26). Because a displaced volume self regulates as fluid is drawn up from the capillary into the reservoir, proportionally decreasing the drive pressure, it won't overshoot the desired volume and is very effective at controllably withdrawing the fluid. We empirically determined that withdrawing approximately 8 µL of fluid and having an air isolation gap (Figure 26) <90 µL, supplied enough negative pressure to withdraw all the fluid out of the capillary while minimizing the amount of additional air aspirated. Ideally, the volume of the air isolation gap should be minimized to increase the pressure difference generated for a given aspiration volume $P_{diff} = \frac{Vasp}{Vasp - Vgap}$. To attempt to increase the aspiration pressure simply by increasing the aspiration volume will cause the fluid in the reservoir to be aspirated further up into the tubing once the capillary is cleared, potentially causing osmolarity and concentration changes if it is combined with a drop of fluid from the supply tubing. Too small of an air gap, however, will increase the likelihood of contact between the deionized water and

the intracellular solution, upsetting the delicate osmotic balance in the intracellular solution.

The syringe pump alone failed to reliably dispense fluid, however. As the pump withdraws fluid from the capillary, occasionally small bodies of fluid remain in the capillary (Figure 27d) which, due to capillary forces at the tip, prevent the fluid from being dispensed by the pressure generated from a volume displacement. Applying a pressure pulse (1 Bar) reliably clears these blockages and allowing controlled, reliable dispensing if used with accurate valve timing. Because the flow resistance increases during dispensing, it effectively prevents it from overshooting the desired volume. After the capillary is refilled with fluid, the resistance is constant and millisecond timing of pressure pules is effective at dispensing accurate volumes. A schematic of the dual pressure and displacement control system is shown in Figure 26 and is based on the design by Innovadyne (Queensland Australia [8]).

To fill a pipette, the syringe pump first dispenses 8 µL of fluid to force fluid from the reservoir down to the tip of the microfil. Surface tension forces are sufficient to prevent fluid from exiting the tip at this point. While this is happening, the robot arm positions the pipette into the spring clips on the shuttle that align the pipette with the guide tube through which the microfil is threaded. As the shuttle is raised, the pipette is threaded over the microfil while five mBar of pressure is applied for three seconds to dispense a very small amount of fluid inside the pipette. This fluid quickly comes into contact with the moving inner walls of the pipette and is rapidly wicked away by the glass filament and down to the tip of the pipette under the force of gravity and capillary action. The pipette is filled during threading to prevent a large drop of fluid from bridging the walls of the pipette and essentially creating a bubble in the lower part of the capillary. While the pipette is moving, the tip of the microfil is more likely to come in contact with pipette before a large droplet is formed. The secondary, yet essential, benefit is that the intracellular solution flows down the

filament to the tip of the pipette and the taper of the pipette over time. This is important for the next stage where a higher pressure pulse (1 Bar, 100 ms) dispenses the remaining 1-2 µL of fluid into the tip. If the taper is not pre-filled, dispensing a 1-2 µL droplet of fluid can create an air bubble in the tip of the pipette. After the pressure pulse, the pipette tip is filled and the shuttle is lowered to withdraw the pipette from the microfil. Finally, 8 µL of fluid is withdrawn by the syringe pump to evacuate the capillary of the microfil during the waiting period before the next fill. The shuttle also acts as a physical hard stop to position the back of all pipettes to the same Z height before the robot arm moves them to the length measurement module and later to the pipette holder.

The robot can perform all the filling steps in about 12 seconds, approximately equivalent to the manual rate, with 94.4% reliability. As with all the modules in the robot, reliability was the key concern. The failures that did occur were either due to buckling of the microfil capillary during threading, or when all the fluid had been dispensed during a long experiment and operator failed to refill it. The filler is designed to use a specific disposable microfil (Eppendorf Microloaders®) to reduce contamination. They hold approximately 40 µL of fluid (sufficient for roughly 25 pipettes) when a low profile adapter is used to connect it to the tubing. The software currently allows the microfil to be easily refilled during an experiment or alternatively, a custom reservoir geometry could be designed by working with the supplier to increase capacity.

The impact of using the filler instead of manual filling on the performance of the experiment is currently unknown. Ideally, a control experiment would be conducted where the pipettes are filled manually to elucidate any possible effects. Future work should also examine the levels of contamination that occur between both manual and automated dispensing.

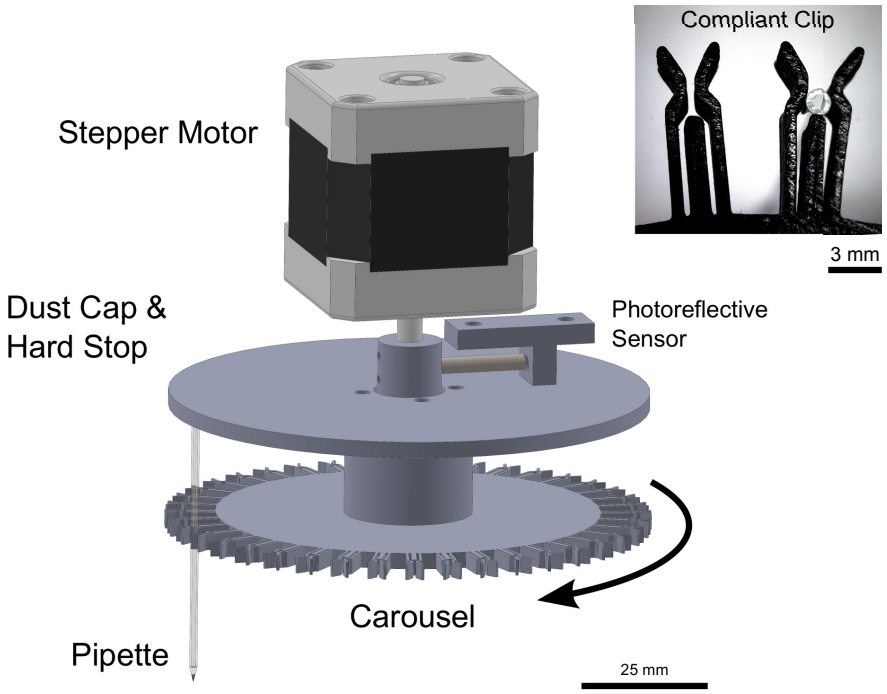

Figure 29: Pipette storage module. The dust cap prevents contaminates from entering the back of the pipette, the compliant clip holds and centers the pipettes for retrieval by the robot arm, and the rotational position of the carousel is calibrated using the photoreflective sensor.

3.9 Pipette Storage

The pipettes are stored on a motorized carousel shown in Figure 29. The design requirements for storing pipettes include preventing dust particles from contaminating the inside of the pipette and precisely positioning them so they can be retrieved by the robot arm. It consists of a stepper motor with a coupling that connects it to a dust shield that doubles as a hard stop when loading the pippette. The user inserts the pipette into a 3D printed ABS plastic disk with compliant spring clips to retain the pipettes (carousel). This design was also used to retain the pipette on the shuttle of the filler mechanism. Figure 29b shows the symmetrical geometry of the spring clips which automatically center the pipettes in the theta direction.

The symmetrical geometry of the compliant clip passively centers the pipette for retrieval by the robot arm. However, the 3D printed disk had inaccuracies in the

layer widths leading to significant Abbe error at the ends of the pipette. To reduce the effect, the carousel was positioned in Z so that the robot arm would grasp the pipette near where it is held by the carousel rather than near the ends of the pipette. A photoreflective sensor and reflective target are used to calibrate the position of the carousel and provide accurate angular positioning. The stepper motor rotates the carousel so the next pipette is in position for the robot arm to retrieve for the next trial. The storage system is 100% reliable due to its simplicity and can be scaled to store however many pipettes are needed, possibly in multiple radial rings. Currently it has a 40 pipette capacity. The storage capability could also be important for experiments where the cytosol is extracted after recording and stored in the carousel for later off-line analysis of mRNA expression or metabolic factors [144, 87, 18].

3.10 Pressure Control System

The two current methods to control the pressure applied to the pipette are by manually manipulating syringes or mouth pipetting. It is a highly skilled technique requiring weeks of training, and is subject to human variability and limitations. The most challenging step is applying the short pulse of suction during the break-in without damaging the cell. It is highly variable and non-quantitative. The original autopatcher work determined that the pressure control could be accomplished using three discrete pressures and an array of solenoid valves. Here we extend that work by adding electronic pressure regulators and analog pressure control, developed a feedback-controlled pressure ramp break algorithm, and added additional electrical control elements (schematic shown in Figure 30). These were implemented into a stand-alone automation system that has been adopted by dozens of other labs and allows labs to rapidly incorporate the autopatcher algorithm into their workflow. The pressure control system, known as the "Autopatcher Control Box," has been disseminated to dozens of labs by a startup company, Neuromatic Devices Inc. and

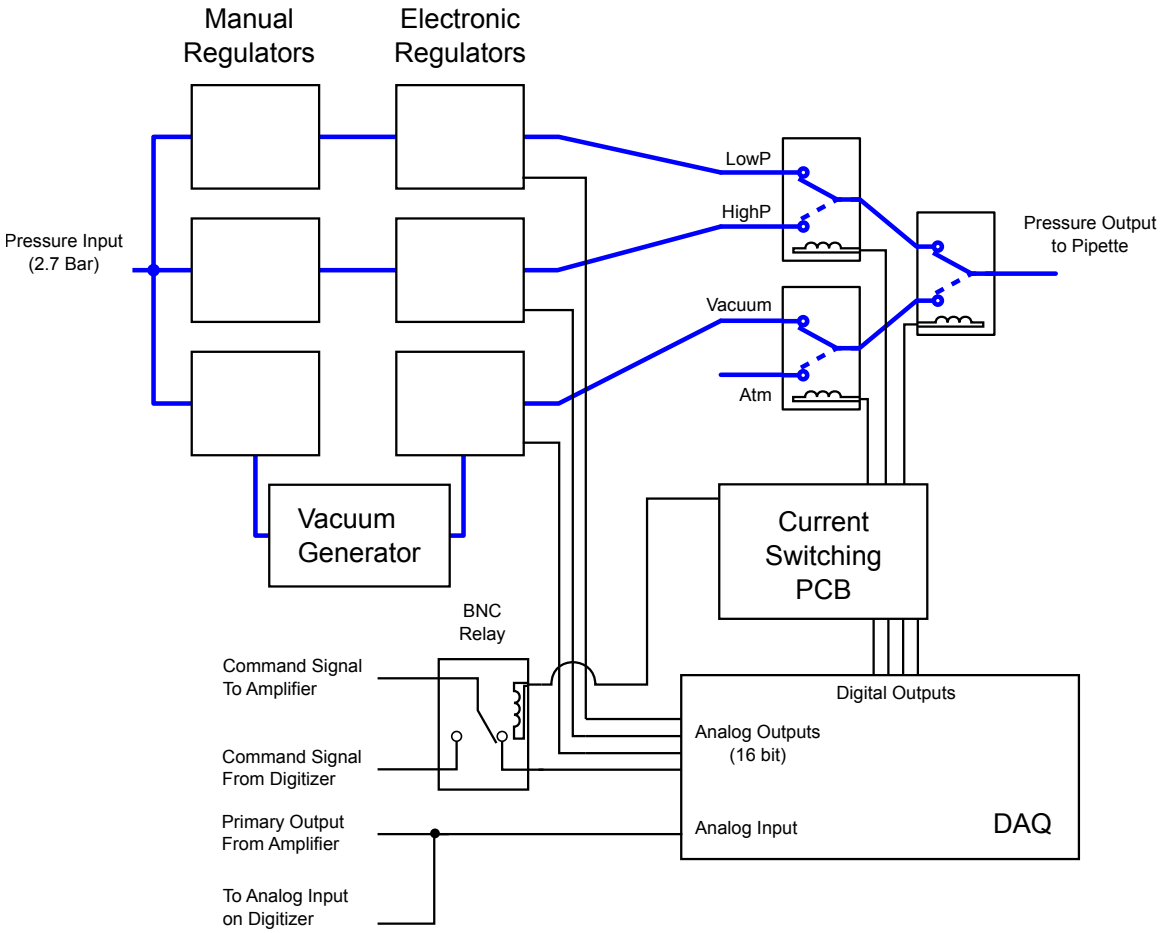

Figure 30: Schematic of the computer-controlled pressure control system used in automated patch clamp experiments. It enables algorithmic, analog pressure control and dissemination of optimal pressure protocols in software. The fast response times and exceptional repeatability exceed those of a human operator.

published [70]. The hardware and software are freely available to the community on our website www.autopatcher.org and are frequently updated as new techniques and improvements become available. The impact of this development effort is seen in its widespread adoption and replication by the community.

One of the contributions from the original autopatcher work involved defining the pressure specifications for successful algorithmic patch recordings. This was done using syringes to generate four pressure states (800 mBar, 25 mBar, -15 mBar, and -150 mBar). These pressures are similar to those that have been in use by others [47, 100], and were optimized for use with an algorithm. The manual regulators and

Table 4: Table showing the part numbers and adjustment specifications for the pressure control system. These provide the pressures used in the four pressure states used in the autopatcher. The manual regulators are adjusted to supply pressures within the input range required by the electronic regulators.

Manual Regulation	**Adjust to (mBar)**	**Electronic Regulators**	**Electronically Adjust to (mBar)**	**Patch Clamp Pressure**
McMaster 41795K3 (0-5 psi)	200	Parker 990-005101-002 (0-2 psi)	25	Low Pressure
McMaster 41795K3 (0-30 psi)	1500	Parker 990-005101-015 (0-15 psi)	800	High Pressure
McMaster 41795K3 (0-60 psi) & Air-Vac AVR038H	∼2700 (to give -500 vacuum)	Parker 990-005203-005 (0-345)	-15 (gigasealing) & -345 (break-in)	Low & High Vacuum
			0	Atmospheric

electronic regulators in this work are adjusted according to the specifications in Table 4 to automatically supply the required pressures.

Connecting a DAQ or the output from a microcontroller to the control pins on the electronic regulators also enables complete programmatic control of these pressures. This enables the development of pressure control algorithms that can precisely vary the pressure over time such as those detailed in Chapter 4 for autonomous break-in, as well as those developed by others using the control box, and enables a wide range of other manipulations to be performed algorithmically such as mRNA extraction [18] or macromolecule delivery [9]. As new algorithms are developed for these techniques, they can easily be transferred between labs in software rather than tedious training exercises. Electronic pressure control exceeds the ability of human operators by enabling higher precision and faster response times.

The pressure settings mentioned have been extensively proven *in vivo* but are actually a measure of the pressure supplied to the array of solenoid valves rather than the true pressure seen on the pipette. As alluded to in Section 3.4, the actual pressure dynamics at the pipette can be affected by flow restrictions in the pipette holder and capacitive pneumatic effects from the volume of the tubing. These effects are largely unquantified in most systems. Differences between systems could contribute to the variation seen in the styles of mouth pipetting or syringe manipulation techniques used by different experimenters [30]. The two most common break in methods use pressure ramps [30, 100], and pulses [69] but these are largely unsupported by controlled, quantified experimentation due to the manual way in which they are typically performed and the effort required to obtain a statistical sample. With the automation system presented here, repeatable experiments can be conducted to determine the optimal strategy for general experimentation, for specific cell-types, or for a given pipette geometry to obtain maximum yield.

The data collected in this work represents observations over many experiments using two different pipette holders with different pressure dynamics. The black measurement shown in Figure 31b and c are from the collet pipette holder design in Figure 10. It shows the slowest time constants for both applying negative pressure (Figure 31b) and returning to atmospheric (Figure 31c). We believe these dynamics contributed to the poor recording stability in that design by less effectively breaching the cell membrane during break in. If the membrane is only partially disrupted, it can reseal over the tip of the pipette, increasing access resistance, and reduce the quality of the recording. With faster negative pressure pulses, the patch of membrane is more fully disrupted and less likely to reseal. These slower dynamics are caused by the flow restriction in the pipette holder where the air is forced to flow through a 300 µm diameter 6 mm long wire guide tube. During a recording this hole is also filled with a 250 µm diameter wire reducing the effective cross sectional area by 56%. This

effectively filters the pressure dynamics when using this holder.

The pressure dynamics for the improved pipette holder design (Figure 11) are shown in pink and have nearly the same dynamics as the tubing alone (green) indicating that the holder has insignificant flow restrictions. This design directs the pressure through a separate flow channel instead of forcing it to pass through the guide tube. When the guide tube and flow channel meet above the back of the 1.5 mm pipette, the geometry was carefully chosen so that the guide tube could still align the wire with the pipette, but also minimize any flow restrictions (more details in Section 3.4.0.1).

We also investigated the effect of the tubing length on the system performance. By measuring the pressure output directly from the box (Figure 31ai) we determined that the electronic regulators were capable of very fast pressure control. However, after adding the tubing into the system (green), we see that the additional pneumatic capacitance decreases the performance significantly (tubing ID 1.6 mm, length 2.7 m). We also measured the pressure at the output of the box while the tubing was attached to see if flow resistance through the tubing was the cause of this decrease. This measurement was identical to the measurements at the end of the tubing indicating that the flow restriction was upstream in the system in either the solenoid valve or pressure regulator itself.

To separate these two effects, we also measured the release of negative pressure (Figure 31b) where the valve has disconnected the regulator from the fluid path and the only restrictions could be the tubing and/or the solenoid valve ports. The 3x improvement in speed between plots b and c indicate that the dominate flow restriction is in the regulator. To improve the overall performance, the two dominant effects must be addressed. 1) The length or diameter of the tubing must decrease to reduce the capacitance or 2) the flow capacity of the regulator must increase.

The final pipette holder design achieved break in successfully in 68.2% (30/44) of

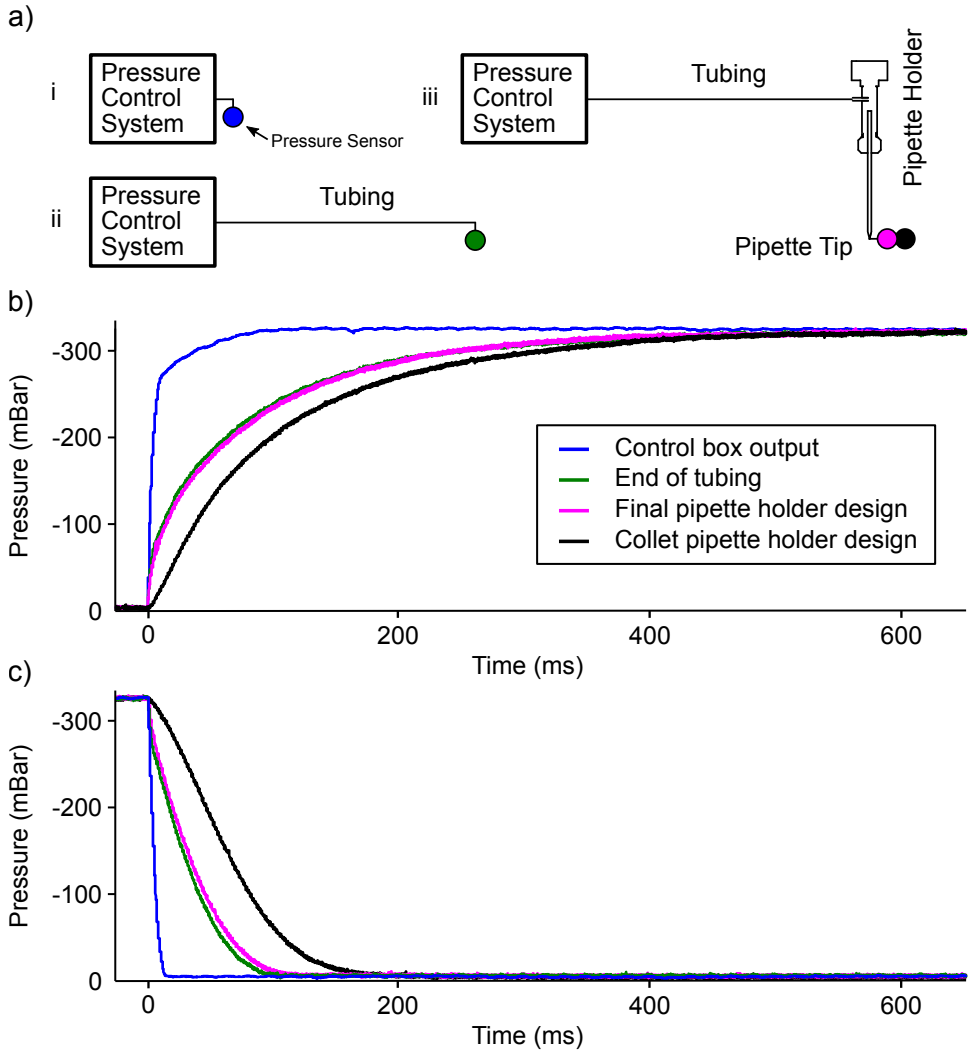

Figure 31: Pressure measurements at various locations in the pneumatic system. The pressure in the pipette was measured at the end of a capillary inserted into the pipette holder. (a) The locations in the system where the pressures were measured in (b) and (c). (b) Pressure dynamics when the pressure control system is switched to -326 mBar for break-in. (c) Pressure dynamics when the system is switched back to atmospheric pressure.

gigaseals, similar to the rates reported in the original autopatcher (83%) and elsewhere (67% [28]). The collet design achieved a similar success rate of 64.7% (33/51) but suffered from short recording durations likely due to partially broken membranes possibly caused by these slower pressure dynamics. This suggests that these dynamics represent the lower bound of pressure performance required for quality recordings (τ_{vac} =100 ms and τ_{atm}= 73 ms). The time constants for the final successful design were τ_{vac} =71 ms and τ_{atm}= 38 ms. These measurements also have implications for the pressure pulse methods that employ this specific hardware. The suction pulses between 100 and 1000 ms duration that are commonly used by the autopatcher algorithm will experience significant filtering and fail to reach the expected -345 mBar unless the pulse is longer than 400-500 ms. While the pulse method continues to report good function despite this effect, perhaps the performance could be improved further by using even shorter time constants and additional algorithm optimization.

In summary, we show the development of an automated pressure control system that enables algorithmic pressure control and characterized its performance, have shown a lower performance bound for successful pressure dynamics during break in that leads to stable recordings, and have quantitatively shown the dynamics of a system that achieved successful stable recordings. We also mention the improvement in access resistance due to the automated pressure regulation system and algorithmic pressure control. The pressure control system will enables future deterministic control algorithm optimization, new experimentation methods (such as pipette reuse [72]), and systematic dissemination of robust advanced techniques through repeatable hardware and software embodiments.

3.11 Automated Pipette Tip Geometry Inspection

Note: this system was not an integral part of the fully-automated patch clamp robot.

One of the main challenges in *in vivo* patch clamp experiments is fabricating

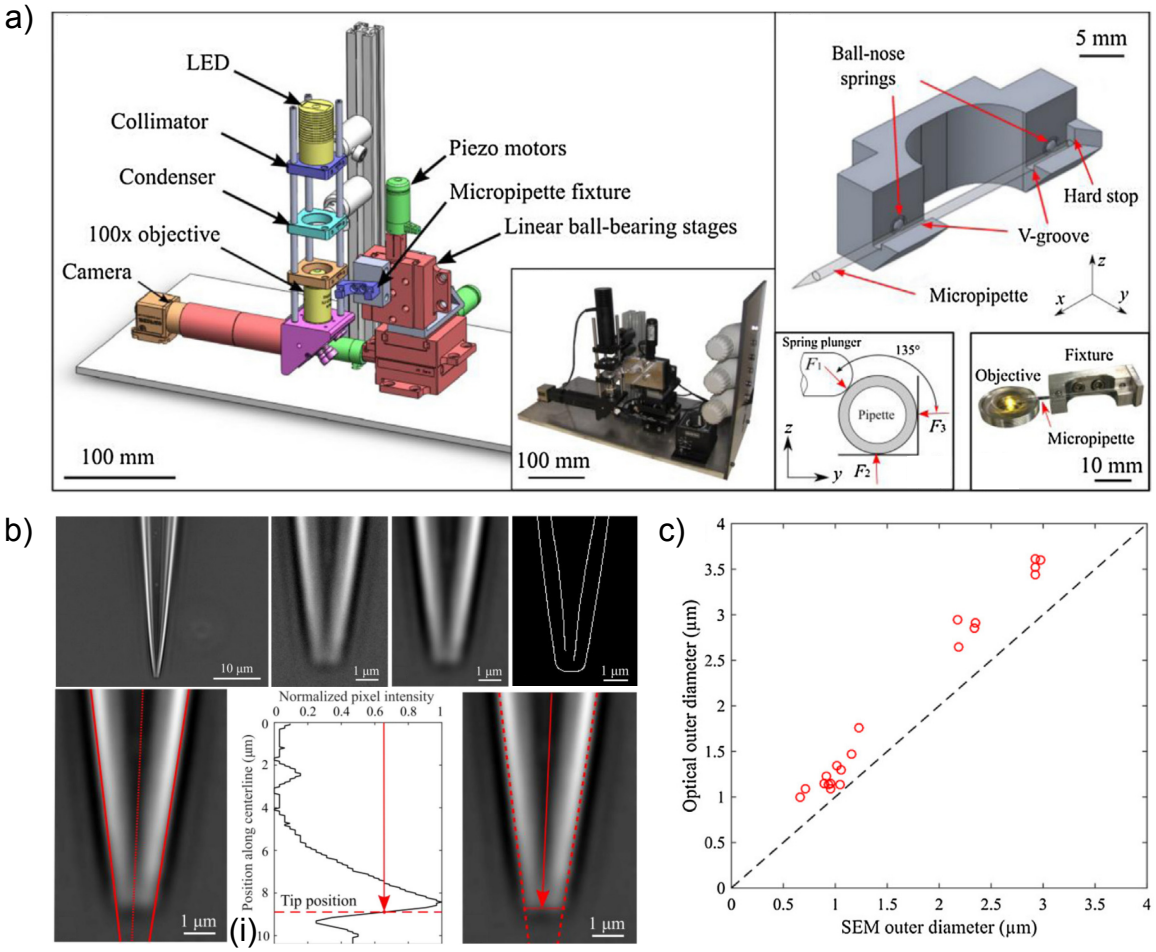

Figure 32: Summary of the automated pipette inspection system. It accurately measures the diameter of the pipette tip and taper angle to quantify the quality of a pipette. (a) A CAD rendering of the microscope, camera, light source, and three-axis manipulator. It also shows the kinematic fixture to position the tip of the pipette near the field of view of the microscope. (b) Microscope images of the pipette tip through various stages of processing. The image is acquired, cropped to the region of interest, averaged to reduce noise, processed using Canny edge detection, and processed using the Hough line transforms to find the edges of the pipette. The tip of the pipette in the vertical direction is found by locating the largest drop in the brightness along the mid-line of the (bi). The diameter is measured at this location. (c) Comparison between the automated inspection system and measurements taken using a scanning electron microscope.

quality patch pipettes to achieve high yield and good recording quality during the experiment [42, 99]. *In vivo* recordings in particular require a specific tip geometry to select for cell somata instead of detecting axons, dendrites, glial cells, or blood vessels. However the optimal size and shape is not well quantified. It is often described in terms of the shape of the optical aberrations seen when inspecting the ∼1 µm diameter tip under a bright field microscope. This characterization is largely qualitative and requires good visual acuity and training to recognize the optimal shape. The approximate diameter can be measured visually relative to an optical reticle, but is imprecise. Ideally there would be an unbiased quantitative method for measuring the geometry of the pipette tips to allow correlation with *in vivo* experimental yield to determine the optimal pipette shape.

A good pipette can also be described by a certain tip diameter and cone angle which are intuitively understood by experienced patch clamp experimenters but there does not exist a system that can quickly measure them quantitatively and accurately. There is some quantitative analysis about the optimal pipette geometry [137, 99] but no practical quantitative measurement system exists to gather the data to correlate geometry with yield. The experimenter must therefore be trained to recognize a good patch pipette visually over a period of several months of experimentation. In addition, it can require several days of effort to optimize the fabrication settings when the pipette puller drifts out of calibration. It requires several minutes to pull and inspect each pipette and the process quickly becomes haphazard due to the nonlinear effects of changing fabrication settings, manufacturing variability, and additional variability and bias from visual inspection. To optimize the geometry, between 25 and 100 pipettes are typically pulled an inspected. This process could be significantly accelerated by gathering unbiased quantitative measurements from each pull would enable autonomous multivariable system optimization.

We therefore developed an automated inspection microscope that measures the

diameter and taper angle of the tip of the pipette shown in Figure 32 [134]. It incorporates a 100x water immersion objective with a three-axis micropositioning stage and camera that can acquire high-resolution images of the tip of the pipette with minimal optical aberrations. After the user loads the pipette, it automatically locates the tip in the field of view of the microscope, adjusts the focus, and process the image to extract the inner diameter and cone angle. It measures the pipette diameter with ± 0.38 µm of error, and the cone angle with $\pm 5.45°$ of error (95% confidence interval) then compared to measurements made with a scanning electron microscope showing good agreement (Figure 32c). It uses the same image processing steps as before: averaged 10 frames, background subtraction, Gaussian smooth filter, Canny edge detection, and the Hough line transform to identify the walls of the pipette. The tip location was found using the column of the pixels down the center of the pipette and a user specified threshold which is triggered after the peak in image intensity (Figure 32bi). The diameter was measured between the two lines that designate the walls of the pipette and the taper angle is measured as the angle between the two lines. The pipette in this example has a cone angle of 16°. The pipette is manipulated using three piezoelectric nanopositioning motors and held in a spring loaded v-groove kinematic constraint.

While this system was not an integral part of the full automated patch clamp robot, it contributes towards transforming the art and qualitative nature of patch clamp experimentation to a quantified, systematic, and informatic science. The automated inspection system was developed under the author's guidance by Thomas Capocasale, Max Stockslager, Michael Simon, Yuanda Li, and Dustin McGruder for their senior capstone design project.

CHAPTER 4

SOFTWARE AND ALGORITHMS

The major contribution of the original autopatcher was the idea that the steps performed by a manual experimenter to establish the gigaseal could be performed by a simple computer algorithm. The two main algorithms contributed were the neuron hunting and gigasealing which significantly reduce the training required and achieved good yield *in vivo* [69]. Algorithmic control has the benefit of being readily transferable in software and is highly deterministic and quantitative, reducing biases and improving experimental consistency. The highly variable and low yield nature of *in vivo* patch clamp recordings would also benefit from this standardized, quantitative approach allowing optimal algorithms to be developed and disseminated.

Here we present the development of the remaining algorithms to fully automate the experiment. The hardware detailed in Chapter 3 forms the interface between the software and all the physical, electrical, and pneumatic tasks in an experiment and must be controlled by intelligent, adaptable, and robust algorithms with at least the same skill as a manual operator and ideally with increased speed and precision.

This chapter is divided into two sections covering the software architecture and the algorithms. The software architecture improvements include implementing the autopatcher algorithm in a state-machine architecture and developing a hybrid event-driven and state-machine architecture that greatly simplifies the development of new experimental protocols and enables multithreaded operation, non-blocking deterministic execution, and low latency algorithms.

Two new algorithms were developed in this work and include 1) determining the

moment for break-in and 2) the feedback-controlled ramp break-in method. The fully-automated system also incorporates the algorithms from the original autopatcher, with some minor adjustments, with their performance compared in Chapter 2.3. Here we will compare the performance of the new feedback method with the semi-manual break-in method used in the original autopatcher and replicated by another group who also implemented a simple automated version [28].

In addition to these main algorithms that could directly affect the performance of the robot, we developed dozens of other functions to automatically control the hardware and conduct the electrophysiology experiment. While these tasks do not typically require innovative algorithm development, they do require translating best experimental practices into computational logic and an execution flow-control system that allows it to react to the all the different situations that arise during an experiment.

4.1 Architecture

In the case of patch clamping software, there does not exist a standard software architecture that is designed to be easily customized for automated neuroscience experiments. Most software architectures are purpose built for specific tasks such as real-time control (RTXI, C++ [88]), automated microscopy (Micro-Manager, API [32]), or custom built using MATLAB (MathWorks, Natick, MA) [28], LabVIEW (National Instruments Co., Austin, TX) [69], or other languages.

The algorithm for the original autopatcher was custom built in LabVIEW in a procedural style with a single execution thread and a looping structure with a few state switches. This allowed rapid development in the graphical programming environment and algorithm optimization. However, as we added additional systems and user-requested features, this architecture quickly became unwieldy since all the

procedural code lacks modularity and hardware abstraction. In addition, any computational tasks requiring more than a few seconds would also block the GUI from responding to user input, leading to user frustration and lack of control. Our first step to alleviate both issues was to segment sections of the code at the natural divisions in the experimental protocol (e.g., pipette check, neuron hunting, gigasealing) and convert them to self-contained "states." This isolation is key in building a robust, modular code base where users can easily follow the execution in a piece-wise fashion, add new protocols, and benefit from reduced development time. This state-based design was developed in collaboration with Michael McKinnon, was also implemented in LabVIEW, and was included as part of the Nature Protocols publication [70] and is freely available on our website `www.autopatcher.org`.

This version also included hardware abstraction libraries to isolate the hardware specific implementations from the procedural code. There were several different versions of the pressure control system and many different actuators in use, so it became important that new algorithms were transferable without requiring rewrites. In the original autopatcher software, the hardware was integrated with the algorithms so six different versions of the original software had to be developed, one for each set of hardware (see "software" on www.autopatcher.org). The newest version allows the code for the hardware-specific functions to be interchangeable making the adoption process much more streamlined for custom hardware.

This new version of the autopatcher software still lacks a few additional features including a responsive GUI, and accessible parallel processing. These became increasingly important as more automation was added in the fully-automated design as several hardware subsystems need to operate simultaneously and without blocking the program. The logical architecture choice for this behavior is a multithreaded event-driven design where all code execution occurs in response to an event, either from a GUI widget like a button press or an event fired by a hardware subsystem

such as completing a motor move command. Using multiple threads, tasks and events can be handled in parallel without blocking each other or the GUI. After completion they then dispatch events to the main procedural code to continue execution. The main challenge with this architecture is that there is typically only a single function that handles all the events of that type. For example, if a GUI button is pressed, the event handler must use a switch case to select the appropriate code that should run depending on the which state is currently active. If the state code is included in the event handler, the consequence is that code that makes up a "state" is now scattered across dozens of event-handler functions and can be extremely difficult to follow, modify, and is not modular. As new states are added, the event-handler functions grow in size as new cases are added (there are 21 states in the fully-automated system). It also made testing isolated pieces of the code very challenging because to redirect the code to skip certain states (for example, so the robot would not have to recalibrate every time we tested an electrophysiological algorithm) required significant modifications to the code, which inevitably resulted in introducing additional bugs. This event-driven design was far less scalable, less maintainable, and made it very difficult to add new states.

How then, do we balance the need for procedural programming that follows the typical step-by-step protocol in biological experiments, with the improved performance of event-driven and parallel code? The answer lies in creating a specialized hybrid architecture that incorporates elements from state-machine and event-driven architectures. Unfortunately, this type of architecture is not supported by the built-in state-machine and event-driven architectures in LabVIEW. Our first attempt to develop the fully-automated robot software in LabVIEW resulted in poor performance and unreliability due to the high level of abstraction and architecture design constraints. Part of the reliability problems stem from the way LabVIEW hides threading functionality from the user in the graphical programming environment.

To develop this hybrid functionality we evaluated using C++ and the Qt signals and slots event-driven architecture. The key design feature that enables the hybrid design is the ability to redirect which functions handle the events without requiring hundreds of case structures with dozens of cases each. This allowed the architecture to direct the event to whichever state was currently active (rather than error prone case structures) and also forcibly prevents other states from responding to an event. This dramatically improves the modularity, generality, maintainability, and extendibility of the code. The way this is accomplished is by developing a parent class from which all the states in the robot inherit. Next, all the possible events sent to and from the GUI and hardware are routed through this parent class. The parent class essentially becomes an interface class for all the states. It contains a list of all the events and defines the name of the event handler that the user can use in their custom state. By standardizing this interface between all the states rather than letting them access the hardware and GUI directly, we can form the hybrid architecture in the state machine. The basic premise is that whenever a state becomes active, the state machine will connect all of the events going to and from the GUI and hardware to that specific state and disconnect all of the other states. This means that every state can have its own event-handler function for each type of event and that it will be the only state that responds to it. So rather than having all the code that responds to a specific type of event residing in a single function with case structure redirection, each state can have its own handler and that handler is guaranteed to be the one that responds once the state is active.

The end result of this conceptual shift is that all of the code that defines a state can now be written procedurally while receiving the benefits of an event-driven architecture. Since most experimental protocols have this step-by-step style, this makes development much more intuitive for end-users wishing to customize the software and

allows protocols and algorithms to be shared. Figure 33 shows a schematic of the architectures for the original autopatcher, the state-machine design in LabVIEW, and the final C++ version.

One of the other main conceptual rules we established was to force the user to highlight the areas of the code that control the transitions between states. In the previous versions, the decision to switch to another state would occur somewhere in the procedural code and would cause a change in the flow of execution. In the newest design, when a state finishes it returns with a decision code that the state machine uses to select the subsequent state. The state transition list specifies the subsequent state for each return code (Figure 33c, Next State 1 and 2). This allows the code to be redirected without modifying the code within the state and allows completely different experimental protocols to be executed simply by changing which states that will become active for each outcome. This makes the flow of the program much more readable and customizable. States can be added or removed from the execution flow easily and robustly. However, care must be taken when designing states, so that their code remains largely procedural to maximize reusability and readability. If anything more than simple loops or one or two branches of code exist within the state, it should be separated into multiple states and the branches added to the main state transition list so it is visible. One drawback of using a list to control state transitions is that the transitions can be difficult to customize. This is partially the intent of the design so that the transitions between states are simple and robust, but it requires workarounds for anything more complex. One option is to use flags set by another state to change the outcome in another state. These non-standard workarounds should be well documented if employed.

So far we have discussed the basic architecture for procedural-style automation programming using the signals and slots event-driven architecture and we will now

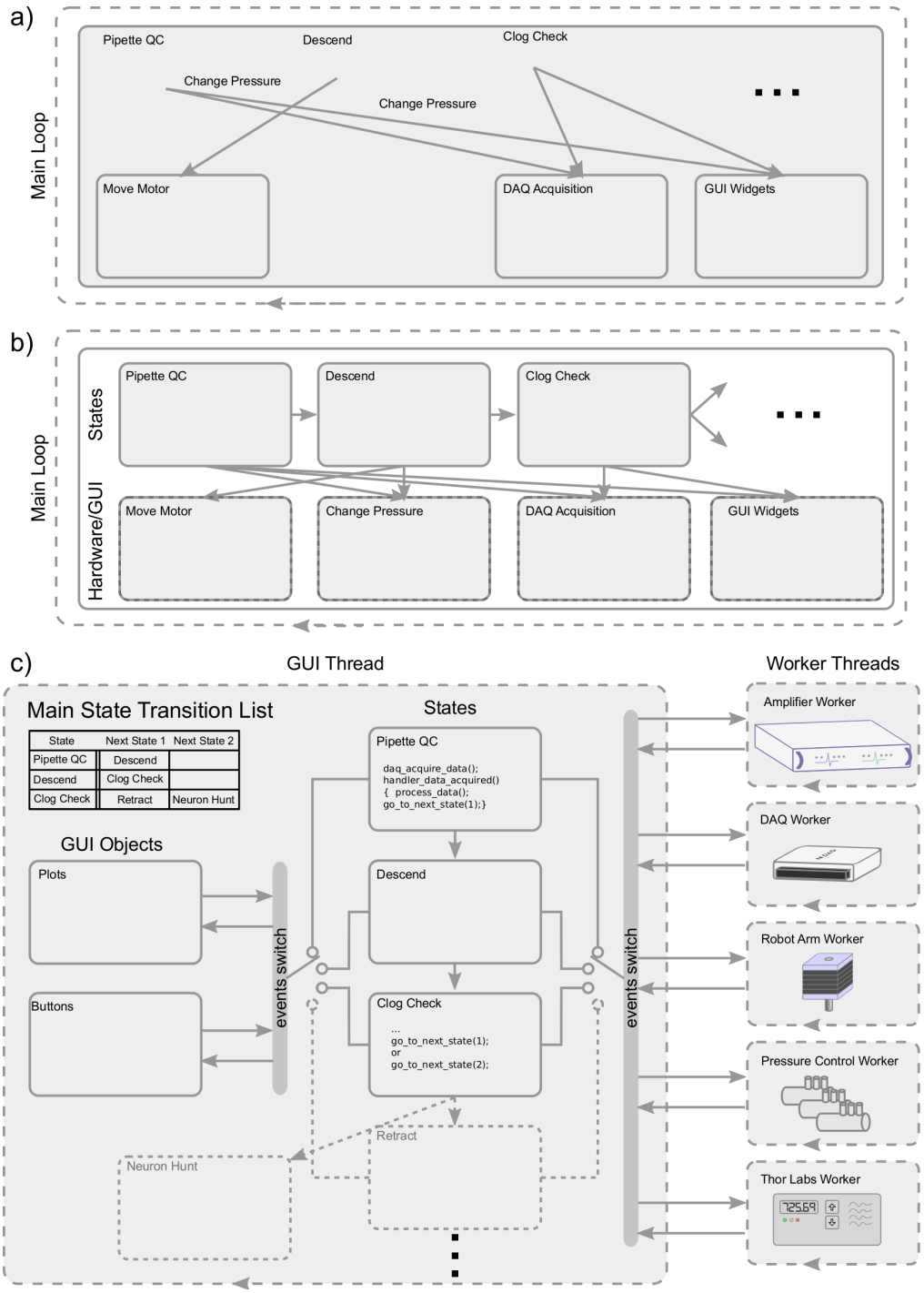

Figure 33: (a) Shows the first iteration of the autopatcher software architecture. The code was somewhat subdivided and there existed some hardware encapsulation. (b) The second version of the software with well-defined states, clear transitions, and fully isolated and interchangeable hardware blocks [70]. (c) The final architecture for the fully-automated system. It allows control of the order of state execution from a list, allows parallel processing, and maintains a procedural programming style while combining the performance improvements of multitasking and an event-driven architecture.

focus on the parallelization aspects. Automated experiments, and most biological protocols, are generally performed in a step-by-step fashion but can benefit from some level of parallel operation to improve efficiency or enable completely new parallelized experiments. In the case of the fully-automated system, there were several instances where multiple operations needed to happen simultaneously. Although true parallel processing was not needed, we employed multitasking extensively. For example, the functions that are used to control the amplifier are blocking functions which would cause the digital acquisition to halt during the pipette offset correction. To allow multitasking whenever there was a blocking function or time-intensive, low-priority computation being performed, they were sequestered into their own thread. Generally, algorithm execution is well within the real-time performance demands of the user, but hardware functions are much slower and require non-blocking functionality. Fortunately, the event-driven structure is very amenable for controlling asynchronous execution within separate threads. By allowing for blocking functions to operate within their own threads, this also simplified the requirements on the embedded software so an event-driven architecture did not have to be implemented on all the embedded devices.

Overall, the hybrid architecture allowed for efficient growth from the original five states of autopatching to the 21 states in use by the fully-automated system. The software design made a significant contribution to the stability of the software and significantly increased the reliability of the final system, critical to the performance of a system of this complexity. This final version of the software transects the event-driven, state-machine, parallel, and procedural software design paradigms and enabled the scaled development of the fully-automated robot and is a good platform for supporting systems of even greater complexity.

Despite the success in this new architecture, the largest disadvantage is the development language itself. While many scientists are skilled in programming as evidenced by the many open-source projects within neuroscience (Open Ephys, RTXI, PsychoPy, NeuroRighter, OpenWorm, ACQ4, Ephus [140], ScanImage) there are a very small percentage of electrophysiologists as a whole who are familiar with C++. Despite the conceptual advances in the architecture, this one issue will likely dissuade most neuroscientists from adopting it. However, the concepts are likely translatable to other languages such as python (PyQt). MATLAB has limited support for this kind of custom architecture and it would be challenging to implement this exact design, although other architectures could be used. The loss in computational speed from switching to these scripting languages would very likely be compensated for by the simpler syntax for most users. The main motivation to use C++ was the to leverage the high-speed execution, low latency, and low level control to maximize the performance of feedback-controlled break-in algorithm detailed in Section 4.2.3.

4.2 Algorithms

The original autopatcher performs a pipette resistance check, regional pipette localization, neuron hunting, and gigaseal formation tasks as shown in Figure 2. A semi-automated break-in algorithm was also investigated in the original work. However, it left the determination of when and how to break in and the detection of the break-in event, up to the user for each trial. This is a good approach for experiments that require flexibility but relies on the presence of an experienced electrophysiologist.

To achieve full automation we implemented an algorithm to determine the appropriate time to break-in, performs break-in using a novel feedback-controlled algorithm, and detects whether the whole-cell configuration has been achieved or the cell is lost. We also implemented a number of tests that run after break-in occurs to measure the resting membrane potential, holding current, capacitance, membrane resistance,

Table 5: The cutoff thresholds for terminating the gigasealing attempt. For example, if the resistance is not greater than 40 MΩ after 30 seconds after the positive pressure has been released, the pipette is retracted.

Required Resistance (MΩ)	at Time (sec)
40	30
100	90
500	120
1000	180

access resistance, rheobase, and spike amplitude. These are used to determine the quality of the recording and to indicate to the algorithm when to retract the pipette after a failure. We also implemented the necessary automation to control the current injection, bAC firing stimulation, visual stimulus, and ongoing quality control. We also developed algorithms or integrated existing ones to correct the pipette offset, bridge balance, and capacitance compensation.

4.2.1 Gigasealing

The autopatcher gigasealing algorithm performs the steps to obtain a gigaseal by releasing positive pressure, applying suction, and ramping down the holding voltage. The user would judge the quality and speed of the forming seal and decide whether to continue or terminate the attempt. To implement this assessment in a systematic automated fashion, a simple algorithm was developed to balance efficiency with the probability that a gigaseal will form during a trial. The purpose of this algorithm is to quickly reject cells that are not likely to seal, yet allow cells that are progressing enough time to successfully seal. Table 5 shows the resistance versus time thresholds where a trial would be terminated if the resistance does not meet the required threshold.

These thresholds match or are slightly less stringent than what a manual operator

would do during a gigasealing attempt. The emphasis with these values is to trade some efficiency (e.g., wait a little longer than an operator would) to avoid retracting the pipette in instances where an operator would have chosen to wait.

Future algorithms could also improve the rate of resistance increase by applying additional periods of negative pressure or by advancing or retracting the pipette 2-10 µm to help accelerate the seal formation in cells that are slow to seal, similar to techniques used in manual experiments [30]. These adjustments could be scaled based on the change in resistance seen during detection, which is an indicator of how far the pipette is from the cell, or on the initial rate of gigasealing. However, the emphasis in these algorithms should be to make minor, conservative adjustments that help compensate only for cases that are obviously sealing too slowly to avoid negatively affecting successful cases.

4.2.2 Determining Moment of Break-In

Once a gigaseal has formed, break-in must be attempted if a whole-cell recording configuration is desired. The focus of this section is to develop an algorithm that is highly reliable and reproduces the actions of typical human operator. However, because this decision has always been based on the experience of the operator there is very little quantitative data about the process or whether it impacts the success rate. There are different opinions about when break-in should be performed. One group suggests that breaking in immediately is optimal [30], while others suggest waiting 3-5 minutes for the seal to stabilize [18]. The simplest algorithm is to simply break in once it has reached 1 GΩ[28]. However, in the case where a cell is sealing quickly and a higher seal resistance is desired (2-10 GΩ) the algorithm should wait. Therefore, we implemented an algorithm that attempts to balance the need to break in and start the recording as soon as possible, with the desire for the gigaseal to reach its maximum potential. The overall average gigaseal resistance for our recordings using

this algorithm was 4.4 GΩ.

We developed the algorithm using historical gigasealing resistance measurements to test the robustness of different algorithms and whether they matched what an experimenter would choose during a manual experiment. It is a two-stage algorithm that becomes active after a single resistance measurement greater than a gigaohm is acquired. The first stage is designed for cells that seal slowly (>2 min to reach 1 GΩ) and the decision is made once a single measurement greater than 1.2 GΩ is acquired. This ensured a full 1 GΩ seal in the presence of measurement noise and because the time to reach a gigaohm is typically excessive for these cells, break-in is attempted immediately. None of the cells which fell into this category resulted in a quality recording. This could indicate that the seals were not very robust despite the gigaohm resistance or that the novel break-in algorithm is not ideal for these slow sealing cells.

The second stage of the algorithm is designed for cells that seal quickly (<2 min). We designed this algorithm to balance the need for efficiency and the desire to allow the seal to stabilize. To quantify the stability of the seal resistance, we used the first derivative of the resistance measurements and two different averaging windows to determine what an experimenter would consider stable. We optimized the algorithm using historical gigaseal resistance traces followed by *in vivo* testing.

The algorithm begins monitoring resistance measurements as soon as gigaseal has been reached. After acquiring 30 measurements over ~30 seconds, it calculates the first derivative using a linear regression on those 30 points. As each new resistance measurement is acquired, it recalculates the first derivative D_1 for the most recent 30 points, essentially using a moving window for calculating the first derivative. These derivative values are stored in an array and the maximum value in this array D_{max} is updated with each new addition. Finally, the percent change of the most recent derivative value is calculated relative to the global maximum derivative value. The

decision to break in is made once the derivative drops below 50 MΩ/s and when the most recent derivative value is less than 50% of the maximum derivative value in the array.

The algorithm also requires that another first derivative D_2, calculated from the five most recent resistance values, is below 1 MΩ/s. This allows a comparison between the lower noise, long average of the first metric with this more responsive metric that uses a smaller averaging window. We also investigated replacing this metric with a requirement that the second derivative of the five most recent points be less than 1 MΩ/s^2. These two metrics behaved similarly and the first derivative metric was ultimately used in the experiments.

These three conditions ($D_1 < 50$, $\frac{D_{max}-D_1}{D_{max}} \cdot 100 > 50$, $D_2 < 1$) were very reliable and allow the majority of the potential seal resistance to be reached and efficiently terminates gigasealing without requiring the slope to reach zero. The seal for many cells never stabilizes completely (zero slope) so a positive threshold should be used and adjusted according to the taste of the experimenter to allow the algorithm to be tuned to either achieve maximum seal resistance or to break in quickly after the gigaseal is formed.

The algorithm also includes a provision that would allow the robot to proceed to the membrane test state if the resistance drops below 500 MΩ after previously reaching 1 GΩ. This successfully handled spontaneous break-in events during the experiments. The algorithm does not handle cells that break in spontaneously without first having reached a gigaohm, but these recordings are typically lower quality and rejected by the quality control algorithms.

The majority of the higher quality and stable recordings in our experiments came from seals that formed within the first 100 seconds of gigasealing and that reached resistances >2 GΩ(Figure 34).

These plots indicate that the maximum gigaseal resistance is a good predictor

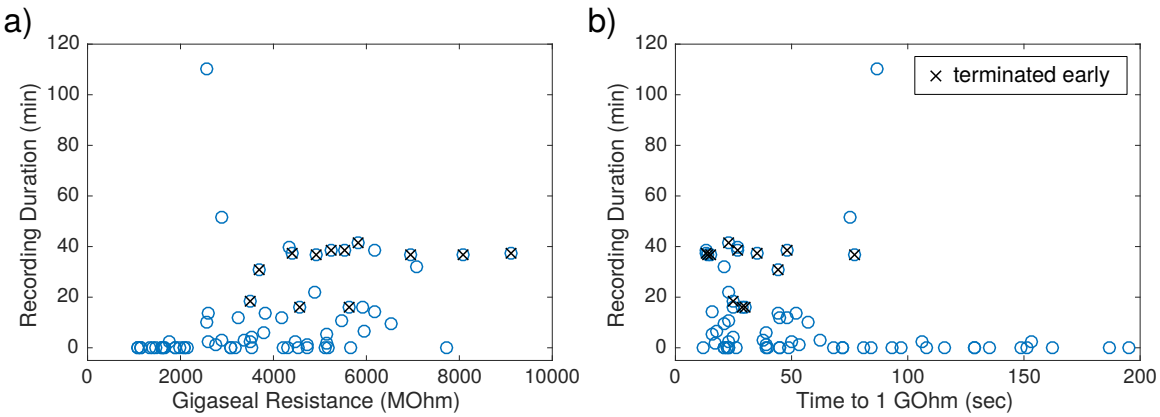

Figure 34: (a) Shows the effect of gigaseal resistance on recording duration. (b) Shows the lack of an effect from the rate of gigasealing on the recording duration for cells that form a seal within 100 seconds.

of recording stability whereas there is little correlation between the time to reach a gigaseal for gigaseals that form in less than 100 seconds. If the seal resistance is below 2 GΩ, the majority of the break-in attempts fail or the recording is unstable. Traditionally, a gigaseal that forms quickly is a good predictor of the stability of the recording as supported by the results in Figure 34b. For cells that seal in more than 100 seconds, very few were of good quality. This would indicate that the threshold values in Table 5 could be more strict to increase efficiency or that a new break-in method should be derived for cells with gigaseal resistances <2 GΩ. Alternatively, additional suction pressure applied during gigasealing (up to -200 mBar) [100] or moving the pipette closer to the cell could help increase the seal resistance, increase the yield, and improve the access resistance of the recordings.

4.2.3 Feedback-Controlled Break-in

This algorithm combines the computer-controlled analog pressure regulation system from Section 3.10 with high-speed resistance measurements to perform a ramp break-in method similar to the manual method described in [100]. Pulses of suction were used in the original autopatcher with good success (82%), and by other groups (66%) [28], but there remains the possibility of damaging the cell from using a pulse of

excessive duration or of excessive amplitude. Here we use a slow ramp of suction (0 to -345 mBar over 1.5 seconds) while monitoring the pipette resistance using a 100 Hz, 20 mV peak-to-peak amplitude square wave. The acquisition buffer was the size of one period of the square wave and the resistance was computed for each period and checked. During the ramp of suction, if the resistance dropped below 350 MΩ , the pressure was released by sending a serial command to the pressure control system to switch the solenoid valve to atmospheric. The voltage ramp sent to the electronic regulator to ramp down the suction pressure was controlled by a timer on a microcontroller within the pressure control system that could be interrupted by the command. This gave an average response time of 30 ms when using a model cell and up to 100 ms *in vivo* where noise could affect the resistance measurement. If the membrane failed to rupture after completing the ramp, a second ramp was initiated several seconds later and a zap (1V, 25-100 µs) was delivered 750 ms into the ramp. This combination was always able to either achieve a successful recording or resulted in the loss of the cell. Alternatively, a regulator capable of supplying a higher vacuum pressure could be used to continue the pressure ramp until break-in occurs.

We obtained an overall break-in success rate of 68% which, although somewhat lower that the original autopatcher (83%), is within the normal performance variation found between laboratories and experimenters (Fisher's Exact Test, p=0.4) [28]. As shown in Figure 34, the majority of recordings were of short duration or failed on break-in when the seal was less than 2 GΩ. Perhaps suction pulses or a voltage zap without suction are better for breaking into cells with seals <2 GΩ. The largest improvement due to this algorithm was a reduction in the average access resistance of the recording from 50 MΩ to 21 MΩ. These improvement is discussed further in Section 5.4.1.

Due to the latency limitations of the USB connections between the DAQ and

microcontroller to the computer, the response time is limited to 20-30 ms (not including the acquisition or processing time) and is subject to the additional sporadic latency from the Windows operating system. To improve the performance, a PCI DAQ interface (<10 µs) and a hardware serial port (<1 ms) could be used. Alternatively, a dedicated field-programmable gate array (FPGA) or an embedded real-time operating system could reduce the processing and data transmission overhead. After implementing these digital improvements, the response time would only be limited by the period of the square wave (10 ms) and the response time of the solenoid valve (4 ms). The potential benefits from additional reductions in the response time, such as further reducing access resistance, repeatability, and allowing more direct control of the pressure state, are offset by the additional complexity of lower latency hardware and software. The actual pressure change is also still subject to the pressure dynamics of the pressure control system (τ_{atm} = 73 ms), but a higher flow rate regulator or a vacuum tank could reduce this significantly.

4.2.4 Electrophysiology Algorithms

This section contains details on the methods used in the remaining algorithms required to fully automate the experiment.

4.2.4.1 Resting Membrane Potential

The resting membrane potential is easily measured in current clamp in the anesthetized and *in vitro* preparations due to the low variance in the resting voltage during a "down" state. After break-in, the robot checks the quality of the cell by performing a membrane test in voltage clamp and then switches to current clamp and continuously measures the resting voltage. It continuously interrogates the voltage data using a 0.5 second moving average over the acquired data. The variance of the 0.5 second period is also calculated and the first period acquired with a variance below 0.2 mV^2 is averaged and used as the resting membrane potential. These parameters

effectively select for quiescent periods because the variance is much higher during periods with spikes or subthreshold activity. This measurement is used on-line to check the quality of the recording following break-in.

4.2.4.2 Membrane Test

The membrane test is performed in voltage clamp by injecting a square wave of voltage (20 mV peak-to-peak, 25 Hz, DC offset at -65 mV) and calculating the access resistance, membrane resistance, membrane capacitance, membrane time constant, and holding current using charge integration methods [104] given the pipette resistance. The exponential fit and parameter calculations are performed on-line to enable the robot to check the quality of the recording and decide whether to terminate a poor recording or continue. The membrane test was performed several times throughout the experiment to assess the quality and drift of the recordings. The robot also sends a command to the visual stimulus computer to pause the visual stimulus (TCP socket connection, pauses the python script) and perform the test. This allows periodic quality monitoring which could also be coupled with future algorithms that could take corrective action (e.g., retract pipette 10 µm, apply slight positive pressure) to improve the quality of the recording [30]. Using a voltage clamp membrane test does increase the risk of damaging the cell from frequent switching between current clamp and voltage clamp, but this occurred in less than 10% of recordings.

4.2.4.3 Action Potential Detection

After the membrane test is performed and the resting potential is measured and both are found to meet the quality thresholds, the algorithm will inject a series of current pulses (600 ms) increasing in 20 pA steps while measuring the voltage response. If the recording contains a spike during the injection, the algorithm will detect them by searching for voltages greater than -10 mV. If found, the robot will continue to the next stage of the experiment. If the cell is lost or a glial cell is found, the current pulse

amplitudes will increase until the average voltage during the injection is greater than -20 mV whereupon the robot has determined that it was unable to elicit spikes and will retract the pipette. Note that if any spontaneous spikes occur during a current injection, this will also cause the algorithm to decide that the cell does indeed spike and will continue with the experiment.

4.2.4.4 Measure Rheobase

After the cell has passed the quality control checks (access resistance, membrane potential, spiking) and after a three-minute waiting period, the robot injects another set of increasing current pulses while monitoring for spikes to measure the rheobase. If spikes are found, that same current is injected an additional two times to confirm that the current is able to consistently elicit spikes. This approach accurately measured the rheobase, to within 20 pA, in all our recordings except for a fast spiking interneuron which had such a high level of spontaneous spiking activity that spikes occurred in during most current injections despite being far below the rheobase. In this cell it severely underestimated the rheobase.

4.2.4.5 Current Injections

After measuring the rheobase, the robot injects an appropriate range of currents to measure the IV relationship, evoked spike rates, sag currents, and adaptation properties of the cell. It injects from -0.5x to 1.5x the rheobase divided into 20 steps. The 20 current injections are repeated three times to control for *in vivo* variation and spontaneous activity; more repeats may be necessary for highly active cells. Some reports use up to two times the rheobase [147], which we found to be excessive and degraded the quality of recording in some cells. These current injections were 600 ms in duration. We found that one second durations led to slow depolarization of the cell and damage to the seal.

4.2.4.6 Capacitive Compensation

To increase the accuracy of the measured voltage, capacitive compensation is built into the amplifier to correct for the capacitance and series resistance of the pipette [150]. We integrated the robot with the amplifier control software (3rd party DLL interface) to use the automated capacitive compensation and estimation routines within the amplifier software. These calculate an approximate pipette capacitance that the robot then uses during current clamp. However, if the estimated capacitance is too high it can destroy the cell in current clamp mode so only 80-90% of the capacitance value was used by the robot. This was a reliable and moderately accurate method. The capacitance value is determined after the gigaseal has formed and before breaking in. After break-in has occurred, the robot performs a membrane test followed by a switch to current clamp whereupon it sets the capacitance compensation value in the amplifier software. This type of automated adjustment is only available on computer-controlled amplifiers (e.g., Multiclamp 700B, EPC10)

Software controlled amplifier adjustment is a recent development, with the first computer-controlled amplifier published in 1995 [132, 131] and now heavily used *in vitro* by automated patch systems [76]. It has not been used extensively *in vivo* due to the small number of possible simultaneous recordings. It is, however, a critical feature for this to be a fully automated.

4.2.4.7 Bridge Balance

The automated amplifier used here (Multiclamp 700B) also incorporates an automated bridge balance adjustment feature in its software, but was non-functional when using their DLL interface. However, the bridge balance value was adjustable in software so we integrated an automated bridge balance algorithm similar to the one described by Sherman-Gold [130], although ours is less aggressive (500 pA injection versus 5 nA). Using a 150 Hz square wave 500 pA peak-to-peak in current clamp

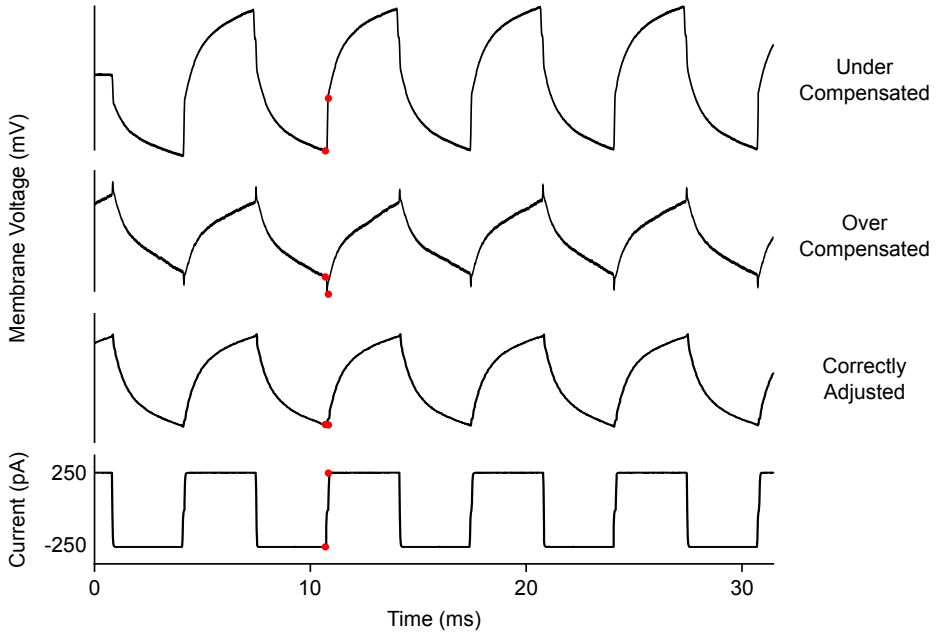

Figure 35: Plot showing the effects of over and undercompensating for the bridge balance. The red dots denote the samples that are compared during the on-line bridge balance adjustment to measure the degree of additional adjustment needed. The driving square wave is 150 Hz, 500 pA peak-to-peak, and the red dots are 150 µs to either side of the square wave transition.

mode, the bridge balance compensation is adjusted until the offset between the periods of positive and negative current injection are zero as shown in Figure 35. This is easily measured by comparing two samples 250 µs on either side of the transition point in the square wave (red dots) and adjusting the balance they are within 5 mV.

4.2.4.8 Return to Neuron Hunt

In the original autopatcher algorithm, there exists an option in the gigasealing stage to return to neuron hunt if the resistance decreases after detecting a cell. When gigasealing begins, there is a 10-second waiting period before the low positive pressure is released and if the resistance drops indicating that the cell has moved away from the pipette, the algorithm will return to neuron hunting. This threshold for this to happen was specified as a drop of more than 250 kΩ which proved problematic in cases where the resistance increase during neuron hunting is between 500 kΩ and

1 MΩ. These large increases are typically ideal, indicating that the membrane will be pressed up tightly against the tip of the pipette once the pressure is released and that the gigaseal will form quickly. However, the resistance will often drop 250 kΩ during the 10-second wait and the algorithm will return to neuron hunting and force the pipette further into the cell. The resistance drop in these cases is a small percentage of the resistance increase (25 - 50%) and the resistance is still far above the detection threshold so it should not indicate to the robot to return to neuron hunting. By changing the criteria so that the robot returns to neuron hunting only if the resistance drops below the detection threshold (we use 350 kΩ) rather than an absolute resistance drop, the algorithm could correctly handle detection events >500 kΩ. This algorithm has been proven in the fully-automated system and with the traditional autopatching hardware.

4.2.4.9 Data Logging

The added benefit of fully-automated experimentation is the ability to automatically log all the operational and experimental parameters measured in the experiment. The cell quality statistics, rheobase, current injections properties, and action potential properties are all recorded during operation and could be used to control the response of the robot. This would allow different experimental protocols to be conducted based on the type of cell detector quality of the recording, maximizing the usefulness of each recording obtained. This on-line data also enables the robot to adapt the same way a manual operator would.

CHAPTER 5

IN VIVO ROBOT VALIDATION

5.1 Introduction

The validation of a new tool is a critical piece of the development process. In the metrology sciences, when certifying a new length measurement tool, it is compared against ultra-precise length standards that have themselves been calibrated against the international standards for length. Historically, these standards have taken the form of platinum bars of exact length (from 1889 to 1960), the wavelength of atomic emissions (from 1960 to 1983), and ultimately the speed of light itself (from 1983 to the present) [142]. While the science of *in vivo* electrophysiology has yet to reach this level of precision and global standardization, it is with this perspective that we undertake the validation of these new automation tools.

In a system of this complexity, it is difficult to foresee which are the most important design parameters, interactions, and performance metrics. Continuous *in vivo* testing throughout development effectively highlighted the most critical issues and allowed direct comparison with the performance of the original autopatcher and manual methods. The algorithms, for example, underwent a series of revisions based on how they performed *in vivo*, similar to the iterative testing procedure used to develop the original autopatcher algorithms.

One of the major challenges with *in vivo* testing, however, is the inherent variability in the quality of surgical preparation, the geometry of the pipettes, and contamination that can falsely implicate the hardware or algorithm being tested as the source of failure. This can lead to unnecessary redesign efforts. A better approach is to conduct multiple experiments to control for day-to-day variation, especially when the

performance difference is small or when a small number of data points are obtained from each experiment. However, this significantly increases the number of experiments required and limits the number of improvements that can be made. This is one of the main challenges that has limited the progress of the patch clamp technique over the last few decades. Technique improvements have been made, especially when driven by a scientific objective, such as developing the original *in vivo* patch clamp technique [100, 25], combining two photon imaging to target specific cells [74], developing a pipette fixation method for freely moving recordings [79], or developing the original automated patch clamp technique [69], but these typically require extensive optimization and validation.

The fully-automated robot was also developed over several periods of extensive *in vivo* experimentation. There were three main sets of experiments designed to test the robot in various stages of development. Our first set of experiments was designed to validate the wire threading, pipette tip positioning accuracy, pressure control, and amplifier tuning capability of the integrated robot design (Figure 5). We simultaneously validated the new state-machine software architecture that incorporated the original autopatcher algorithm (see Figure 33b) [70]. This led to the discovery of some of the critical design challenges (pipette insertion into holder, silver wire buckling, low reliability, etc.) and resulted in several semi-automated recordings *in vivo*. These first experiments demonstrated that automation would indeed be possible once all the subsystems were integrated.

After implementing the necessary improvements, the next set of validation experiments focused on using the robot to characterize the types of cells in the primary visual cortex (V1) in anesthetized mice. This more complex experiment placed higher demands on the robot by requiring 20 - 40 min recordings and higher throughput. It also required additional automation and software features to control the flow of the

experiment as well as a number of electrophysiological tasks: switching the amplifier between current and voltage clamp, tuning the recording parameters, performing current injections, assessing cell quality, displaying visual stimulation, and terminating the recording. However, the 33 automated recordings obtained by the robot still lacked the stability and resolution necessary for *in vivo* cell-type characterization. The average recording duration was only 4.1 min. After exhaustively eliminating all the possible effects from sub-optimal experimental preparation over the course of 25 *in vivo* experiments, we concluded that the persistent poor performance was due to flaws in the architectural strategy of the integrated robot design. This phase of experimentation also included testing the automated pipette holder prototypes of the final robot design (Figure 7) that utilizes the entirely new architecture. It showed an immediate performance improvement during the final eight additional experiments, yielding an average recording time of 13.7 minutes (for recordings that were at least 4 min in duration). It also yielded four recordings with sufficient duration to perform a full characterization of the visual response indicating that the robot is capable of obtaining stable, high-quality recordings. This was the critical milestone that showed that an automated system could achieve high quality recordings and eventually perform the entire electrophysiological experiment which to this point was still an entirely manual process. This set of 33 experiments and 674 patch clamp trials was performed in Seattle at the Allen Institute for Brain Science with their generous support. Several recordings where biocytin reconstructions were attempted showed significant background staining or lack of visible biocytin. We therefore focused our efforts on the electorphysiological data collection. We estimate that $> 50\%$ of pipettes that were retracted at 3 µm/s to form the gigaseal reached > 600 MΩ, necessary for quality reconstructions. With further improvements in the biocytin concentration, recording duration, and post processing steps, the robot could potentially be used for coupled electrophysiological and morphological characterization. For best results,

multiple craniotomies should be used to leverage the autonomous ability of the robot to best effect. If only one craniotomy and very few pipette insertions are desired, manual experimentation may be more efficient.

The goal of the final set of experiments was to demonstrate both full automation and high quality recordings, which to this point had been only partially demonstrated in the two previous sets of experiments. Once the hardware was complete for the new architecture (Chapter 3), and the software architecture and algorithms were developed to automate the electrophysiological portions of the experiment (Chapter 4), we demonstrated the quality and full autonomy of the robot by performing an additional 21 *in vivo* experiments. These yielded 39 recordings with 16 of sufficient duration for visual response characterization. A total of 699 patch clamp trials were performed by the robot. The robot now routinely acquires 1 - 3 high-quality long-duration recordings per experiment and in two separate instances obtained two whole-cell recordings in sequence, completely without any human interaction. The robot still benefits from occasional human intervention to adjust the target position in the craniotomy after several pipette insertions, to check for bleeding, and to refresh the artificial cerebral spinal fluid (ACSF) on the surface of the brain. However, the labor-intensive tedious process of replacing pipettes and manipulating long electrophysiological recordings, has now been reduced to a simple supervisory task that requires minimal training and requires little attention. This design is ready for parallelization and enables high-throughput *in vivo* whole-cell patch clamp recordings.

These final 39 recordings were obtained in the primary visual cortex (V1) of mice with the goal of investigating the role of layer 5 (L5) cells and their unique intrinsic properties. The following sections will discuss the physiology of L5, our experimental methods, the quality of the recordings obtained by the robot, and conclude by comparing the intrinsic and functional properties from our recordings with current literature.

5.2 Cell Types and Electrophysiology of Layer 5

L5 in the visual cortex has garnered significant interest due to its role as an output layer from the cortex to many other functional areas including projections to subcortical areas [65, 145, 11, 45, 49, 55, 56, 63, 154] and higher visual areas [65, 95]. L5 pyramidal neurons in V1 are thought to modulate subcortical regions in response to motion in the visual field and also transmit information to secondary visual areas. Most studies have analyzed the intrinsic and functional role of these cells using patch clamp recordings *in vitro* [77, 44] or used two-photon microscopy *in vivo* [65, 95, 51]. However, very few studies have used patch clamp recordings *in vivo* in V1 L5 with visual stimulus. The *in vitro* studies have shown intrinsic bursting and back propagating action potential (bAP) physiology similar to those observed in L5 of the vibrissae pathway in rats [78, 120, 51] and mice [58]. Patch clamp recordings have also been used extensively in V1 layer 4 of mice to characterize the cells that receive the majority of the sensory input from the thalamus [84, 85, 86]. Recent work in layer 6 also employed large-scale *in vivo* patch clamp recordings (80 recordings, 16 morphological reconstructions) to show the intracellular and morphologically correlated cell-type specific behavior. We deployed the robot in L5 to both validate the robot and support the ongoing efforts to characterize the functional cell types in V1.

Previous studies have shown at least three main types of visually active pyramidal cells in L5 [65, 95]. These types are usually characterized by the targets of their axonal projections including cortico-cortical (CC), cortico-subcortical (CS), and cortico-cortical/non-striatal (CC-NS). The classification schemes are constantly being revised and complemented by additional simultaneous measurements on additional measurement axes (e.g., transcriptomal, morphological, physiological). This is typical in general within every major cell-type classification scheme throughout the brain [43] and we can expect these to be refined further as new information becomes available. The three types in L5 are also defined by the morphology of the dendritic arbor; CC

cells have a thin apical dendrite and small apical dendritic tuft; CS cells typically have thick apical dendrites and an extensive tuft arborization; CC-NS cells have similar arborizations to CC cells.

These cell types are also classified by their intrinsic electrophysiological properties. Three of the most prominent features of CS cells in L5 are 1) a large dendritic calcium current that occurs at the main bifurcation point in the apical tuft, 2) back propagating action potentials, and 3) intrinsic bursting behavior [78, 20, 51]. Interestingly, although the bursting and the calcium currents are highly correlated, they seem to be driven by two separate mechanisms when they occur in the hippocampus [33]. Bursts are thought to be involved in coincidence detection [129] and can often induce dendritic calcium currents which may play an important role in plasticity by effecting long term changes in the dendritic arbor and postsynaptic cells [75]. Bursts are also more informationally rich, possibly to enable more reliable signal transmission in certain brain areas [89]. Bursting is also thought to be a second "state," possibly enabling multiple signal processing modes within the same cell [112].

Back propagating action potentials occur when high frequency action potentials occur in the soma and cause a depolarization of the dendritic arbor. This back propagation is Na^+ channel mediated and causes an increase in dendritic Ca^{2+} currents, further increasing the sensitivity of the apical tuft. For somatic action potentials occurring at >100 Hz (critical frequency), the back propagating signal can cause a large depolarizing Ca^{2+} current which can lead to bursting [129, 77]. This effect has been extensively studied *in vitro* [77], extracellularly [17], and intracellularly using sharps electrodes [61] and is thought to play a role in plasticity by affecting various Ca^{2+} mediated pathways [51, 62]. This mechanism forms a method for reverse information transfer between the somatic compartment and the tuft [136, 149]. These Ca^{2+} currents have been linked to sensory input in the vibrissae pathway and place-cell firing in the hippocampus [51, 93, 33]. However, the functional role of these large calcium

currents, bursts, and bAPs have yet to be determined in V1 L5.

In the recent work using two photon imaging, genetically encoded calcium indicators, and transgenic and viral morphological reconstruction methods, they identified the visual spatial frequency tuning, orientation tuning, and bandwidth for each cell type in L5 and correlated their function with their long range connectivity. They effectively characterized the spiking behavior and output characteristics on a large scale (∼1500 cells) [65, 95]. There still exists a major gap, however, in identifying the function role of the unique intrinsic behaviors of L5 cells. Their existence and potential role has been explored *in vitro* but a functional link is still unknown. Currently, patch clamp recordings are the only available method for obtaining the long duration intracellular recordings needed to correlate these effects with sensory stimuli. Calcium indicators lack the temporal and subthreshold resolution necessary to record these behaviors *in vivo*.

While a full characterization of functional L5 physiology is beyond the scope of this work, we will discuss a preliminary analysis of bursting, bAPs, and the general cell types (bursting and regular spiking) observed by the fully-automated robot during our *in vivo* validation.

5.3 Methods

We performed *in vivo* patch clamp recordings in 8 - 14 week old C57BL/6 mice (Charles River Laboratories International Inc.). For the patch clamp recordings, the stock intracellular solution contains 135 mM potassium gluconate, 10 mM HEPES, 4 mM potassium chloride, and 1 mM EGTA dissolved in deionized H20 with the pH adjusted to 7.30 using 1 µL additions of 8 N KOH being careful to wipe down the exterior of the pipette tip for more accurate additions. This stock solution is first prepared in a 50 mL batch, aliquoted into 4 mL volumes in 5 mL cryogenic vials (Globe Scientific Inc., 3015), and stored at -50° C. 8 mL of stock solution are thawed

as needed and 0.3 mM GTP-Na, 5 mM ATP-Mg, and 10 mM Na_2-phosphocreatine are added. The pH is then readjusted using 8 N KOH to 7.25 and aliquoted into 32, 0.5 mL centrifuge tubes (Eppendorf 022363611) (250 µL in each), stored at -50° C, and used within 6 months. This is based on a protocol developed by Yang Dan's laboratory. The complete protocol with minor edits is included in Appendix A.

5.3.1 Surgical Preparation

The surgical preparation consists of implanting a titanium headplate on the skull of the mouse to increase the stability of the recordings. First, anesthesia is induced using 5% isoflurane in 100% oxygen followed by 1.1 - 1.5% for maintenance during surgery. The skull of the animal is positioned in a stereotax (Kopf 963, 923-B, 922) using non-rupture ear bars. Ophthalmic ointment (Puralube) is applied to the eyes to prevent the formation of cataracts. Meloxicam (0.2 - 1.0 mg/kg), atropine (0.05 mg/kg), and buprenorphine (0.05 - 0.1 mg/kg) are administered after induction. Meloxicam and buprenorphine help reduce brain swelling and variability between animals by reducing inflammation and reducing the sympathetic response. Optionally, dexamethasone (3.2 mg/kg) can administered ideally between 8 and 12 hours prior to surgery (can be given a minimum of 2 hours before) to help reduce brain swelling. Atropine helps reduce airway secretions and reduces gasping, especially during long experiments (>1 hr under anesthesia).

Once the animal is positioned in the stereotax, a mid-line incision is made along the scalp using a #10 scalpel and a small portion of the skin is removed to expose the top of the skull (approximately 8-10 mm in diameter). The residual fascia and periostium should be removed to allow good adhesion between the dental cement and the skull. The muscle connections on the lateral and posterior edges are detached and retracted 1 mm using a #11 scalpel. The muscle is affixed using surgical adhesive (e.g., Vetbond) to expose the corner transition between the top and sides of the skull.

Figure 36: (a) Dimensioned drawing and (b) photograph of the headplate that is surgically implanted on the skull of the mouse. The Y shaped tabs are held in clamps to provide mechanical stability during the experiment. (c) Illustrates the locations where the dental cement should be applied (white fillets). Lambda and bregma are also labeled inside the 11.5 mm opening in the headplate (L and B). The headplate design and surgical technique were developed by the Allen Institute for Brain Science.

The skull is then leveled with respect to lambda and bregma using the stereotax, and the titanium head post (see Figure 36a-b) is placed on the surface of the skull. The inner apical edge of the 11.5 mm diameter opening in the headplate should be positioned approximately 1.25 mm anterior to bregma and centered laterally. Dental cement (Metabond Parkell, S371, S398, S396, S387) is applied on the underside and vertical edges of the headplate around the periphery of the opening and around the entire perimeter near the skull (see Figure 36c). This surgical technique was developed by the Allen Institute for Brain Science.

Two craniotomies were made at 1.25 mm anterior and 2.25 mm lateral to lambda in both hemispheres. A high-speed dental drill (American Rotary Tools Company, ECO450, 1/8" collet), with a 250 µm diameter square end mill, is attached to a 3-axis manipulator to allow precise control of the drilling location and depth. After locating the end mill above the desired location on the skull, the manipulator lowers the drill 190 µm from the surface of the skull to drill a precise craniotomy. This technique is based on the automated craniotomy robot but operates without using the electrical feedback [114]. Vascularization in the skull above the visual cortex often results in false positive detections of the brain surface, prematurely stopping the drill. After the initial drilling using the manipulator, a dental drill (3/32" collet) with a spherical

dental bur (diameter 250 µm, #1/4 size) is used to manually countersink the area around the drilling location. The tip of a 29 gauge needle (ExcelInt 26018) is then used to lift the bone island remaining in the drilling location. If not completely detached, additional manual countersinking around the periphery and mechanical separation using the needle can separate the island. Extreme care should be taken to avoid damaging the surface of the brain when removing the bone. The opening in the skull should be as small as possible (200-350 µm) while exposing sufficient tissue to allow pipette insertion without damaging blood vessels or contacting the dura. The dura is retracted by delicately rubbing the dura using the tip of fine (not ultra-fine) tweezers that are sufficiently rounded to avoid damaging the cortex. Alternatively, the tip of a 29 gauge needle that has been bent so that the tip points parallel to the surface of the cortex can be used to cut a slit in the dura and fold it to either side of the slit. Some groups leave the dura intact to avoid damaging the cortex but we have found that this increases the rate of clogged pipettes [28].

Throughout the surgical procedure, the surface of the brain and dura should be kept moist by submersing it in ACSF or 0.9% saline once the bone is removed. While the dura is being manipulated however, it is most easily visualized and removed after the fluid has been wicked away. Care should be taken to periodically hydrate the surface of the brain during this procedure if it begins to dry (every 1-2 min). Bleeding can be controlled by irrigating with ACSF or 0.9% saline and utilizing absorbent spears (Kettenbach, Sugi). With careful manipulation of the dura, bleeding can occasionally be avoided altogether. Clotting on the surface of the brain should be avoided as it increases the incidence of clogged pipettes even after the clots are removed. Throughout the remainder of the experiment, the surface of the brain should be covered by ACSF or 0.9% saline except when positioning the tip of the pipette above the surface of the brain. If pipette clogging is problematic, several cycles of irrigation and drying will help remove debris from the area surrounding the

craniotomy. Filtering the ACSF or 0.9% saline can also reduce clogging. The entire surgical procedure requires 45 - 90 min. Additional information on our surgical and experimental methods are detailed in [70].

5.3.2 Recording Protocol

After surgery, the animal is relocated to the electrophysiological apparatus where the headplate is secured horizontally using aluminum optical filter clamps (Eskma Optics, 830-0055) and 12 mm optical posts. Isoflurane (0.75 - 1.1%) in 100% oxygen is continued throughout the experiment. The level of anesthesia was carefully regulated as to just suppress the toe pinch reflex. Any additional anesthesia will unnecessarily suppress additional cortical activity. The temperature of the animal was maintained at 37° C using a low-noise warming pad (FHC, DC temperature controller FHC-40908, small heating pad FHC-4090207). If the animal is too cold, the breathing will slow and gasping will be more evident. Motion of the spinal cord during gasping causes severe motion artifacts and will effectively prevent gigaseal formation if not addressed. The posture of the mouse should be adjusted to reduce this motion by positioning the head of the mouse approximately 22 mm above the warming pad [34]. The breathing rate should be at least 0.5 Hz.

The ophthalmic ointment is removed from the eyes before beginning the recordings and hyaluronan eye drops and contact lenses (Ocuscience, 2.5 mm) help maintain optical clarity and to reduce the formation of cataracts. To enable recording from either hemisphere, two 609 mm monitors were placed in front of the animal at a 55° angle measured from a vertically oriented plane intersecting the midline of the animal, and 190 mm from the eye at the closest point. The lower edge of the monitors were placed 100 mm below eye level so as to cover 74° of visual space in altitude, and 98° in azimuth. Drifting sinusoidal gratings with spatial frequencies 0.01, 0.02, 0.04, and 0.08 were displayed with a fixed 2 Hz temporal frequency. Eight different grating

orientations were displayed with a contrast ratio of 0.8. The PsychoPy software suite was used to generate and display the stimulus with slight modifications for dual monitor display. The visual stimulus was displayed on the monitor contralateral to the hemisphere of the recording while the other monitor was kept blank. A photodiode (ThorLabs, PDA25K) was placed in front of one monitor to directly record the onset of the stimulus in parallel the recording. Each combination of spatial frequency and orientation was displayed eight times, in a randomized fashion. Ten seconds of blank stimulus (gray screen) preceded the first stimulus presentation and followed the final presentation. Each stimulus was presented for two seconds, followed by a blank stimulus displayed for one second. For every 10 visual stimulus presentations, a two-second blank stimulus was also presented. These blank stimuli were also included in the randomization scheme.

We utilized a Multiclamp 700B intracellular amplifier, Digidata 1440 for data acquisition, and pClamp 10 software for processing (Molecular Devices LLC). The liquid junction potential between the pipette and the bath was corrected before neuron hunting. The bridge balance was corrected using the algorithm in Chapter 4. The pipette capacitance was compensated in current clamp using 80-90% of the automated compensation value determined by the amplifier just prior to break in. The recordings were post processed using MATLAB (MathWorks Inc.).

5.3.3 Pipette Geometry

One of the most critical aspects of high-yield *in vivo* patch clamp recordings is the geometry of the pipette tip. We pulled pipettes using 1.5 x 0.86 mm filamented borosilicate capillaries with fire polished ends (Warner G150-4) using a flaming brown pipette puller (Sutter Instruments, Inc. P-97) with a 3 x 3 mm platinum box filament. The puller was adjusted to have the settings in Table 6. The pipettes had an average resistance of 6.5 MΩ (σ = 1.1 MΩ) and ranged from 3.9 - 9 MΩ. We optimized the

Table 6: Pipette puller settings used for 1.5 mm OD x 0.86 mm ID borosilicate capillaries on a P-97 flaming brown puller. A 3 mm x 3 mm platinum box filament was used.

Heat	Velocity	Pull	Delay	Pressure	# Lines	# Loops
648 (Ramp + 20)	22	0	0	600	1	5

pipettes to have a wide cone angle at the tip. Figure 37 illustrates the geometrical features of an optimal pipette and denotes how the cone angle is measured (Figure 37c). Pipettes with a concave taper (Figure 37b, right), are thought to be more likely to seal poorly and aspirate the cell into the pipette during gigasealing whereas a convex taper (Figure 37b, left) is thought to increase the gigaseal resistance, improve the probability of a successful break in, and prevent aspiration of the cell. Some groups include fire polishing or other procedures to maximize the smoothness of the tip and this cone angle [105, 148, 42].

The two right images of Figure 37a and the one in Figure 37c were acquired using a 100x water immersion objective on an upright bright-field microscope (Compound Microscopes CD005A000M) which reduces the aberrations seen in the images acquired at 40x in the two left images in Figure 37a. This is critical for determining the real shape of the pipette tip rather than inferring the geometry from the optical aberrations at the tip of the pipette as is traditionally done by most experimenters. Terms such as "nubs" or "bulbs" are traditionally used to describe these aberrations by experienced electrophysiologists to indicate good or bad tip geometry. This manual inspection technique is highly subjective, making it difficult for new experimenters to optimize pipette geometry and achieve high yield, especially *in vivo* where the experiment is much more sensitive than *in vitro*.

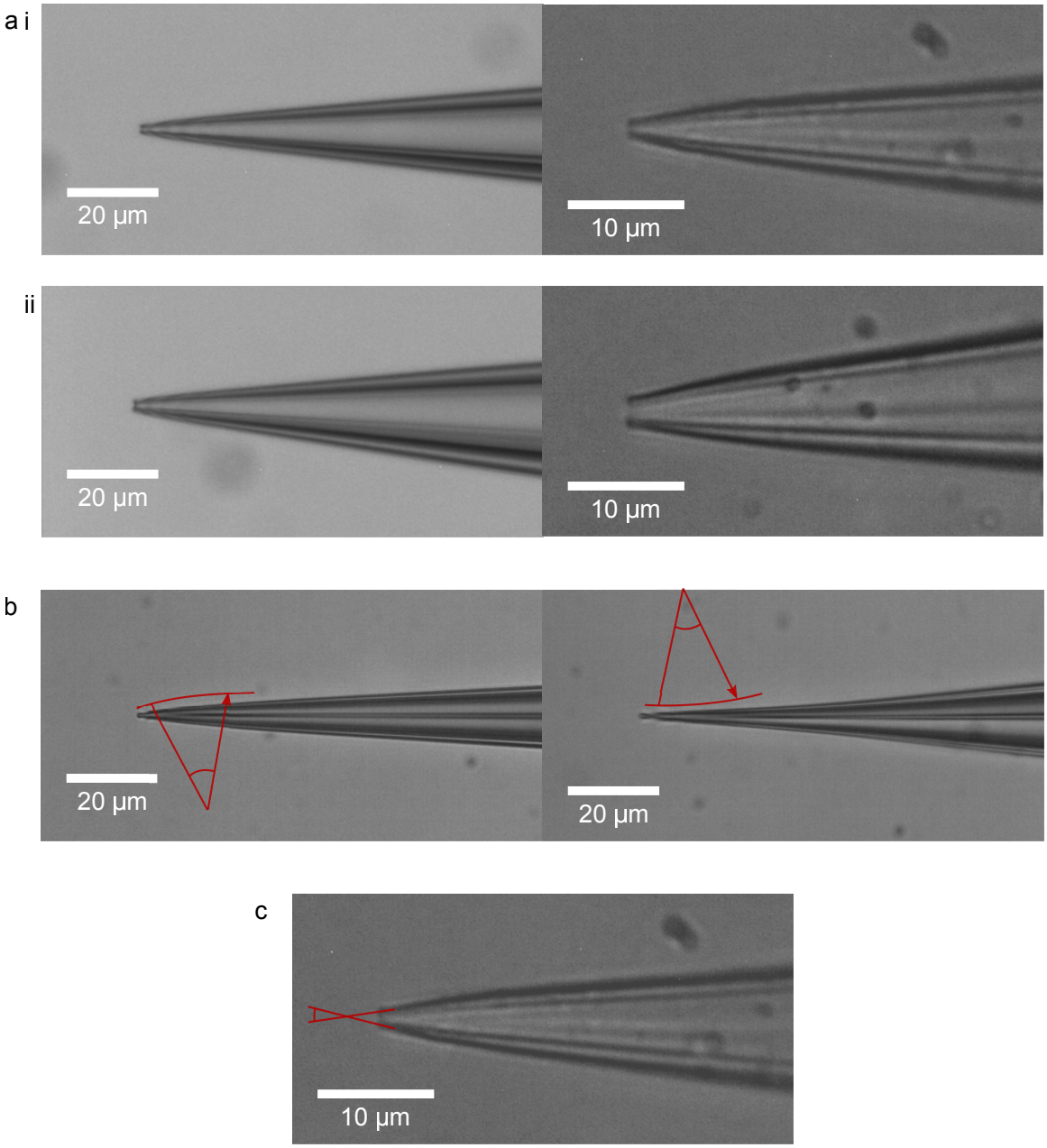

Figure 37: Photomicrographs of patch pipettes, focusing on the pipette tip. (ai) Ideal patch pipette with 0.9 µm tip diameter (6.2 MΩ resistance) visualized at 40x magnification objective (left) and 100X water immersion objective (right) in comparison to (aii) a patch pipette with 1.5 µm tip diameter (3.3 MΩ resistance) visualized at 40x magnification objective (left) and 100x water immersion objective (right). (b) Comparison of a concave tapered pipette which is ideal for *in vivo* recordings (left) vs. convex tapered pipettes (right) which result in lower yield (20x objective). (c) A wide cone angle, measured at the very tip of the pipette (red, 21.5°), is ideal for high-yield experiments and leads to rapid gigasealing, stable recordings, and requires fewer break-in attempts and less suction pressure when using the pulse method.

An automated pipette inspection microscope to rapidly and quantitatively measure the diameter and cone angle of the pipette tip is detailed in Section 3.11. We found that the optimal pipette geometry has a diameter between 0.9 and 1.1 µm and a tip angle >15°. The pipette in Figure 37c has a diameter of 1.5 µm and a cone angle of 21.5°.

We also compared several different batches of borosilicate capillaries from different manufacturers and found that it affects the ability of the puller to create the convex taper at the tip of the pipette. We were advised by Sutter Instruments Inc. that this is likely due to differences in the composition of the glass, leading to different glass transition temperatures and the size of the glass transition temperature range. This property likely interacts with the heating and cooling stages of pulling where glass that solidifies more quickly during the cooling stage might more easily produce that convex shape. After the filament is aligned and the optimal puller settings are found, changing the composition of the glass is the next step towards achieving optimal pipette geometry. Increasing the pressure setting on the P-97 also enhances the cooling which will produce a more convex taper.

As previously discussed in Section 3.5, the diameters of the glass capillaries also vary enough (±2.5%) to affect the diameter and shape of the pipette tip. It can affect the alignment of the capillary in the filament and change the total thermal capacitance enough to change the pulling dynamics. We found it was beneficial to measure and sort the capillaries by their outer diameters to achieve the most consistent size, shape, and resistance (bin size of 0.02 mm). This also helps prevent erroneous conclusions when optimizing the puller settings.

In a separate set of experiments performed in collaboration with Yi Liew, we found that two populations of pipettes with similar average resistances (μ_1 = 5.4 MΩ, μ_2 = 6.8 MΩ) had different whole-cell recording yields (Y_1 = 8.8% n_1 = 34 trials, Y_2 = 23% n_2 = 52 trials) although not statistically different (Fisher's Exact test p=0.145).

The pipettes were pulled using the same batch of borosilicate glass, using different puller settings. All other experimental variables were held constant. Group 1 had a concave taper and very parallel walls at the tip, whereas group 2 had a convex taper and a wider cone angle similar to Figure 37ai. This suggests that a wider cone angle is important for high-yield experiments *in vivo* and that the resistance alone is not sufficient.

With the fully-automated robot, there was not statistical difference overall between the resistance of the pipettes from the entire population and those that achieved successful recordings, 6.5 MΩ (σ = 1.1 MΩ) and 6.3 MΩ (σ = 1.2 MΩ) respectively (Student's T-test $p>0.05$). The pipettes that achieved whole-cell recordings had resistances between 3.9 and 9.0 MΩ, similar to previous reports. We also observed no significant effect from the pipette resistance on the recording duration (ANOVA F-test $p=0.18$).

5.4 Results

These results are the output from the final 21 experiments performed by the robot yielding 39 whole-cell recordings. Data from the prior experiments were omitted so the experimental parameters, surgical technique, and pipette geometry would be as consistent as possible. The data show that the robot can autonomously obtain stable, high-quality whole-cell recordings from multiple cell types.

5.4.1 Recording Quality

We previously defined a threshold for quality recordings as ones with a resting membrane below -55 mV, series resistance below 50 MΩ, action potential peak voltages greater than 0 mV, and holding currents at -65 mV of less than ±200 pA. These are the typical quality thresholds used for *in vivo* patch clamp recordings [69, 30, 39, 84, 66, 100]. For characterizing the visual response, only recordings that

were of sufficient duration to include a minimum of three repeats of the visual stimulus for all orientations were included (except for cell 16, a putative interneuron, which only had 1 - 3 repeats).

Figure 38 shows the duration of the recordings, resting membrane potential, series resistance, membrane resistance, holding current to maintain the cell at -65 mV, and the spike amplitude, for all 39 cells recorded by the fully-automated robot. There were 41% of the recordings (16/39) that were a least 14 minutes in duration, sufficient for measuring the intrinsic parameters and for a partial visual stimulation characterization. There were 31% (12/39) with both the intrinsic parameters and the all eight replicates of visual stimulation. And finally 23% (9/39) of the recordings were of sufficient quality and duration to obtain more than eight replicates of the visual stimulus. The average recording duration was 19.8 minutes, and ranged from 1 110 minutes. It requires approximately five minutes at the beginning of the recording to wait for it to stabilize and to measure the intrinsic parameters by injecting current and conducting membrane tests in voltage clamp. The visual stimulus then follows and requires 15 minutes to display the eight replicates of orientation and spatial frequency. A few recordings (12/39, 31%) were terminated early once the 8 - 16 repeats of the visual stimulus were complete, so the true average maximum recording duration is likely higher.

The bi-modal shape of the recording durations in Figure 38 suggests that a subset of recordings are inherently more stable and durations >30 min can be expected. This improvement occurred after the pipette geometry was optimized (see Section 5.3.3) and the surgical technique improved for making 200 - 300 µm diameter craniotomies. The stability of the recording is a function of the craniotomy size, with smaller craniotomies showing reduced tissue motion and longer recording durations [100, 28]. After these changes, the final six experiments had an average duration of 35 min (for recordings longer than 4 min) and 90% of those were terminated early

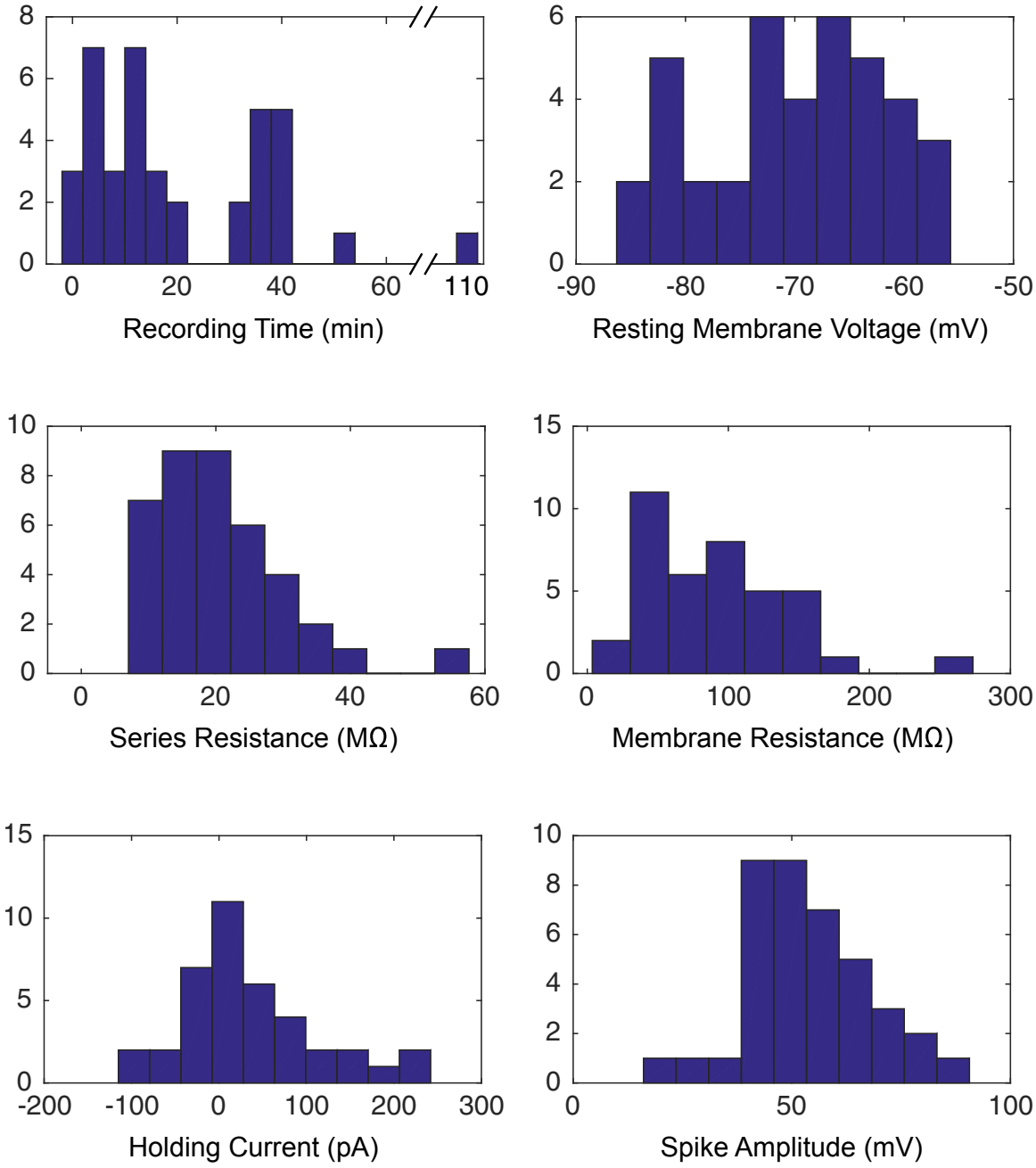

Figure 38: Histograms of common quality metrics for the final recordings acquired by the robot. A total of 39 recordings were obtained in 21 experiments. The holding current is the amount of current required to hold the cell at -65 mV. The spike amplitude is measured as the spike peak voltage minus the spike threshold.

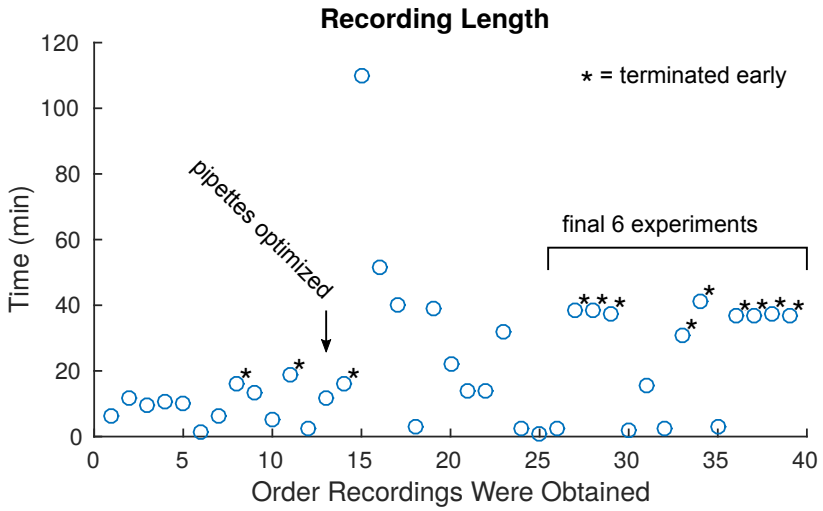

Figure 39: Plot showing increasing recording durations over time as the pipette geometry was improved and surgical technique was optimized. The cells recorded during the final six experiments had significantly longer recording times and are more consistent with other reports of average recording duration. The recordings with an asterisk were terminated once the visual stimulation was completed.

after completing 16 repeats of the full visual stimulation protocol (see Figure 39).

This performance compares well with other reports for recording durations *in vivo* (20 min [30], 8 - 30 min in awake mice [100, 28], 10 - 150 min in awake bats [25]) and with the original autopatcher (56.6 $\pm$44.2 min in anesthetized mice [69], $\sim$45 min in anesthetized mice [70]).

Series resistance, combined with the capacitance of the pipette, has a filtering effect on the recorded voltage, reducing resolution. The amplifiers can compensate for a portion of the pipette capacitance and series resistance but this can cause instability and large voltage oscillations that can destroy the cell. It is advantageous therefore, to reduce this resistance as much as possible experimentally by keeping the tip of the pipette clear of debris. *In vitro*, the pipettes and experimental conditions can be optimized to achieve <15 MΩ of series resistance [126] but due to the difficulty in obtaining *in vivo* recordings, a larger resistance is tolerated. The original autopatcher had an average series resistance of 50 MΩ with a wide standard deviation (18.9 MΩ) similar to another group that also using an automated patch clamp system (52

MΩ) [28]. These are similar to those seen in most manual *in vivo* recordings [100, 30, 71]. Using the pressure control system developed here and the same algorithms as the original autopatcher, the average series resistance was reduced to 27.9 MΩ (σ = 10.2 MΩ) showing a statistically significant improvement in the mean (two-tailed Student's T-test, $p<0.05$) and variance (F-Test, $p<0.05$) as shown in Figure 40 "control box." This demonstrates the performance and repeatability benefits from using electronic pressure regulation in place of syringes or mouth pipetting. The figure also shows additional improvement using the feedback-controlled ramp break-in algorithm discussed in Section 4.2.3 that further reduced the average series resistance to 21.6 MΩ (two-tailed Student's T-test, $p<0.05$) and exhibited a similar variance (σ= 10.2 MΩ, F-test, $p>0.05$). This represents a significant improvement over the series resistance typically seen in manual *in vivo* experiments and approaches the levels seen in *in vitro* and during two-photon targeted experiments [67]. We also obtained very low series resistance recordings in a 14-week-old animal where we obtained three recordings with an average series resistance of 17.7 MΩ, significantly lower than those reported in the literature for animals of this age ($\sim$100 MΩ) [100].

The average resting membrane potential was -70.1 mV which was lower than that of the original autopatcher (-61.2 mV, Student's T-test, $p<0.05$) largely due to the 4 - 6.3 mV difference in the Goldman-Hodgkin-Katz potential calculated from the composition of the internal solution, -63.5 mV and -57.2 mV for the solutions used in the robot and the autopatcher respectively. This effect also affects the holding current required to maintain the cell at -65 mV in current clamp. The robot had an average 38.7 pA holding current compared to the -8 mV pA in the autopatcher. Overall, values are similar to those seen during manual experiments [69, 100].

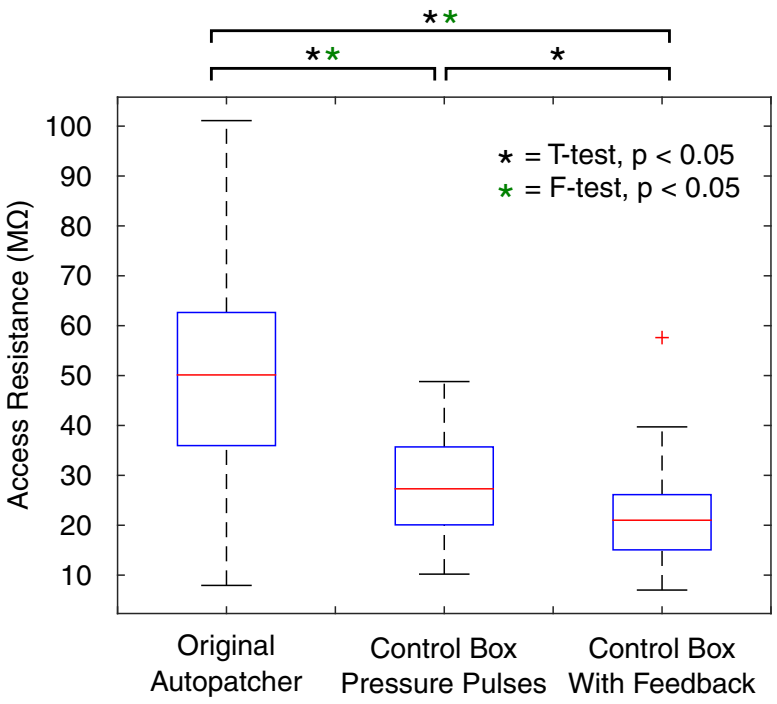

Figure 40: The addition of the electronic pressure control system (Control Box) significantly reduced the average series resistance compared to the original autopatcher and reduced variation. The feedback-controlled pressure-ramp break-in algorithm showed additional improvement. (n=25 for the original autopatcher, n=21 for the control box using pressure pulses, and n=42 for the control box with the feedback break-in method).

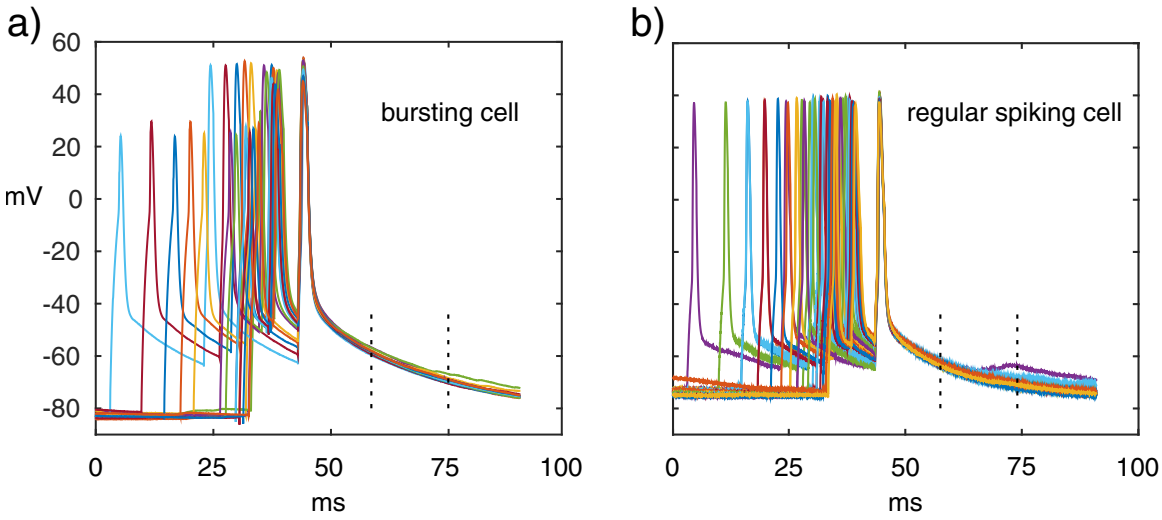

Figure 41: Plots showing evoked spiking behavior while injecting three 1.8 ms current pulses with frequencies ranging between 25 - 100 Hz with an amplitude between 800 - 1000 pA. (a) Shows the response for a bursting neuron, and (b) shows the same for a regular spiking neuron. We did not observe any afterdepolarization following the third spike in any of the cells (n=7) which would have been confirmation of a bAP and dendritic calcium current. The dashed lines delineate the expected region for these depolarizations.

5.4.2 Back-Propagating Action Potentials and Bursting

Back-propagating action potentials were originally characterized *in vitro* through simultaneous patch clamp recordings in the soma, apical dendrite, and basal dendrites [77, 120, 129, 109] with one instance of two photon guided dendritic recordings *in vivo*. Due to the challenge of dendritic patch recordings and simultaneous recordings *in vivo*, the functional correlate of this bAPs is still unknown.

Figure 41 shows our results from current pulse injections (25 - 100 Hz) designed to induce bAPs. For both bursting (n=4) and non-bursting cells (n=1) we saw no evidence of the characteristic after depolarizations (ADP) as seen by others in vitro [77, 129, 120] for current pulses with frequencies beyond 100 Hz. They do report instances where dendritic spikes produce no visible ADP at the soma [77] similar to our observation. This could indicate that the *in vivo* extracellular environment or spontaneous inhibitory network activity may suppress this effect.

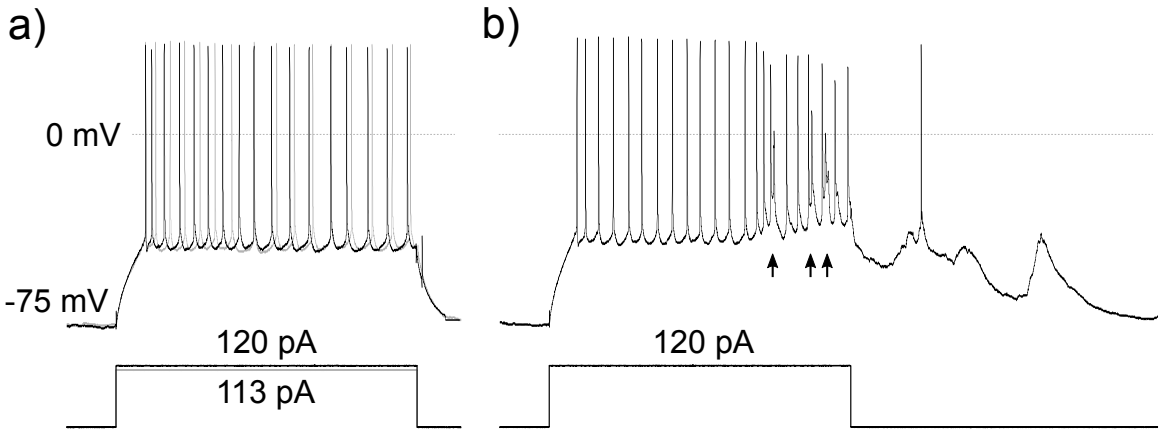

Figure 42: (a) Plot showing the failure of current injections to reliably evoke bursts at 1.5x the rheobase. (b) Bursting that occurred during current injections was likely due to concurrent spontaneous activity. Arrows denote doublet bursts. Rheobase was 80 pA.

In addition, we were unable to reliably evoke bursting using somatic current injections in spontaneously bursting cells for moderate amplitude current injections (1.5x rheobase, Figure 42a), different from reports in L5 of the rat barrel cortex [51] where somatic current injections elicited bursts and dendritic calcium spikes. Bursts did occur during current injections but seemed to require the addition of ongoing spontaneous activity (Figure 42b).

Overall, we observed somwhat sparse bursting activity similar to observations in L5 of the somatosensory cortex where ¡ 15% of APs were part of a burst [75]. In one cell with more frequent bursting activity, we observed very specific direction tuning aligned with the preferred spiking orientation, with a moderately broad orientation tuning curve. It had very little spontaneous bursting activity indicating a higher signal-to-noise ratio than individual spikes, similar to observations in freely viewing monkeys [90]. This suggests that bursting is a critical visual processing feature of V1 L5 neurons and likely requiring large data sets and long duration recordings to adequately correlate sensory stimulus with intracellular activity.

5.4.3 Visual Response

In our analysis of the visual response, we found that 87.5% of the cells in our data exhibited a statistically significant spiking response to visual stimuli. We compared the number of spikes per one-second interval of visual stimulus to the number of spikes during the one-second blank periods between stimuli. The results were approximately Poisson distributed with some non-ideal dispersion where $\mu < \sigma^2$ (ideally $\mu = \sigma^2$ for a true Poisson distribution) and from some zero inflation (i.e., results dominated by many one-second periods with zero spikes). A goodness of fit test using the χ^2 distribution to test the appropriateness of the Poisson distribution was unsuccessful due to the low number of counts per bin, even with bin pooling. The Poisson rate ratio exact test was used here despite some dispersion and zero inflation due to its improved accuracy over the more traditional Wilcoxon-Mann-Whitney test[102]. Alternative to the ratio exact test, more advanced methods such as the negative binomial distribution could more effectively account for dispersion and zero inflation. Table 7 shows the spike counts, the number of one-second intervals, the p-values using the rate ratio exact test, the calculated rate ratio (λ_v/λ_b) assuming a perfect Poisson distribution, and a rate ratio calculated from a Poisson regression.

We confirmed the test by dividing the periods of blank stimuli from a single recording into two groups and the test did not show significance between them. The number of spikes during the visual stimulus is a sum from all the responses to all orientations and spatial frequencies.

In addition to spiking, we integrated the subthreshold activity during the periods of stimulus and during blanking and 56.3% (n=9/16) of cells had statistically significant responses (Student's T-test, $p<0.05$). This reduced rate is due to the up and down states that occur during anesthetized recordings. The spikes were removed from the recording before performing the integration.

We also characterized the strength of visual drive by integrating the subthreshold

Table 7: Data used to test the statistical significance of the spiking behavior. Periods of visual stimulation are compared to periods of blank stimuli using a Poisson rate ratio exact test with a null hypothesis that the spike rates are equal between the two groups. (* = limit of machine precision)

				VStim		Blank		VStim	Blank	
Cell ID #	p-value	Ideal Rate ratio	Regression Rate Ratio	# Spikes	# Intervals	# Spikes	# Intervals	Spikes/sec	Spikes/sec	% Increase
12	1	1.09	0.63533	8	251	8	275	0.032	0.029	9.6%
14	2.20E-16*	2.7	1.5211	592	192	236	207	3.083	1.140	170%
16	0.5	1.78	1.4254	5	57	3	61	0.088	0.049	78.4%
20	2.20E-16*	2.88	1.7066	306	157	115	170	1.949	0.676	188%
22	2.20E-16*	1.69	1.0074	3839	974	2477	1064	3.941	2.328	69.3%
23	2.20E-16*	1.922	2.7841	5025	508	1153	556	9.892	2.074	377%
24	2.20E-16*	11.9	8.0397	142	508	13	556	0.280	0.023	1096%
26	2.20E-16*	3.17	1.8678	2480	509	853	556	4.872	1.534	218%
35	2.73E-09	1.48	0.84935	539	416	406	463	1.296	0.877	47.8%
36	2.20E-16*	1.8	1.0419	1129	513	678	555	2.201	1.222	80.2%
40	2.20E-16*	2.39	1.3468	1388	326	623	349	4.258	1.785	139%
41	2.20E-16*	5.45	3.4473	479	256	96	280	1.871	0.343	446%
43	2.20E-16*	1.759	0.99905	1221	499	751	540	2.447	1.391	75.9%
44	2.20E-16*	3.49	2.1429	2081	466	657	513	4.466	1.281	249%
45	2.20E-16*	3.67	2.0156	69896	530	20140	560	131.879	35.964	267%
46	2.20E-16*	2.55	1.6026	503	503	220	560	1.000	0.393	155%

activity during the first 500 ms after the onset of the stimulus and compared it to the integration of the 500 ms of activity prior to onset. Both this integral and the integration over the entire stimulus window were calculated relative to a baseline voltage equal to the minimum voltage measurement that occurred during the integration period. Using this onset integration metric, there were 93.8% (15/16) of cells with significant subthreshold responses to visual stimuli (Student's T-test, $p<0.05$).

For comparison, the proportion of visually responsive cells of certain subpopulations in previous studies using two photon calcium imaging was approximately 50% for awake mice and 84% for animals under 0.2 - 0.75% isoflurane (Tlx3-Cre$^+$, Efr3a-Cre$^+$, Glt25d2-Cre$^+$ [65], and CT, CC, CS projection neurons [95]). Our recordings were obtained under 0.75 - 1.1% isoflurane. The metrics used to determine visually driven cells using two photon imaging (6% - 10% $\Delta F/F$) and patch clamp recordings (Poisson exact test) are not directly comparable considering the different levels of anesthesia and the challenges with indirect measurement of spiking activity using genetically encoded calcium indicators. With regards to the proportion of visually active cells, the largest sources of error stem from the variation in the proportion of visually active cells depending on the type of indicator used (10-60% [22, 64]). Calcium indicators have yet to be fully validated to determine if they represent the true proportions of population spiking behavior. They do, however, provide large sample sizes for measuring spike orientation, direction, and spatial frequency tuning (1000s of cells).

Figures 43, 44, and 45 show the spiking response from current injections and visual stimulus for regular spiking (RS) cells (n=5), intrinsically bursting cells (IB) (n=9), and for the two putative interneurons recorded by the robot (Cells 16 and 45). The cell IDs in the figure correspond to those in Table 7. Appendix B shows the orientation tuning plots for the subthreshold integration metrics and spatial frequency tuning. While in this case we have divided the data into four groups (regular spiking,

bursting, SOM interneuron, PV^+ interneuron), based on their electrophysiological properties, there are clearly multiple cell types within each group. CC, Efr3a-Cre^+, and Tlx3-Cre^+ are typically regular spiking; CS, CT, and Glt25d2-Cre^+ are intrinsically bursting. To link the axonal morphology with the intracellular properties of these cells, simultaneous patch recordings and morphological reconstructions using blind methods with single cell transfection [122] or two photon targeted methods with transgenic or viral targeting [74, 67, 147] would be required.

Negative values exist in the tuning plots when the response falls below the baseline firing rate (green circles). The variation in the tuning plots is the result of the high background activity and the up and down states under anesthesia. Light anesthesia (0.75 - 1.1% isoflurane) led to higher spontaneous firing rates combined with up and down states. In one cell, only six spikes were present during the two-second period of visual stimulus and was immediately followed by a bursting up state that produced 46 spikes during the one-second blank period. This significantly skews the average background firing rate which leads to negative values in the orientation plots. The average spontaneous firing rate of the IB cells was 1.4 $\pm$0.18 Hz compared to 0.46 $\pm$0.29 Hz for RS cells (mean $\pm$ standard error of the mean) and were statistically different (Student's T-test, $p<0.05$). This agrees with previous reports in L5 cells in the auditory cortex showing that IB cells had a higher spontaneous firing rate than RS neurons, 3.3 Hz and 1.28 Hz respectively in an anesthetized preparation using ketamine and xylazine [139]. Similarly, in L5 of the vibrissae pathway under urethane, the thick tufted cells had spontaneous rates of 3.65 Hz and 1.1 Hz for slender tufted [26]. These morphologies correlate well with IB and RS cells respectively [65, 95].

Figure 46 shows the orientation selectivity indices (OSI) and direction selectivity indices (DSI) of the visual spiking response for IB and RS cells excluding the putative interneurons. Negative DSIs and OSIs and values greater than one are a result of the variation and negative values in the tuning curves. The variation within and between

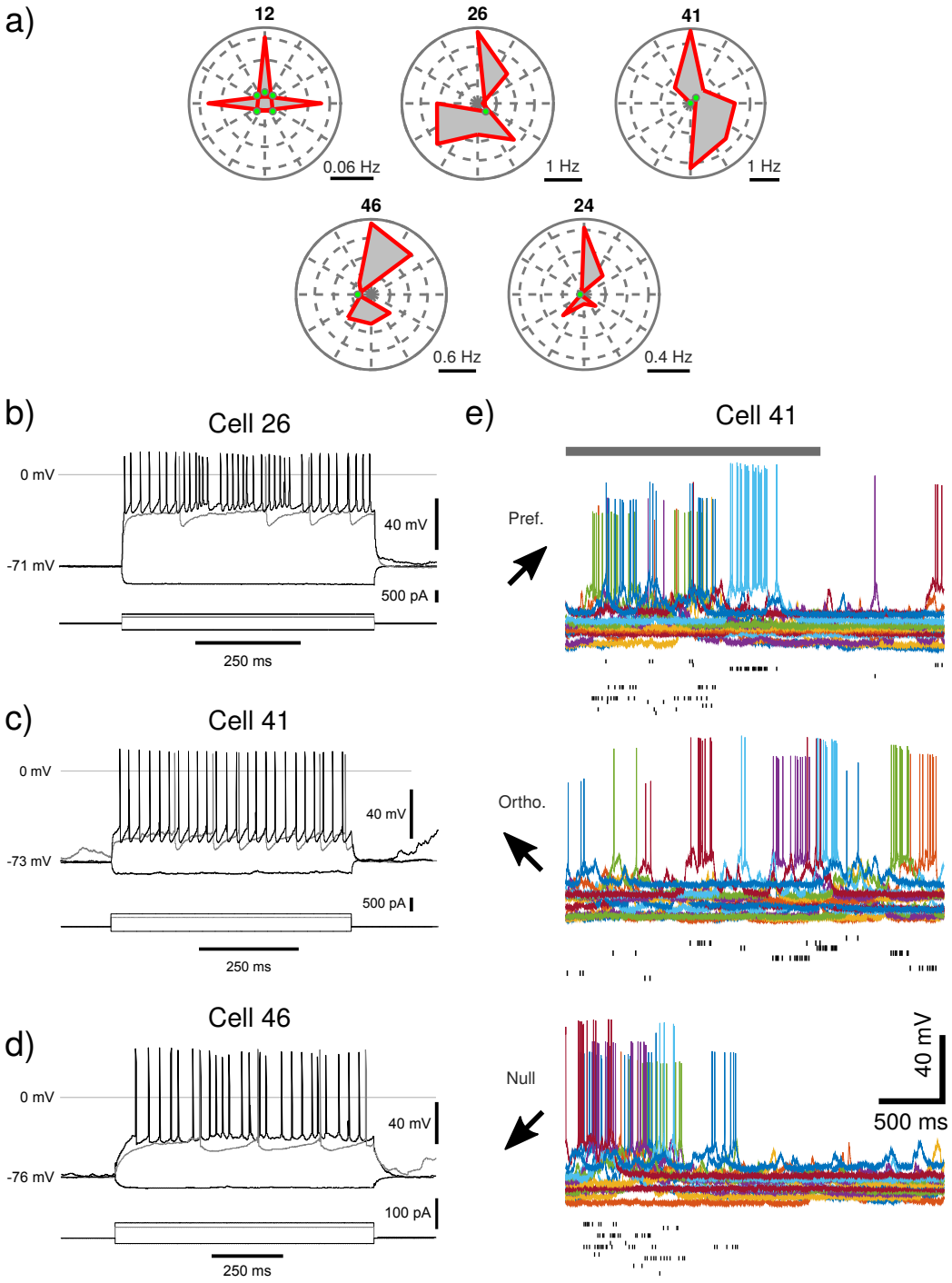

Figure 43: Characteristics of regular spiking neurons. (a) Orientation tuning plots for spiking. All the tuning plots have been rotated so the preferred direction is oriented up. The green dots denote orientations with a response that falls below the baseline activity (negative). (b-d) Current injections for individual cells. (e) Membrane voltages during visual stimulus (gray bar).

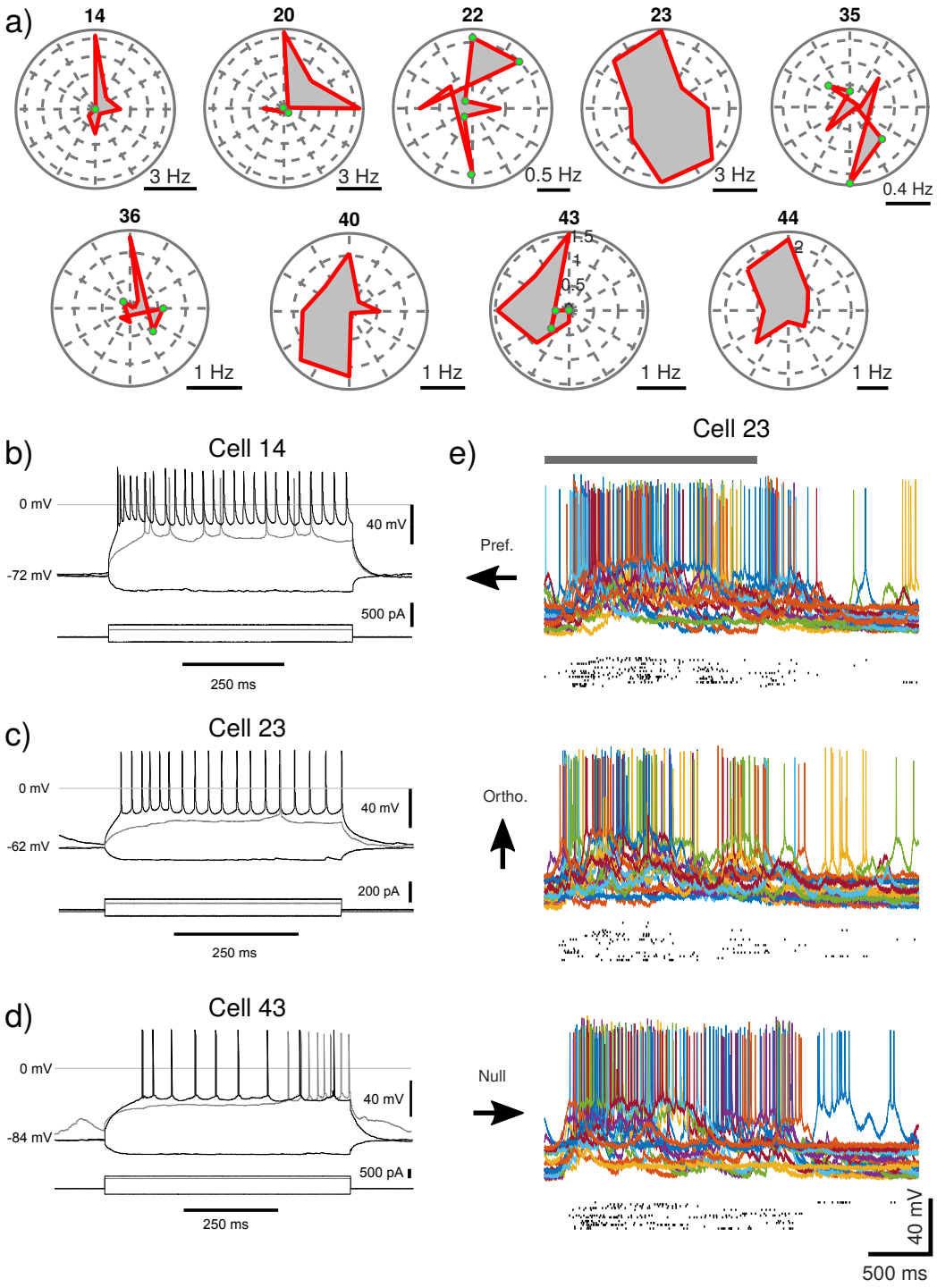

Figure 44: Characteristics of bursting neurons. (a) Orientation tuning plots for spiking. All the tuning plots have been rotated so the preferred direction is oriented up. The green dots denote orientations with a response that falls below the baseline activity (negative). (b-d) Current injections for individual cells. (e) Membrane voltages during visual stimulus (gray bar).

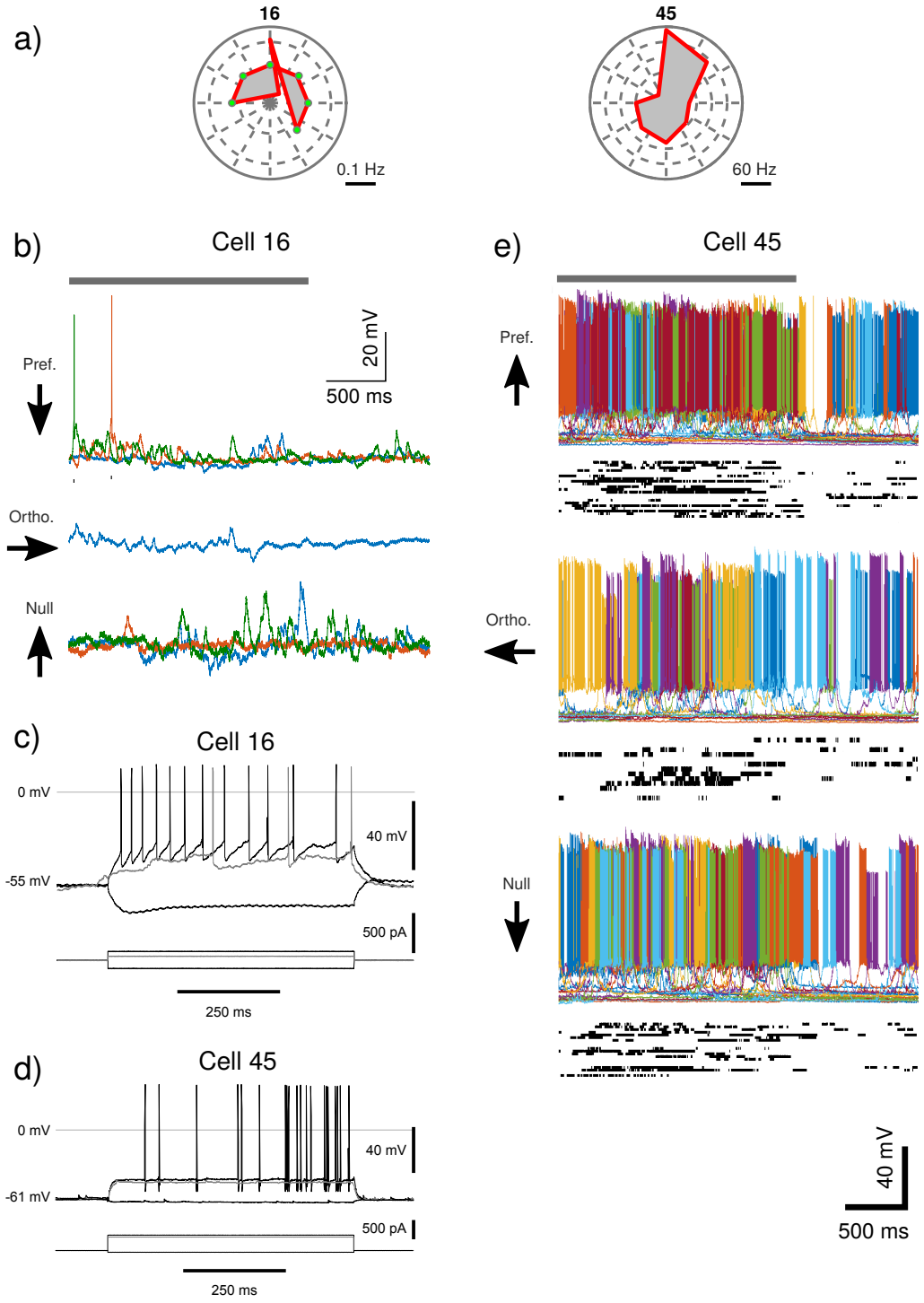

Figure 45: Two interneuron recordings. (a) Orientation tuning plots for spiking. The tuning plots have been rotated so the preferred direction is oriented up. The green dots denote orientations with a response that falls below the baseline activity (negative). (b and e) Membrane voltages during visual stimulus (gray bar). (c and d) Current injections for individual cells. Cell 16 is a putative SOM+ interneuron characterized by a strong h-current and low spontaneous firing rate. Cell 45 is likely a PV+ interneuron judging by its high maximum firing rate (∼400 Hz).

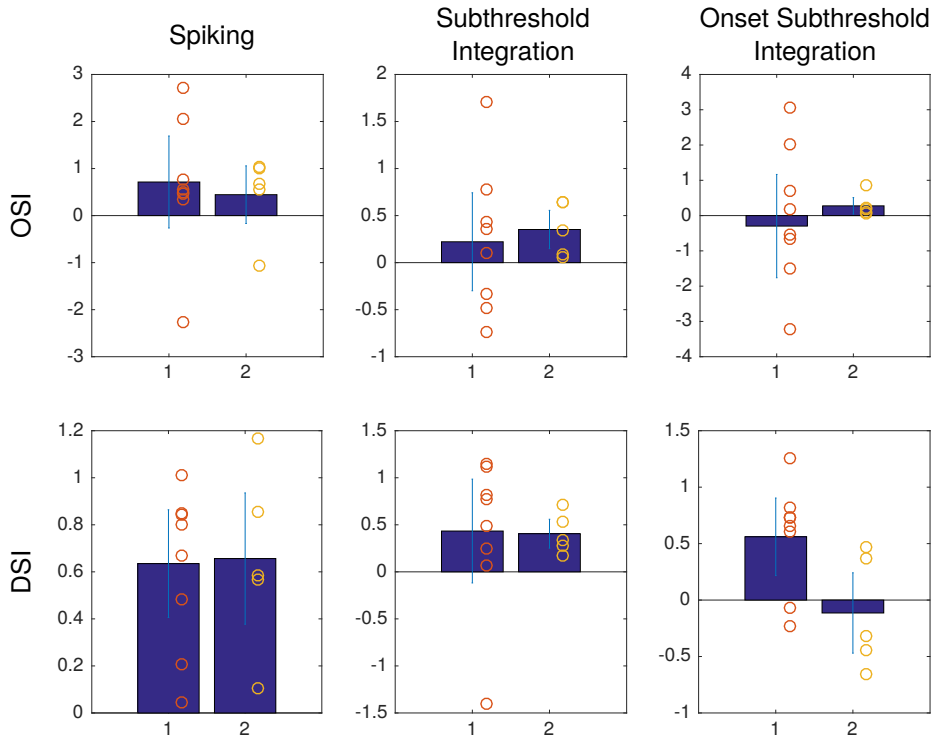

Figure 46: Orientation and direction selectivity indices for bursting (1), and non-bursting (2) cells for spiking, subthreshold integration, or subthreshold integration during the initial 500 ms of stimulus onset.

the two groups is much larger than reported by studies using two photon imaging [65, 95], but is similar to the variation seen in patch recordings in L6 [147] although they had a much lower spontaneous firing rate. Patch clamp recordings are limited in the number of replicates of the visual stimulus it can display during the 30-minute recording whereas many replicates are possible with two photon imaging. They also improve consistency by targeting an identified subpopulation of cells and select for ones with a strong visual response whereas these data show the heterogeneity in L5 cells using a broader sampling method. A subset of the IB cells (7/21) exhibited bursts with subsequent voltage plateaus at -10 to -15 mV (see Figure 47, similar to those observed in the hippocampus [36, 141, 93] and cerebellum [91]). In the hippocampus, they are elicited by place fields in a robust manner during freely moving recordings. The functional role of bursting in V1 L5 remains unknown. To the author's knowledge, this is the first evidence for voltage plateaus in mouse V1 L5. This highlights the

need for additional intracellular recordings to correlate bursting and plateaus with sensory input or behavior. In L5 of the rat primary somatosensory cortex, 15% of spikes form part of a burst, making them somewhat rare. For such a potent signal, this certainly seems appropriate especially considering the added effects of plasticity within the apical tuft due to bAPs and potentiation of downstream targets [27]. In our recordings, bursts were similarly infrequent preventing correlation with the visual stimulus. The patch clamp technique is currently the only method for observing these behaviors and to determine their functional role *in vivo*. However, due to the high spontaneous firing rate and low bursting frequency, it will require a large number of recordings to obtain sufficient statistical power. Due to possible effect of bursting on plasticity, the preferred stimulus may also be better elucidated during awake recordings while presenting novel visual stimuli. These challenges highlight the need for high-throughput automated recording methods.

Of the 16 recordings, two were likely interneurons judging by their intrinsic firing behavior. Approximately 30% of cells in L5 are interneurons [49] showing that there is a bias in the robot towards pyramidal cells (only 5%, 2/39, were interneurons). Figure 45a-c (cell 16) is possibly a somatostatin positive interneuron (SOM^+) exhibiting a strong h-current and rebound behavior [94, 97]. The intrinsic parameters of this cell also agree well with those identified by others [23, 152] such as a high resting membrane potential (-56 mV) and a low spontaneous firing rate (0.05 Hz) [96]. The spike adaptation behavior of this cell is also similar [97]. SOM^+ cells in L5 are often Martinolli cells [107] and may have similar role to those in the hippocampus where they regulate the bursting behavior of pyramidal cells [124, 41]. The axons of SOM^+ cells in layers 4 and 5 project densely to layer 1 [97] coincident with the apical tuft of L5 pyramidal cells which have been shown to be involved in L5 cell bursting behavior [145, 77]. There were too few replicates of the stimulus to establish the visual response of this cell.

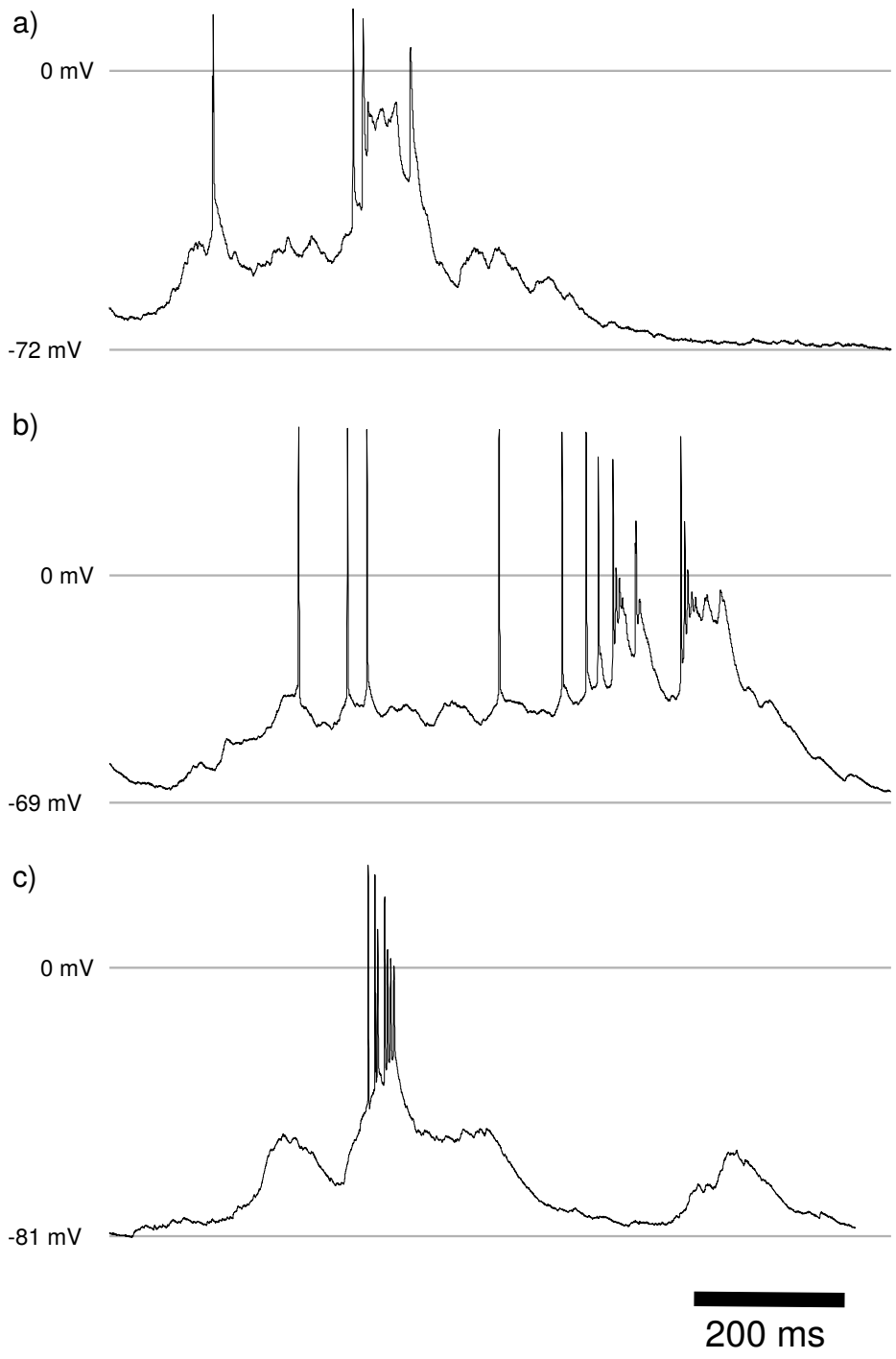

Figure 47: Plots of the different bursting modalities in L5 V1 pyramidal cells. (a-b) Show a -10 to -15 mV voltage plateau in a subset of bursts similar to those in the hippocampus and cerebellum. (c) A more typical bursting behavior for comparison. (a) Is from cell 14, (b) is from cell 23, and (c) is from cell 43.

Figure 45a,d-e (cell 45) is very likely a parvalbumin positive (PV^+) interneuron due to its high max firing rate (∼400 Hz) and large after spike hyperpolarization (AHP) [54, 125, 101]. The PV^+ cells are thought to linearly modulate activity in the visual cortex [6] and are highly visually responsive (79% of all PV^+ cells) with some orientation tuning [96]. The cell in Figure 45a demonstrated good orientation tuning and some direction selectivity consistent with previous reports.

5.5 Conclusions

We validated the robot by acquiring 39 high-quality recordings *in vivo* in a fully-automated and systematic manner representing the transformation from a highly skilled manual technique to a robust, robotic tool. The quality of the recordings is seen in the average recording duration (19.8 min), the low average series resistance (21 MΩ), and agreement with published physiological results. We now have a tool capable of high throughput *in vivo* cell-type characterization necessary for acquiring the sample sizes to correlate rare intracellular events with sensory stimuli. We also showed the large variation in L5 visual responses through a blind sampling of bursting and regular spiking cells, motivating the need for larger sample sizes afforded by automated systems. Finally, we observed the previously unreported presence of voltage plateaus in L5 IB cells similar to those found in other brain regions.

CHAPTER 6

CONCLUSIONS AND FUTURE WORK

The immense complexity of the brain presents significant instrumentation challenges as we seek to characterize basic function of individual cells, networks, and entire regions. Recent advancements in two-photon microscopy, genetically encoded calcium indicators, calcium dyes, voltage sensitive dyes, and electrode arrays enable thousands of cells to be recorded simultaneously. While these tools have dramatically accelerated our understanding of neural function on the network level they have limited resolution to record the single cell subthreshold activity critical to cellular level computation. Of the intracellular recording methods, patch clamp recordings are the only method with sufficient stability and resolution for correlating subthreshold events with *in vivo* function. Due to the difficulty of the experimental procedure *in vivo*, only single patch clamp recordings were possible until recently [68]. The highly skilled and manual nature of the experiment limits the throughput, introduces variability, and prevents large scale systematic studies of brain regions with this resolution.

This work addresses these issues by quantitatively characterizing the highly-skilled tasks and incorporating automation systems that increase the repeatability and autonomy of the experiment enabling parallelization and high-throughput cell-type characterization. This work represents the transformation of an experimental art form into systematic robotic tools. Previous work presented methods for performing the pipette quality checks, regional pipette localization, neuron hunting, and gigasealing steps of the experiment [69]. In parallel with this work, others have also developed methods for precise pipette positioning and pressure control [28]. This work integrates

the prior advancements with the remaining hardware, software, and algorithms necessary to perform, for the first time, fully-automated serial recordings *in vivo* without any human interaction. This effectively removes the human from the loop, reducing variability and training time, and increases recording quality.

Finally, the robot performed a preliminary survey of the visual response of different cell types in L5 of the mouse visual cortex demonstrating the ability to repeatably acquire high-quality, stable recordings. It also showed the need to link the unique intrinsic intracellular properties of L5 cells with sensory stimuli which is only possible with whole-cell patch clamp recordings. It also showed the inherent heterogeneity in L5 and the high spontaneous activity that will require large data sets, enabled by these robotic tools, to decipher the rich *in vivo* behaviors found within L5.

6.1 Major Contributions

The major contributions of this work include hardware advancements, algorithm developments, and physiological observations in L5.

- Demonstrated the first fully-automated serial patch clamp recordings *in vivo* without human intervention. In two experiments, three serial recordings were obtained in a completely autonomous fashion, and up to five serial recordings were obtained in a single experiment with only minor manual adjustments. It can perform 40 serial attempts at a time with 83.8% reliability in all the pipette preparation steps for small craniotomies (250-300 µm diameter), and achieved a 9.9% whole-cell recording yield.

- Designed, fabricated, characterized, and disseminated the automated pressure control system now in use by dozens of labs for automated patch clamp experiments. It provides the 800 mBar, 25 mBar, -15 mBar, and -345 mBar pressures, analog control, and the rapid ($\tau < 71$ ms), accurate, and repeatable pressure dynamics required for successful break-in [70].

- Designed, fabricated, and integrated hardware for automated pipette storage, pipette filling, pipette length measurement, automated pipette holding, wire threading, precise pipette positioning in the craniotomy, and pipette handling. Combined with the pressure control system and control software, these systems automate all of the remaining tasks in a patch clamp trial, removing the human from the loop. The system enables unattended operation and parallel scaling [40].

- Developed an adaptive algorithm to choose the moment for break-in for both fast and slow gigasealing cells using numerical derivatives of the resistance measurements during gigasealing and empirically optimized quantitative decision criteria that replicates the judgment of an experienced human operator seeking to maximize the gigaseal resistance without reducing experimental efficiency.

- Developed a feedback-controlled break-in algorithm and supporting hardware that detects the moment of break-in during a 1.5 second ramp of negative pressure (0 to -345 mBar) and releases pressure within 30 - 100 ms of detection. This led to a reduced average series resistance of 21.6 MΩ comparable to that typically seen in *in vitro* and in two-photon guided experiments *in vivo*.

- Validated the fully-automated system in L5 of mouse V1, where it obtained 39 whole-cell recordings, 16 of which included visual stimulation to characterize the functional intracellular properties of these cells. We report the presence of previously unreported voltage plateaus in bursting cells and corroborate reports of high spontaneous activity, varied visual responsiveness, and heterogeneous orientation tuning in both spiking and subthreshold responses to visual stimuli.

6.2 Future Work

6.2.1 Pipette Tip Positioning with Feedback

Due to the misalignment of the pipette tip relative to the walls of the capillary, kinematic constraints are insufficient for increasing the precision beyond the 30 - 60 µm error inherent in the manufacturing process shown here and elsewhere [28]. Therefore either a higher precision pipette puller must be devised or a high-precision measurement system is needed to track the true position of the pipette tip after insertion into the pipette holder. Laser-based optical micrometers (Keyence Co.), small-footprint microscopes (Dino-Lite), or a custom high-resolution optical interrupt system could be used to sense the position of the pipette tip. The major constraints are 1) footprint of the sensors in the space near the mouse, 2) electrical interference in the recordings, and 3) mechanical stability. Depending on the resolution of the sensors, the accuracy could be improved to within tens of micrometers which would further reduce clogging, improve reliability, and would be robust to manufacturing errors. Based on the performance improvements seen in this work from increasing pipette placement accuracy, this will likely continue to improve the yield of the system. This feedback would also be generally applicable to other tasks such as targeted viral injections for retrograde labeling or for more accurate extracellular electrode insertion, especially for smaller deeper structures.

6.2.2 Algorithms

With a fully-automated robot we can now systematically explore additional algorithms such as methods for reducing series resistance during a recording by performing slight positional adjustments or pressure manipulations to keep the pipette tip clear of debris. These are employed in manual experiments and would benefit from an optimized, repeatable robot that uses the series resistance as a feedback measurement to inform the adjustment methods [30]. This would increase the overall yield

by compensating for tissue drift in a semi-closed loop fashion.

6.2.3 Miniaturized Automated Patch Recordings

Intracellular recordings in freely moving animals remain an enormous challenge due to the size of the hardware used to actuate the pipette and amplify the signal. Tissue motion and low yield also severely limit the throughput and only a few groups have successfully obtained them [79, 80, 33]. Work is underway to miniaturize the amplifiers [48] and here we show a miniaturized actuation system and custom pipette holder that could be attached to the head of the animal (Figure 48). It uses piezoelectric squiggle motors for nanometer resolution motion and has a very small footprint (28 x 13.2 x 7.5 mm). The open loop version of this motor is only 1.8 x 1.8 x 6 mm. The system also replaces the conventional 1.5 mm diameter borosilicate pipettes with 350 µm diameter fused silica pipettes enabling head mounting and a higher packing density for multiple simultaneous recordings (Figure 48c) [73]. The system successfully obtained recordings *in vitro* (Figure 48h). We characterized the pipette positioning precision (see Figure 48d-g) and found that some improvements will be necessary to reduce random error, perhaps by adding a preload to the linear bearing. This design needs further weight and size reduction by using the open loop squiggle motor, shorter pipettes, and increased stiffness and precision in the linear bearing to stabilize the pipette during animal movement [52]. Future work is also required to reduce electrical noise from the motor and optimize the pipette tip geometry when fabricated from the fused silica capillaries. The system could then be used on freely moving animals or as a high-density array (5-25 pipettes) in a head-fixed preparation.

6.2.4 Automated Pipette Holder Array for Multipatching

Simultaneous recordings typically require filling, inserting, and positioning between two and thirteen pipettes per attempt which begins to consume a larger percentage of the experiment time per trial. Using automated pipette holders and a precise

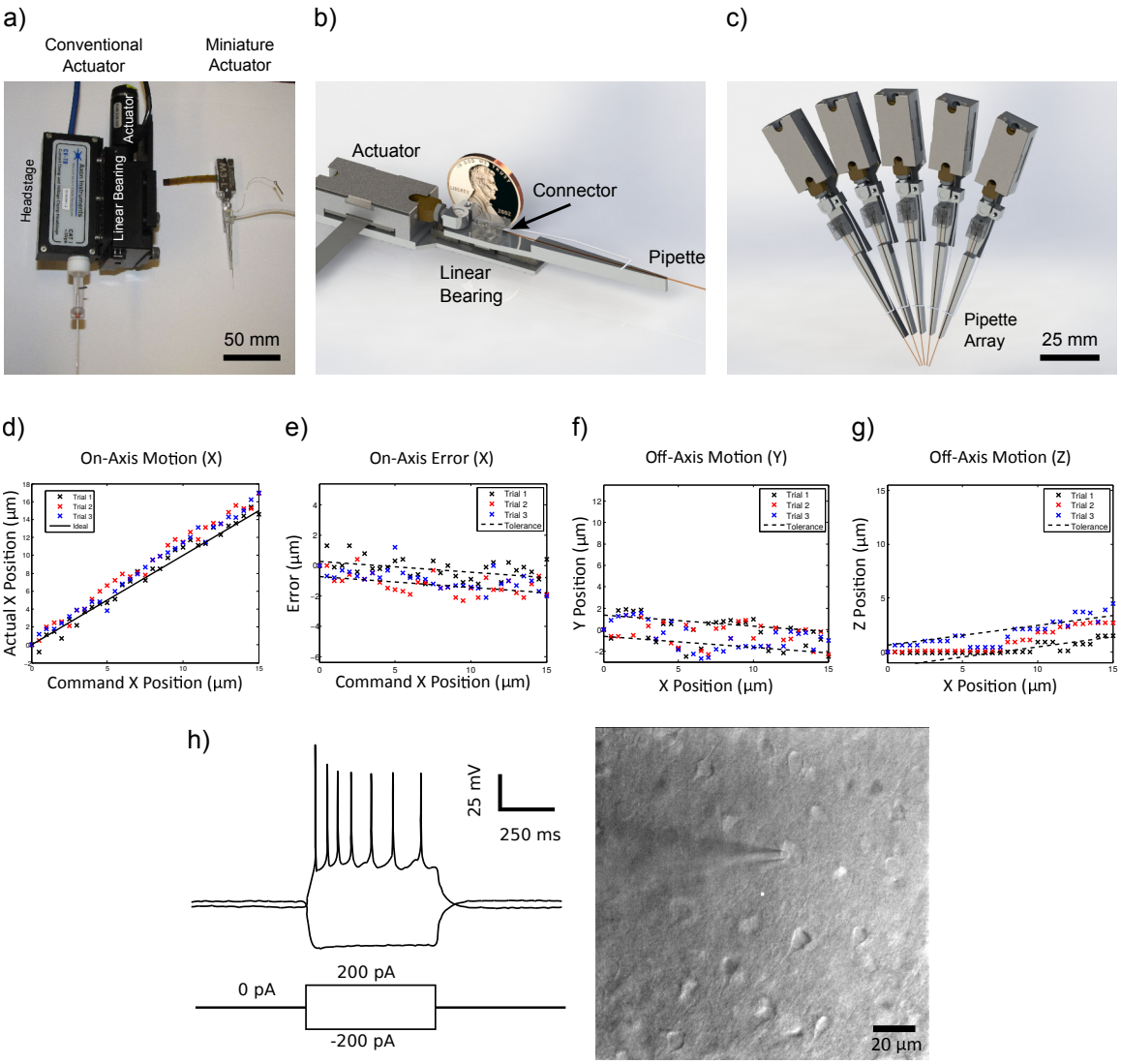

Figure 48: (a) Photograph comparing the conventional autopatcher hardware with the miniaturized actuator and pipette holder design. (b) Detailed rendering of the miniature actuator system. (c) Rendering of a 1D radial array of five miniature actuators. Up to 25 pipettes could be inserted into the same craniotomy with multiple arrays. (d-g) Measurements of precision of the motor and linear bearing. Further miniaturizations would enable freely moving recordings.

pipette handling robot similar to those presented here could significantly reduce the preparation time and push closer to the theoretical limits of the number of possible simultaneous recordings *in vivo*. Figure 49 shows a completed design for a more compact, automated pipette holder with an integrated v-groove, seals, and wire threading mechanism. Pipette change times could be reduced in manual experiments to 3-10 seconds per pipette and would enable automated pipette changes with an automated pipette handling system similar to the one in this work but would require with additional degrees of freedom to orient the pipette properly with respect to the axis of the pipette holder. This could benefit both in vivo and in vitro experimentation.

6.2.5 Integration With Optical Methods

Throughout the design of the fully-automated system, we considered integration with two-photon imaging and *in vitro* systems. These systems have even tighter physical space constraints due to the addition of a microscope objective and supporting optics. The current solutions for manual methods are to rotate or slide the pipette holder away from the recording area to replace pipettes. We designed the pipette holder to have a short pipette insertion distance (4 mm) so that the 3-axis manipulator would be all that is required to insert pipettes. The end effector of the robot arm was also designed to have a minimal footprint for inserting pipettes into these tight spaces. As with the arrays of pipettes mentioned previously, additional rotational degrees of freedom will need to be added to the end of the robot arm to insert pipettes into a holder at the angle required to insert the pipette under the objective. The motors were designed to have sufficient torque to insert pipettes through the o-ring even if positioned horizontally where the insertion force would be entirely provided by the motors rather than the stiffness of the bearings as in the case of vertical insertion. Feedback control of the robot arm joints will likely be necessary in this case so that the position of the pipette can be maintained while the 3-axis manipulator threads

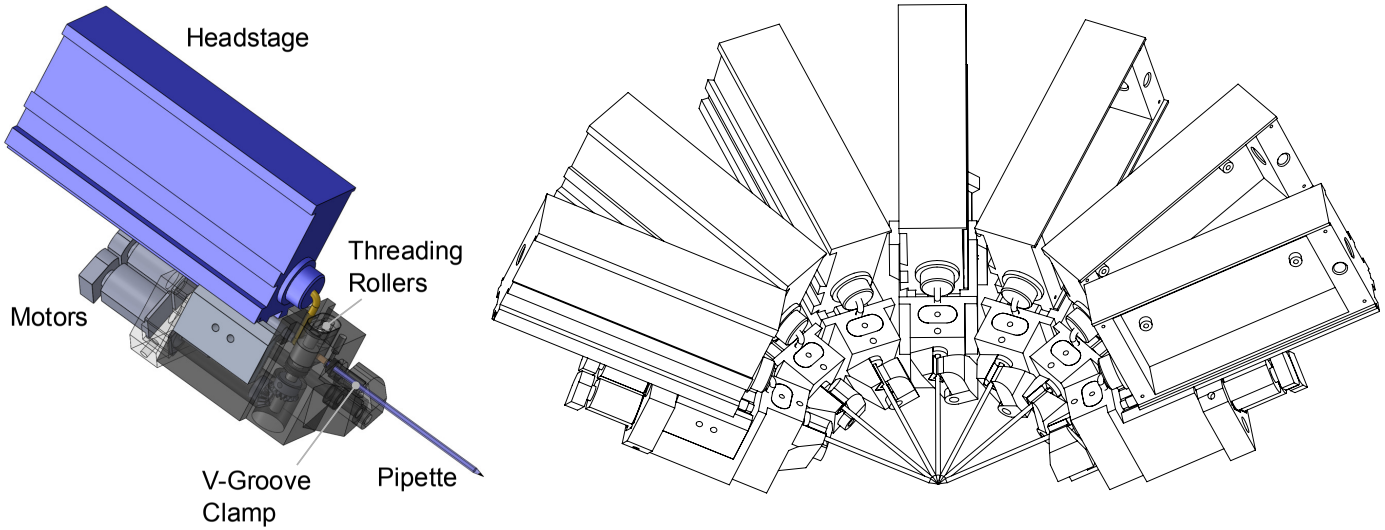

Figure 49: A compact, automated pipette holder (left) designed for high-density arrays (right) for *in vitro* and *in vivo* simultaneous recordings. A total of 13 pipette holders can be arranged radially with a 23° insertion angle relative to the horizontal plane.

the holder (and o-ring) over the pipette.

APPENDIX A

INTERNAL SOLUTION PREPARATION

K Gluconate Internal in mouse, -70 mV E_{Cl}

Current recipe 2012, from Yang Dan's laboratory

To make 50 mL of internal solution:

1. Dissolve items in Table 8 in 40 mL ddH 2 O. pH to 7.30 using 8N KOH (Sigma P4494-50ML).

2. Bring the bulk solution to correct osmolarity: For 0.3% Biocytin internal, or internal with phosphocreatine, make a "LIGHT" internal: QV to 266 mOsm (approx. 47 mL final volume). For normal internal: QV to 271 mOsm (approx. 45-47 mL final volume).

3. Filter the bulk solution using 0.2 um centrifuge filter (**Edit:** optional).

4. Divide into 2.0 mL aliquots in vials with Teflon cap liners and freeze, ok for $\sim$ 2 months. Or, store in bulk in the fridge for $\sim$ 1 mo. (**Edit:** We use 4.0 mL aliquots in cryogenic vials, Globe Scientific Inc., 3015)

5. To use, add the solutes in Table 8 to each 2.0 mL aliquot: (**Edit:** quadruple for 8 mL aliquot)

6. Then, re-pH with KOH to 7.25, and bring the solution to $\sim$ 290 mOsm. Put the solution into 4, 500 µl aliquots and freeze $<$ - 50° C (**Edit:** if making 8 mL, aliquot into 32, 250 µL aliquots in 500 µL centrifuge tubes, Eppendorf 022363611). Thaw one before experiment.

Table 8: Solutes and amounts for preparing 50 mL of stock internal solution.

mM	Compound	MW	g/50 mL	Source
135	K Gluconante	234.2	1.580 g	Fluka #60245, 250 g
10	HEPES	238.31	119 mg	Sigma Ultra H7523-50G
4	KCl	74.5	14.7 mg	Sigma Aldrich #204099-50G
1	EGTA	380.4	20 mg	Sigma E4378-10G

Table 9: Solutes and amounts to be added to 2 mL of stock solution (see Table 8) to prepare the finished internal solution. *if desired. ** It is critical for recording stability and for plasticity that ATP and GTP be absolutely fresh. No older than 1 month. GTP, ATP, phosphocreatine, and biocytin are all stored below -20° C.

mM	Compound	mg/2 mL	Source
0.3	GTP-Na	0.3 mg	Sigma G8877-10MG**
4	ATP-Mg	4.0 mg	Sigma A9187-100MG
10	Na_2-phosphocreatine*	5.1 mg	Sigma P7936-1G
0.66	Alexa Fluor 594 hydrazide	1 mg	Invitrogen A10438
OR			
0.3 %	Biocytin*	6 mg	Tocris 3349

APPENDIX B

VISUAL TUNING PLOTS

(continued on next page)

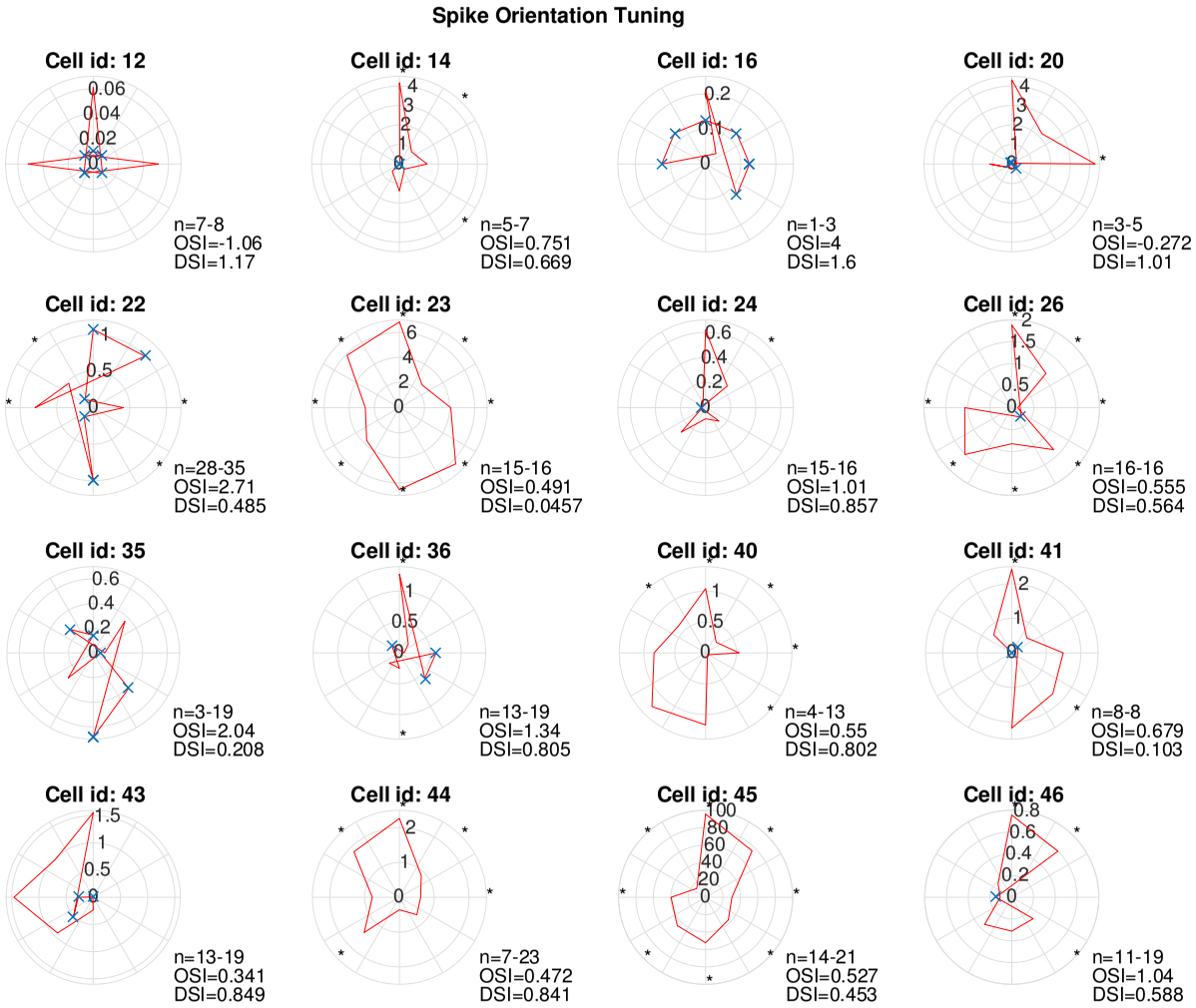

Figure 50: Orientation tuning for the spiking response. The background firing rate was subtracted from all orientations. The X marks responses that fell below the baseline rate (negative). The asterisks mark statistically significant responses ($p<0.05$). Bursting cells are 14, 20, 22, 23, 35, 36, 40, 43, and 44. Regular spiking cells are 12, 24, 26, 41, and 46. Putative interneurons are 16, and 45.

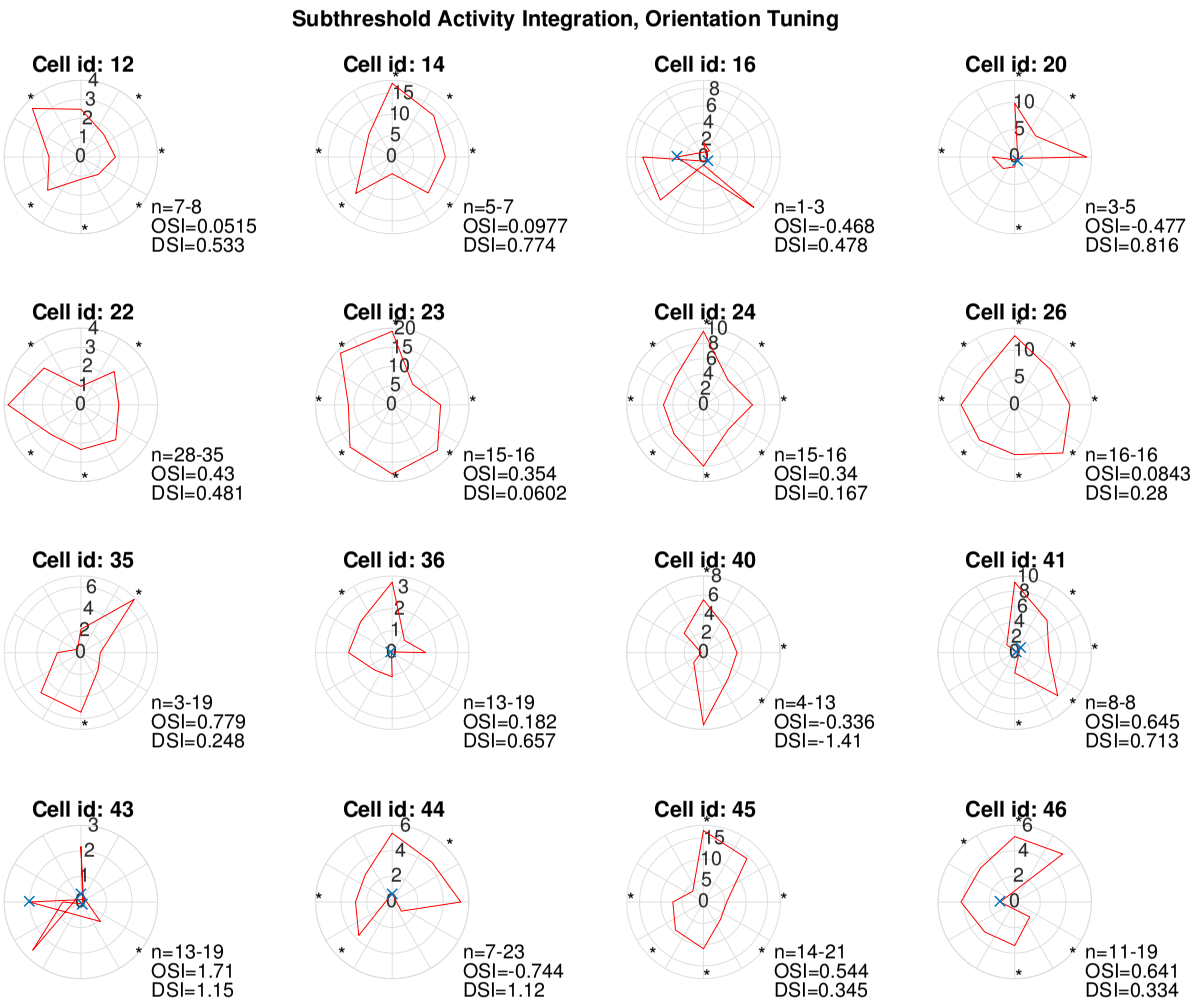

Figure 51: Orientation tuning for the integral of the subthreshold response showing both broad and narrow tuning. The integral was performed relative to the resting membrane potential. The X marks responses below the baseline (negative). The asterisks mark statistically significant responses ($p<0.05$). Bursting cells are 14, 20, 22, 23, 35, 36, 40, 43, and 44. Regular spiking cells are 12, 24, 26, 41, and 46. Putative interneurons are 16, and 45.

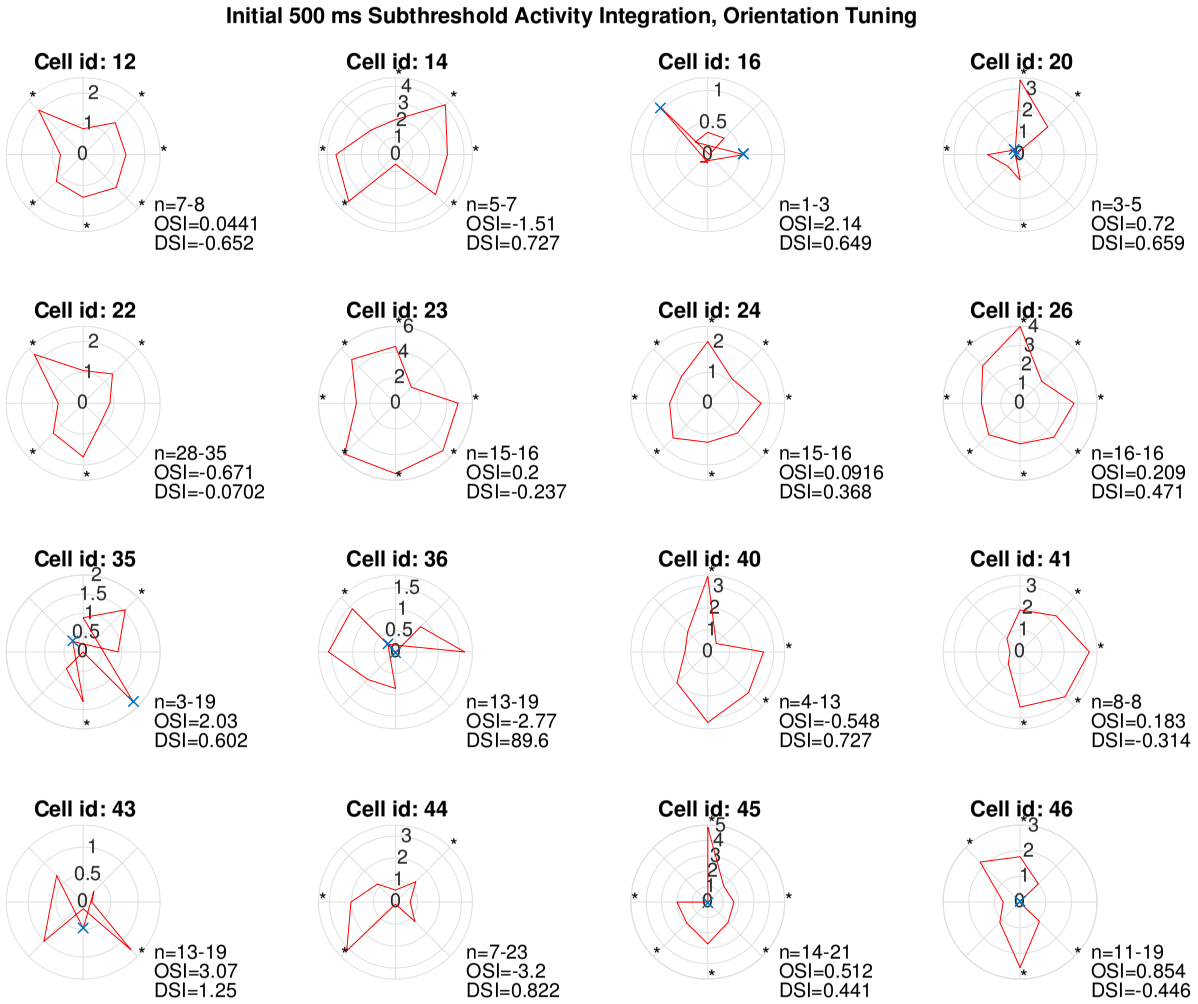

Figure 52: Orientation tuning for the integral of the first 500 ms of subthreshold response after stimulus onset showing broad subthreshold tuning with some narrow tuning. The integral was performed relative to the resting membrane potential and the integral of the 500 ms prior to the onset was subtracted. The X marks responses below the baseline (negative). The asterisks mark statistically significant responses ($p<0.05$). Bursting cells are 14, 20, 22, 23, 35, 36, 40, 43, and 44. Regular spiking cells are 12, 24, 26, 41, and 46. Putative interneurons are 16, and 45.

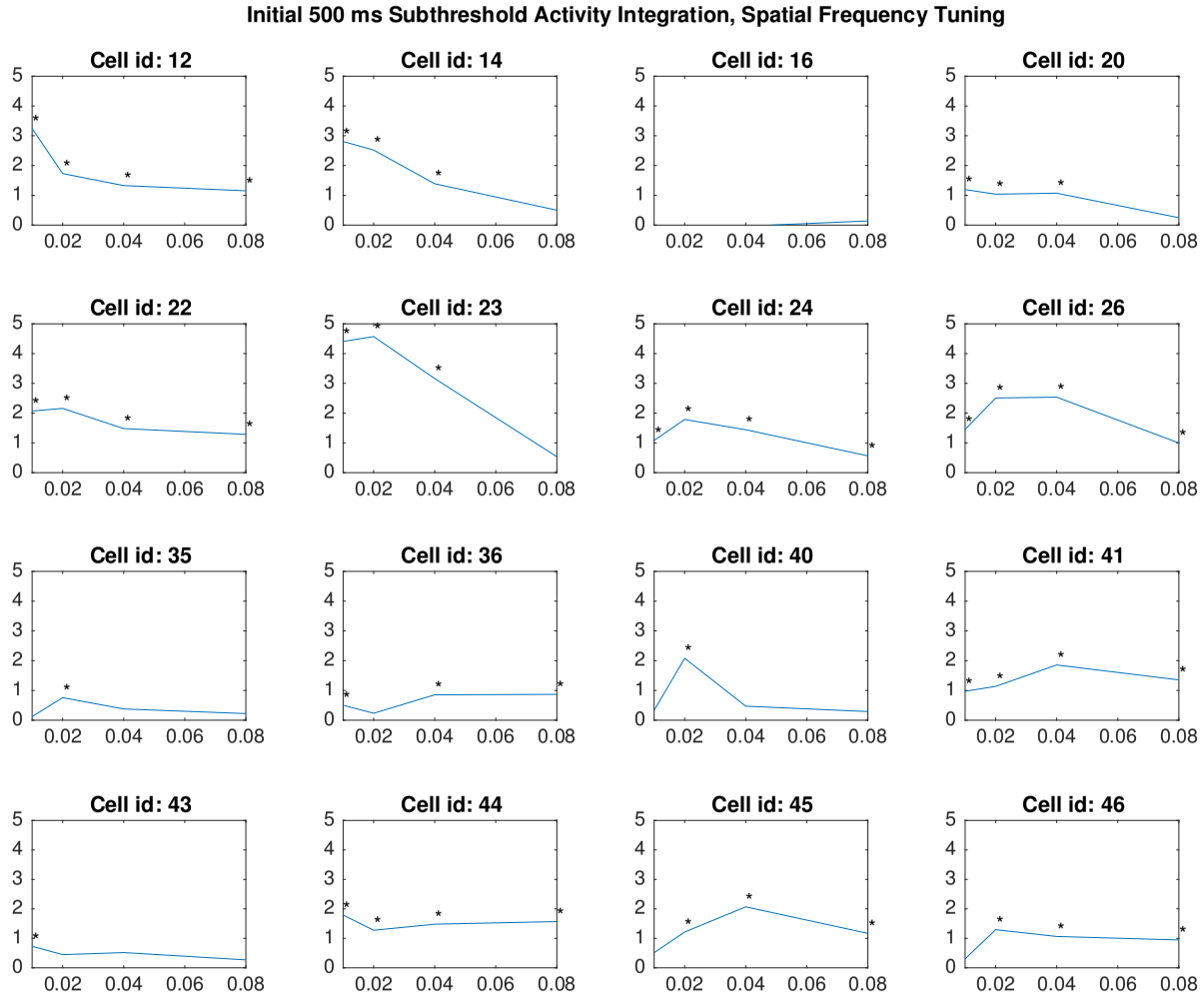

Figure 53: Spatial frequency tuning for the spiking activity showing characteristic low pass or band pass filtering in many cells. The baseline firing rate was subtracted. The X marks responses below the baseline (negative). The asterisks mark statistically significant responses ($p<0.05$). Bursting cells are 14, 20, 22, 23, 35, 36, 40, 43, and 44. Regular spiking cells are 12, 24, 26, 41, and 46. Putative interneurons are 16, and 45.

REFERENCES

[1] "Allen Institute for Brain Science: Allen Cell Types Database," *http://celltypes.brain-map.org/*, 2015.

[2] Abbott, L. F., DePasquale, B., and Memmesheimer, R.-M., "Building functional networks of spiking model neurons," *Nature Neuroscience*, vol. 19, pp. 350–355, Mar. 2016.

[3] Adrian, E. D., "The impulses produced by sensory nerve endings," *The Journal of Physiology*, vol. 61, pp. 49–72, Mar. 1926.

[4] Alivisatos, A. P., Andrews, A. M., Boyden, E. S., Chun, M., Church, G. M., Deisseroth, K., Donoghue, J. P., Fraser, S. E., Lippincott-Schwartz, J., Looger, L. L., Masmanidis, S., McEuen, P. L., Nurmikko, A. V., Park, H., Peterka, D. S., Reid, C., Roukes, M. L., Scherer, A., Schnitzer, M., Sejnowski, T. J., Shepard, K. L., Tsao, D., Turrigiano, G., Weiss, P. S., Xu, C., Yuste, R., and Zhuang, X., "Nanotools for Neuroscience and Brain Activity Mapping," *ACS Nano*, vol. 7, pp. 1850–1866, Mar. 2013.

[5] Alivisatos, A. P., Chun, M., Church, G. M., Deisseroth, K., Donoghue, J. P., Greenspan, R. J., McEuen, P. L., Roukes, M. L., Sejnowski, T. J., Weiss, P. S., and Yuste, R., "The Brain Activity Map," *Science*, vol. 339, pp. 1284–1285, Mar. 2013.

[6] Atallah, B., Bruns, W., Carandini, M., and Scanziani, M., "Parvalbumin-Expressing Interneurons Linearly Transform Cortical Responses to Visual Stimuli," *Neuron*, vol. 73, pp. 159–170, Jan. 2012.

[7] Baker, B. J., Kosmidis, E. K., Vucinic, D., Falk, C. X., Cohen, L. B., Djurisic, M., and Zecevic, D., "Imaging Brain Activity With Voltage- and Calcium-Sensitive Dyes," *Cellular and Molecular Neurobiology*, vol. 25, pp. 245–282, Apr. 2005.

[8] Bammesberger, S., Ernst, A., Losleben, N., Tanguy, L., Zengerle, R., and Koltay, P., "Quantitative characterization of non-contact microdispensing technologies for the sub-microliter range," *Drug Discovery Today*, vol. 18, pp. 435–446, May 2013.

[9] Barker, M., Billups, B., and Hamann, M., "Focal macromolecule delivery in neuronal tissue using simultaneous pressure ejection and local electroporation," *Journal of Neuroscience Methods*, vol. 177, pp. 273–284, Mar. 2009.

[10] Berger, T., Borgdorff, A., Crochet, S., Neubauer, F. B., Lefort, S., Fauvet, B., Ferezou, I., Carleton, A., Luscher, H.-R., and Petersen, C. C. H., "Combined Voltage and Calcium Epifluorescence Imaging In Vitro and In Vivo Reveals Subthreshold and Suprathreshold Dynamics of Mouse Barrel Cortex," *Journal of Neurophysiology*, vol. 97, pp. 3751–3762, Mar. 2007.

[11] Bourassa, J. and Deschenes, M., "Corticothalamic projections from the primary visual cortex in rats: a single fiber study using biocytin as an anterograde tracer," *Neuroscience*, vol. 66, pp. 253–263, May 1995.

[12] Boyden, E. S., Zhang, F., Bamberg, E., Nagel, G., and Deisseroth, K., "Millisecond-timescale, genetically targeted optical control of neural activity," *Nature Neuroscience*, vol. 8, pp. 1263–1268, Sept. 2005.

[13] Brogrdh, T., "Present and future robot control developmentAn industrial perspective," *Annual Reviews in Control*, vol. 31, pp. 69–79, Jan. 2007.

[14] Broussard, G. J., Liang, R., and Tian, L., "Monitoring activity in neural circuits with genetically encoded indicators," *Frontiers in Molecular Neuroscience*, vol. 7, Dec. 2014.

[15] Bruno, R. M. and Sakmann, B., "Cortex is driven by weak but synchronously active thalamocortical synapses," *Science*, vol. 312, no. 5780, pp. 1622–1627, 2006.

[16] Bu, G., Adams, H., Berbari, E. J., and Rubart, M., "Uniform Action Potential Repolarization within the Sarcolemma of In Situ Ventricular Cardiomyocytes," *Biophysical Journal*, vol. 96, pp. 2532–2546, Mar. 2009.

[17] Buzski, G. and Kandel, A., "Somadendritic Backpropagation of Action Potentials in Cortical Pyramidal Cells of the Awake Rat," *Journal of Neurophysiology*, vol. 79, pp. 1587–1591, Mar. 1998.

[18] Cadwell, C. R., Palasantza, A., Jiang, X., Berens, P., Deng, Q., Yilmaz, M., Reimer, J., Shen, S., Bethge, M., Tolias, K. F., Sandberg, R., and Tolias, A. S., "Electrophysiological, transcriptomic and morphologic profiling of single neurons using Patch-seq," *Nature Biotechnology*, vol. 34, pp. 199–203, Feb. 2016.

[19] Carlson, G. C. and Coulter, D. A., "In vitro functional imaging in brain slices using fast voltage-sensitive dye imaging combined with whole-cell patch recording," *Nature Protocols*, vol. 3, pp. 249–255, Jan. 2008.

[20] Chagnac-Amitai, Y., Luhmann, H. J., and Prince, D. A., "Burst generating and regular spiking layer 5 pyramidal neurons of rat neocortex have different morphological features," *Journal of Comparative Neurology*, vol. 296, no. 4, pp. 598–613, 1990.

[21] Chen, R., Romero, G., Christiansen, M. G., Mohr, A., and Anikeeva, P., "Wireless magnetothermal deep brain stimulation," *Science*, p. 1261821, Mar. 2015.

[22] Chen, T.-W., Wardill, T. J., Sun, Y., Pulver, S. R., Renninger, S. L., Baohan, A., Schreiter, E. R., Kerr, R. A., Orger, M. B., Jayaraman, V., Looger, L. L., Svoboda, K., and Kim, D. S., "Ultrasensitive fluorescent proteins for imaging neuronal activity," *Nature*, vol. 499, pp. 295–300, July 2013.

[23] Cottam, J. C. H., Smith, S. L., and Hausser, M., "Target-Specific Effects of Somatostatin-Expressing Interneurons on Neocortical Visual Processing," *Journal of Neuroscience*, vol. 33, pp. 19567–19578, Dec. 2013.

[24] Covey, E. and Carter, M., *Basic Electrophysiological Methods*. Oxford University Press, Incorporated, Mar. 2015.

[25] Covey, E., Kauer, J. A., and Casseday, J. H., "Whole-Cell Patch-Clamp Recording Reveals Subthreshold Sound-Evoked Postsynaptic Currents in the Inferior Colliculus of Awake Bats," *The Journal of Neuroscience*, vol. 16, pp. 3009–3018, May 1996.

[26] de Kock, C. P. J., Bruno, R. M., Spors, H., and Sakmann, B., "Layer- and cell-type-specific suprathreshold stimulus representation in rat primary somatosensory cortex," *The Journal of Physiology*, vol. 581, pp. 139–154, May 2007.

[27] De Kock, C. P. J. and Sakmann, B., "High frequency action potential bursts (100 Hz) in L2/3 and L5b thick tufted neurons in anaesthetized and awake rat primary somatosensory cortex: High frequency bursts in barrel cortex," *The Journal of Physiology*, vol. 586, pp. 3353–3364, July 2008.

[28] Desai, N. S., Siegel, J. J., Taylor, W., Chitwood, R. A., and Johnston, D., "MATLAB-based automated patch-clamp system for awake behaving mice," *Journal of Neurophysiology*, vol. 114, pp. 1331–1345, Aug. 2015.

[29] Destexhe, A., Contreras, D., Steriade, M., Sejnowski, T. J., and Huguenard, J. R., "In vivo, in vitro, and computational analysis of dendritic calcium currents in thalamic reticular neurons," *The Journal of Neuroscience*, vol. 16, pp. 169–185, Jan. 1996.

[30] DeWeese, M. R., "Whole-cell recording in vivo," *Current Protocols in Neuroscience*, vol. Chapter 6, p. Unit 6.22, Jan. 2007.

[31] Dhillon, B. S., *Applied reliability and quality: fundamentals, methods and procedures*. Springer series in reliability engineering, London: Springer, 2007. OCLC: ocm70672607.

[32] Edelstein, A. D., Tsuchida, M. A., Amodaj, N., Pinkard, H., Vale, R. D., and Stuurman, N., "Advanced methods of microscope control using Manager software," *Journal of biological methods*, vol. 1, no. 2, 2014.

[33] Epsztein, J., Brecht, M., and Lee, A., "Intracellular Determinants of Hippocampal CA1 Place and Silent Cell Activity in a Novel Environment," *Neuron*, vol. 70, pp. 109–120, Apr. 2011.

[34] Fee, M. S., "Active Stabilization of Electrodes for Intracellular Recording in Awake Behaving Animals," *Neuron*, vol. 27, pp. 461–468, Sept. 2000.

[35] Flytzanis, N. C., Bedbrook, C. N., Chiu, H., Engqvist, M. K. M., Xiao, C., Chan, K. Y., Sternberg, P. W., Arnold, F. H., and Gradinaru, V., "Archaerhodopsin variants with enhanced voltage-sensitive fluorescence in mammalian and Caenorhabditis elegans neurons," *Nature Communications*, vol. 5, p. 4894, Sept. 2014.

[36] Fraser, D. D. and MacVicar, B. A., "Cholinergic-Dependent Plateau Potential in Hippocampal CA1 Pyramidal Neurons," *The Journal of Neuroscience*, vol. 16, pp. 4113–4128, July 1996.

[37] Frostig, R. D., *In vivo optical imaging of brain function*. CRC press, 2nd ed., 2009.

[38] Garaschuk, O., Linn, J., Eilers, J., and Konnerth, A., "Large-scale oscillatory calcium waves in the immature cortex," *Nature Neuroscience*, vol. 3, pp. 452–459, May 2000.

[39] Gentet, L. J., Avermann, M., Matyas, F., Staiger, J. F., and Petersen, C. C. H., "Membrane Potential Dynamics of GABAergic Neurons in the Barrel Cortex of Behaving Mice," *Neuron*, vol. 65, pp. 422–435, Feb. 2010.

[40] Go, J., Fan, A., Lu, C., Kodandaramaiah, S., Holst, G. L., Stoy, W., Kolb, I., Boyden, E. S., and Forest, C. R., "Fully-automated in vivo single cell electrophysiology," in *Proceedings of the 28th Annual Meeting of the American Society for Precision Engineering*, (St. Paul, MN), Oct. 2013.

[41] Goldberg, J. H., Lacefield, C. O., and Yuste, R., "Global dendritic calcium spikes in mouse layer 5 low threshold spiking interneurones: implications for control of pyramidal cell bursting," *Journal of Physiology*, pp. 465–478, July 2004.

[42] Goodman, M. B. and Lockery, S. R., "Pressure polishing: a method for reshaping patch pipettes during fire polishing," *Journal of Neuroscience Methods*, vol. 100, pp. 13–15, July 2000.

[43] Groh, A., Meyer, H. S., Schmidt, E. F., Heintz, N., Sakmann, B., and Krieger, P., "Cell-Type Specific Properties of Pyramidal Neurons in

Neocortex Underlying a Layout that Is Modifiable Depending on the Cortical Area," *Cerebral Cortex*, vol. 20, pp. 826–836, Apr. 2010.

[44] Gke, O., Bonhoeffer, T., and Scheuss, V., "Clusters of synaptic inputs on dendrites of layer 5 pyramidal cells in mouse visual cortex," *eLife*, vol. 5, p. e09222, 2016.

[45] Hallman, L. E., Schofield, B. R., and Lin, C.-S., "Dendritic morphology and axon collaterals of corticotectal, corticopontine, and callosal neurons in layer V of primary visual cortex of the hooded rat," *The Journal of Comparative Neurology*, vol. 272, pp. 149–160, June 1988.

[46] Hamel, E. O., Grewe, B., Parker, J., and Schnitzer, M., "Cellular Level Brain Imaging in Behaving Mammals: An Engineering Approach," *Neuron*, vol. 86, pp. 140–159, Apr. 2015.

[47] Hamill, O. P., Marty, A., Neher, E., Sakmann, B., and Sigworth, F. J., "Improved patch-clamp techniques for high-resolution current recording from cells and cell-free membrane patches.," *Pflugers Archiv : European journal of physiology*, vol. 391, pp. 85–100, Aug. 1981.

[48] Harrison, R. R., Kolb, I., Kodandaramaiah, S. B., Chubykin, A. A., Yang, A., Bear, M. F., Boyden, E. S., and Forest, C. R., "Microchip amplifier for in vitro, in vivo, and automated whole cell patch-clamp recording," *Journal of Neurophysiology*, vol. 113, pp. 1275–1282, Feb. 2015.

[49] Hattox, A. M. and Nelson, S. B., "Layer V Neurons in Mouse Cortex Projecting to Different Targets Have Distinct Physiological Properties," *Journal of Neurophysiology*, vol. 98, pp. 3330–3340, Oct. 2007.

[50] Haynie, D. T., "Biological Thermodynamics," in *Biological Thermodynamics*, p. 143, Cambridge University Press, Feb. 2008.

[51] Helmchen, F., Svoboda, K., Denk, W., and Tank, D. W., "In vivo dendritic calcium dynamics in deep-layer cortical pyramidal neurons," *Nat Neurosci*, vol. 2, pp. 989–996, Nov. 1999.

[52] Herfst, L., Burgalossi, A., Haskic, K., Tukker, J. J., Schmidt, M., and Brecht, M., "Friction-based stabilization of juxtacellular recordings in freely moving rats," *Journal of Neurophysiology*, vol. 108, pp. 697–707, July 2012.

[53] Hochbaum, D. R., Zhao, Y., Farhi, S. L., Klapoetke, N., Werley, C. A., Kapoor, V., Zou, P., Kralj, J. M., Maclaurin, D., Smedemark-Margulies, N., Saulnier, J. L., Boulting, G. L., Straub, C., Cho, Y. K., Melkonian, M., Wong, G. K.-S., Harrison, D. J., Murthy, V. N., Sabatini, B. L., Boyden, E. S., Campbell, R. E., and Cohen, A. E., "All-optical electrophysiology in mammalian neurons using engineered microbial rhodopsins," *Nature Methods*, vol. 11, pp. 825–833, June 2014.

[54] Hu, H., Gan, J., and Jonas, P., "Fast-spiking, parvalbumin+ GABAergic interneurons: From cellular design to microcircuit function," *Science*, vol. 345, pp. 1255263–1255263, Aug. 2014.

[55] Hbener, M. and Bolz, J., "Morphology of identified projection neurons in layer 5 of rat visual cortex," *Neuroscience Letters*, vol. 94, no. 1-2, pp. 76–81, 1988.

[56] Hbener, M., Schwarz, C., and Bolz, J., "Morphological types of projection neurons in layer 5 of cat visual cortex," *Journal of comparative neurology*, vol. 301, no. 4, pp. 655–674, 1990.

[57] Irwin, R. P. and Allen, C. N., "Simultaneous Electrophysiological Recording and Calcium Imaging of Suprachiasmatic Nucleus Neurons," *Journal of Visualized Experiments*, Dec. 2013.

[58] Jacob, V., Petreanu, L., Wright, N., Svoboda, K., and Fox, K., "Regular Spiking and Intrinsic Bursting Pyramidal Cells Show Orthogonal Forms of Experience-Dependent Plasticity in Layer V of Barrel Cortex," *Neuron*, vol. 73, pp. 391–404, Jan. 2012.

[59] Jiang, G., Wang, X., Wang, Z., and Liu, H., "Wheat rows detection at the early growth stage based on Hough transform and vanishing point," *Computers and Electronics in Agriculture*, vol. 123, pp. 211–223, Apr. 2016.

[60] Jin, L., Han, Z., Platisa, J., Wooltorton, J. A., Cohen, L., and Pieribone, V., "Single Action Potentials and Subthreshold Electrical Events Imaged in Neurons with a Fluorescent Protein Voltage Probe," *Neuron*, vol. 75, pp. 779–785, Sept. 2012.

[61] Kamondi, A., Acsdy, L., and Buzski, G., "Dendritic Spikes Are Enhanced by Cooperative Network Activity in the Intact Hippocampus," *The Journal of Neuroscience*, vol. 18, pp. 3919–3928, May 1998.

[62] Kampa, B. M., Letzkus, J. J., and Stuart, G. J., "Requirement of dendritic calcium spikes for induction of spike-timing-dependent synaptic plasticity: Dendritic spikes controlling STDP," *The Journal of Physiology*, vol. 574, pp. 283–290, July 2006.

[63] Kasper, E. M., Larkman, A. U., Lbke, J., and Blakemore, C., "Pyramidal neurons in layer 5 of the rat visual cortex. I. Correlation among cell morphology, intrinsic electrophysiological properties, and axon targets," *Journal of Comparative Neurology*, vol. 339, no. 4, pp. 459–474, 1994.

[64] Kerlin, A. M., Andermann, M. L., Berezovskii, V. K., and Reid, R. C., "Broadly Tuned Response Properties of Diverse Inhibitory Neuron Subtypes in Mouse Visual Cortex," *Neuron*, vol. 67, pp. 858–871, Sept. 2010.

[65] Kim, E., Juavinett, A., Kyubwa, E., Jacobs, M., and Callaway, E., "Three Types of Cortical Layer 5 Neurons That Differ in Brain-wide Connectivity and Function," *Neuron*, vol. 88, pp. 1253–1267, Dec. 2015.

[66] Kim, J., Matney, C. J., Blankenship, A., Hestrin, S., and Brown, S. P., "Layer 6 Corticothalamic Neurons Activate a Cortical Output Layer, Layer 5a," *Journal of Neuroscience*, vol. 34, pp. 9656–9664, July 2014.

[67] Kitamura, K., Judkewitz, B., Kano, M., Denk, W., and Husser, M., "Targeted patch-clamp recordings and single-cell electroporation of unlabeled neurons in vivo," *Nature Methods*, vol. 5, pp. 61–67, Jan. 2008.

[68] Kodandaramaiah, S. B., Flores, F. J., Holst, G. L., Wickersham, I. R., Brown, E. N., Forest, C. R., and Boyden, E. S., "Multipatcher: A Robot for High Density Measurement of Intracellular Recordings In Vivo," in *Proceedings of the Annual Meeting of the Biomedical Engineering Society (BMES) 2014*, (San Antonio, TX), Oct. 2014.

[69] Kodandaramaiah, S. B., Franzesi, G. T., Chow, B. Y., Boyden, E. S., and Forest, C. R., "Automated whole-cell patch-clamp electrophysiology of neurons in vivo," *Nature Methods*, vol. 9, pp. 585–587, May 2012.

[70] Kodandaramaiah, S. B., Holst, G. L., Wickersham, I. R., Singer, A. C., Franzesi, G. T., McKinnon, M. L., Forest, C. R., and Boyden, E. S., "Assembly and operation of the autopatcher for automated intracellular neural recording in vivo," *Nature Protocols*, vol. 11, pp. 634–654, Mar. 2016.

[71] Koga, K., Li, X., Chen, T., Steenland, H. W., Descalzi, G., and Zhuo, M., "In vivo whole-cell patch-clamp recording of sensory synaptic responses of cingulate pyramidal neurons to noxious mechanical stimuli in adult mice," *Molecular Pain*, vol. 6, p. 62, Sept. 2010.

[72] Kolb, I., Stoy, W. A., Rousseau, E. B., Moody, O. A., Jenkins, A., and Forest, C. R., "Cleaning patch-clamp pipettes for immediate reuse," *Scientific Reports*, vol. 6, p. 35001, Oct. 2016.

[73] Kolb, I., Holst, G. L., Kodandaramaiah, S. B., Stoy, W., Boyden, E. S., and Forest, C. R., "Linear Micro-Actuation System for Patch-Clamp Recording," in *Proceedings of the 29th Annual Meeting of the American Society for Precision Engineering*, (Boston, MA), Nov. 2014.

[74] Komai, S., Denk, W., Osten, P., Brecht, M., and Margrie, T. W., "Two-photon targeted patching (TPTP) in vivo," *Nature Protocols*, vol. 1, pp. 647–652, July 2006.

[75] Krahe, R. and Gabbiani, F., "Burst firing in sensory systems," *Nature Reviews Neuroscience*, vol. 5, pp. 13–23, Jan. 2004.

[76] Kutchinsky, J., Friis, S., Asmild, M., Taboryski, R., Pedersen, S., Vestergaard, R. K., Jacobsen, R. B., Krzywkowski, K., Schrder, R. L., Ljungstrm, T., Hlix, N., Srensen, C. B., Bech, M., and Willumsen, N. J., "Characterization of Potassium Channel Modulators with QPatch Automated Patch-Clamp Technology: System Characteristics and Performance," *ASSAY and Drug Development Technologies*, vol. 1, pp. 685–693, Oct. 2003.

[77] Larkum, M. E., Kaiser, K. M. M., and Sakmann, B., "Calcium electrogenesis in distal apical dendrites of layer 5 pyramidal cells at a critical frequency of back-propagating action potentials," *Proceedings of the National Academy of Sciences*, vol. 96, no. 25, pp. 14600–14604, 1999.

[78] Larkum, M. E. and Zhu, J. J., "Signaling of layer 1 and whisker-evoked Ca2+ and Na+ action potentials in distal and terminal dendrites of rat neocortical pyramidal neurons in vitro and in vivo," *The Journal of neuroscience*, vol. 22, no. 16, pp. 6991–7005, 2002.

[79] Lee, A. K., Manns, I. D., Sakmann, B., and Brecht, M., "Whole-Cell Recordings in Freely Moving Rats," *Neuron*, vol. 51, pp. 399–407, Aug. 2006.

[80] Lee, D., Shtengel, G., Osborne, J. E., and Lee, A. K., "Anesthetized- and awake-patched whole-cell recordings in freely moving rats using UV-cured collar-based electrode stabilization," *Nature Protocols*, vol. 9, pp. 2784–2795, Nov. 2014.

[81] Lein, E. S., Hawrylycz, M. J., Ao, N., Ayres, M., Bensinger, A., Bernard, A., Boe, A. F., Boguski, M. S., Brockway, K. S., Byrnes, E. J., Chen, L., Chen, L., Chen, T.-M., Chi Chin, M., Chong, J., Crook, B. E., Czaplinska, A., Dang, C. N., Datta, S., Dee, N. R., Desaki, A. L., Desta, T., Diep, E., Dolbeare, T. A., Donelan, M. J., Dong, H.-W., Dougherty, J. G., Duncan, B. J., Ebbert, A. J., Eichele, G., Estin, L. K., Faber, C., Facer, B. A., Fields, R., Fischer, S. R., Fliss, T. P., Frensley, C., Gates, S. N., Glattfelder, K. J., Halverson, K. R., Hart, M. R., Hohmann, J. G., Howell, M. P., Jeung, D. P., Johnson, R. A., Karr, P. T., Kawal, R., Kidney, J. M., Knapik, R. H., Kuan, C. L., Lake, J. H., Laramee, A. R., Larsen, K. D., Lau, C., Lemon, T. A., Liang, A. J., Liu, Y., Luong, L. T., Michaels, J., Morgan, J. J., Morgan, R. J., Mortrud, M. T., Mosqueda, N. F., Ng, L. L., Ng, R., Orta, G. J., Overly, C. C., Pak, T. H., Parry, S. E., Pathak, S. D., Pearson, O. C., Puchalski, R. B., Riley, Z. L., Rockett, H. R., Rowland, S. A., Royall, J. J., Ruiz, M. J., Sarno, N. R., Schaffnit, K., Shapovalova, N. V., Sivisay, T., Slaughterbeck, C. R., Smith, S. C., Smith, K. A., Smith, B. I., Sodt, A. J., Stewart, N. N., Stumpf, K.-R., Sunkin, S. M., Sutram, M., Tam, A., Teemer, C. D., Thaller, C., Thompson, C. L., Varnam, L. R., Visel, A., Whitlock, R. M., Wohnoutka, P. E., Wolkey,

C. K., Wong, V. Y., Wood, M., Yaylaoglu, M. B., Young, R. C., Youngstrom, B. L., Feng Yuan, X., Zhang, B., Zwingman, T. A., and Jones, A. R., "Genome-wide atlas of gene expression in the adult mouse brain," *Nature*, vol. 445, pp. 168–176, Jan. 2007.

[82] Lewicki, M. S., "A review of methods for spike sorting: the detection and classification of neural action potentials," *Network: Computation in Neural Systems*, vol. 9, pp. R53–R78, Jan. 1998.

[83] Li, W.-C., "A Direct Comparison of Whole Cell Patch and Sharp Electrodes by Simultaneous Recording From Single Spinal Neurons in Frog Tadpoles," *Journal of Neurophysiology*, vol. 92, pp. 380–386, Mar. 2004.

[84] Li, Y.-t., Ma, W.-p., Li, L.-y., Ibrahim, L. A., Wang, S.-z., and Tao, H. W., "Broadening of Inhibitory Tuning Underlies Contrast-Dependent Sharpening of Orientation Selectivity in Mouse Visual Cortex," *Journal of Neuroscience*, vol. 32, pp. 16466–16477, Nov. 2012.

[85] Li, Y.-t., Liu, B.-h., Chou, X.-l., Zhang, L. I., and Tao, H. W., "Strengthening of Direction Selectivity by Broadly Tuned and Spatiotemporally Slightly Offset Inhibition in Mouse Visual Cortex," *Cerebral Cortex*, vol. 25, pp. 2466–2477, Sept. 2015.

[86] Lien, A. D. and Scanziani, M., "Tuned thalamic excitation is amplified by visual cortical circuits," *Nature Neuroscience*, vol. 16, pp. 1315–1323, Aug. 2013.

[87] Lin, D., Loveall, B., Ewer, J., Deitcher, D., and Sucher, N., "Characterization of mRNA Expression in Single Neurons," in *Neuroprotection Methods and Protocols* (Borsello, T., ed.), no. 399 in Methods in Molecular Biology, pp. 133–152, Humana Press, Jan. 2007. DOI: 10.1007/978-1-59745-504-6_10.

[88] Lin, R. J., Bettencourt, J., White, J. A., Christini, D. J., and Butera, R. J., "Real-time Experiment Interface for biological control applications," in *2010 Annual International Conference of the IEEE Engineering in Medicine and Biology*, pp. 4160–4163, Aug. 2010.

[89] Lisman, J. E., "Bursts as a unit of neural information: making unreliable synapses reliable," *Trends in Neurosciences*, vol. 20, pp. 38–43, Jan. 1997.

[90] Livingstone, M. S., Freeman, D. C., and Hubel, D. H., "Visual Responses in V1 of Freely Viewing Monkeys," *Cold Spring Harbor Symposia on Quantitative Biology*, vol. 61, pp. 27–37, Jan. 1996.

[91] Llinas, R. and Sugimori, M., "Electrophysiological properties of in vitro Purkinje cell somata in mammalian cerebellar slices.," *The Journal of Physiology*, vol. 305, p. 171, 1980.

[92] Llins, R. and Sugimori, M., "Electrophysiological properties of in vitro Purkinje cell dendrites in mammalian cerebellar slices.," *The Journal of Physiology*, vol. 305, pp. 197–213, Aug. 1980.

[93] Long, M. A. and Lee, A. K., "Intracellular recording in behaving animals," *Current Opinion in Neurobiology*, vol. 22, pp. 34–44, Feb. 2012.

[94] Lupica, C. R., Bell, J. A., Hoffman, A. F., and Watson, P. L., "Contribution of the hyperpolarization-activated current (I h) to membrane potential and GABA release in hippocampal interneurons," *Journal of Neurophysiology*, vol. 86, no. 1, pp. 261–268, 2001.

[95] Lur, G., Vinck, M., Tang, L., Cardin, J., and Higley, M., "Projection-Specific Visual Feature Encoding by Layer 5 Cortical Subnetworks," *Cell Reports*, vol. 14, pp. 2538–2545, Mar. 2016.

[96] Ma, W.-p., Liu, B.-h., Li, Y.-t., Josh Huang, Z., Zhang, L. I., and Tao, H. W., "Visual Representations by Cortical Somatostatin Inhibitory Neurons–Selective But with Weak and Delayed Responses," *Journal of Neuroscience*, vol. 30, pp. 14371–14379, Oct. 2010.

[97] Ma, Y., "Distinct Subtypes of Somatostatin-Containing Neocortical Interneurons Revealed in Transgenic Mice," *Journal of Neuroscience*, vol. 26, pp. 5069–5082, May 2006.

[98] Magee, J. C. and Cook, E. P., "Somatic EPSP amplitude is independent of synapse location in hippocampal pyramidal neurons," *Nature neuroscience*, vol. 3, no. 9, pp. 895–903, 2000.

[99] Malboubi, M. and Jiang, K., *Gigaseal Formation in Patch Clamping: With Applications of Nanotechnology*. Springer Science & Business Media, July 2013. Google-Books-ID: 3KzBBAAAQBAJ.

[100] Margrie, T., Brecht, M., and Sakmann, B., "In vivo, low-resistance, whole-cell recordings from neurons in the anaesthetized and awake mammalian brain," *Pflgers Archiv European Journal of Physiology*, vol. 444, pp. 491–498, July 2002.

[101] McCormick, D., Connors, B., Lighthall, J., and Prince, D., "Comparative electrophysiology of pyramidal and sparsely spiny stellate neurons of the neocortex," *Journal of Neurophysiology*, vol. 54, no. 4, pp. 782–806, 1985.

[102] McElduff, F., Cortina-Borja, M., Chan, S.-K., and Wade, A., "When t-tests or Wilcoxon-Mann-Whitney tests won't do," *Advances in Physiology Education*, vol. 34, pp. 128–133, Sept. 2010.

[103] Miyawaki, A., Llopis, J., Heim, R., McCaffery, J. M., Adams, J. A., Ikura, M., and Tsien, R. Y., "Fluorescent indicators for Ca2+ based on

green fluorescent proteins and calmodulin," *Nature*, vol. 388, no. 6645, pp. 882–887, 1997.

[104] Molecular, D., *pClamp 10 User's Guide*. 2006.

[105] Molleman, A., *Patch Clamping: An Introductory Guide to Patch Clamp Electrophysiology*. John Wiley & Sons, June 2003. Google-Books-ID: JBY9NUsq2DkC.

[106] Muoz, W., Tremblay, R., and Rudy, B., "Channelrhodopsin-Assisted Patching: InVivo Recording of Genetically and Morphologically Identified Neurons throughout the Brain," *Cell Reports*, vol. 9, pp. 2304–2316, Dec. 2014.

[107] Naka, A. and Adesnik, H., "Inhibitory Circuits in Cortical Layer 5," *Frontiers in Neural Circuits*, vol. 10, May 2016.

[108] Nakai, J., Ohkura, M., and Imoto, K., "A high signal-to-noise Ca2+ probe composed of a single green fluorescent protein," *Nat Biotech*, vol. 19, pp. 137–141, Feb. 2001.

[109] Nevian, T., Larkum, M. E., Polsky, A., and Schiller, J., "Properties of basal dendrites of layer 5 pyramidal neurons: a direct patch-clamp recording study," *Nature Neuroscience*, vol. 10, pp. 206–214, Feb. 2007.

[110] Oh, S. W., Harris, J. A., Ng, L., Winslow, B., Cain, N., Mihalas, S., Wang, Q., Lau, C., Kuan, L., Henry, A. M., Mortrud, M. T., Ouellette, B., Nguyen, T. N., Sorensen, S. A., Slaughterbeck, C. R., Wakeman, W., Li, Y., Feng, D., Ho, A., Nicholas, E., Hirokawa, K. E., Bohn, P., Joines, K. M., Peng, H., Hawrylycz, M. J., Phillips, J. W., Hohmann, J. G., Wohnoutka, P., Gerfen, C. R., Koch, C., Bernard, A., Dang, C., Jones, A. R., and Zeng, H., "A mesoscale connectome of the mouse brain," *Nature*, vol. 508, pp. 207–214, Apr. 2014.

[111] Okun, M., Naim, A., and Lampl, I., "The Subthreshold Relation between Cortical Local Field Potential and Neuronal Firing Unveiled by Intracellular Recordings in Awake Rats," *Journal of Neuroscience*, vol. 30, pp. 4440–4448, Mar. 2010.

[112] Oswald, A.-M. M., "Parallel Processing of Sensory Input by Bursts and Isolated Spikes," *Journal of Neuroscience*, vol. 24, pp. 4351–4362, May 2004.

[113] Oativia, J., Schultz, S. R., and Dragotti, P. L., "A finite rate of innovation algorithm for fast and accurate spike detection from two-photon calcium imaging," *Journal of Neural Engineering*, vol. 10, no. 4, p. 046017, 2013.

[114] Pak, N., Siegle, J. H., Kinney, J. P., Denman, D. J., Blanche, T. J., and Boyden, E. S., "Closed-loop, ultraprecise, automated craniotomies," *Journal of Neurophysiology*, vol. 113, pp. 3943–3953, June 2015.

[115] Pala, A. and Petersen, C., "In Vivo Measurement of Cell-Type-Specific Synaptic Connectivity and Synaptic Transmission in Layer 2/3 Mouse Barrel Cortex," *Neuron*, vol. 85, pp. 68–75, Jan. 2015.

[116] Perin, R. and Markram, H., "A Computer-assisted Multi-electrode Patch-clamp System," *Journal of Visualized Experiments*, Oct. 2013.

[117] Petersen, C. C. H., Grinvald, A., and Sakmann, B., "Spatiotemporal Dynamics of Sensory Responses in Layer 2/3 of Rat Barrel Cortex Measured In Vivo by Voltage-Sensitive Dye Imaging Combined with Whole-Cell Voltage Recordings and Neuron Reconstructions," *The Journal of Neuroscience*, vol. 23, pp. 1298–1309, Feb. 2003.

[118] Piccolino, M., "Luigi Galvani and animal electricity: two centuries after the foundation of electrophysiology," *Trends in Neurosciences*, vol. 20, pp. 443–448, Oct. 1997.

[119] Popovic, M. A., Carnevale, N., Rozsa, B., and Zecevic, D., "Electrical behaviour of dendritic spines as revealed by voltage imaging," *Nature Communications*, vol. 6, p. 8436, Oct. 2015.

[120] Potez, S. and Larkum, M. E., "Effect of Common Anesthetics on Dendritic Properties in Layer 5 Neocortical Pyramidal Neurons," *Journal of Neurophysiology*, vol. 99, pp. 1394–1407, Jan. 2008.

[121] Purves, D., ed., *Neuroscience*. Sunderland, Mass: Sinauer Associates, Publishers, 3rd ed ed., 2004.

[122] Rancz, E. A., Franks, K. M., Schwarz, M. K., Pichler, B., Schaefer, A. T., and Margrie, T. W., "Transfection via whole-cell recording in vivo: bridging single-cell physiology, genetics and connectomics," *Nature Neuroscience*, vol. 14, pp. 527–532, Apr. 2011.

[123] Renshaw, B., Forbes, A., and Morison, B. R., "Activity of Isocortex and Hippocampus: Electrical Studies with Micro-Electrodes," *Journal of Neurophysiology*, vol. 3, pp. 74–105, Jan. 1940.

[124] Royer, S., Zemelman, B. V., Losonczy, A., Kim, J., Chance, F., Magee, J. C., and Buzski, G., "Control of timing, rate and bursts of hippocampal place cells by dendritic and somatic inhibition," *Nature Neuroscience*, vol. 15, pp. 769–775, Mar. 2012.

[125] Rudy, B. and McBain, C. J., "Kv3 channels: voltage-gated K+ channels designed for high-frequency repetitive firing," *Trends in neurosciences*, vol. 24, no. 9, pp. 517–526, 2001.

[126] Sakmann, B. and Neher, E., "Patch Clamp Techniques for Studying Ionic Channels in Excitable Membranes," *Annual Review of Physiology*, vol. 46, no. 1, pp. 455–472, 1984.

[127] Scholvin, J., Kinney, J. P., Bernstein, J. G., Moore-Kochlacs, C., Kopell, N., Fonstad, C. G., and Boyden, E. S., "Close-Packed Silicon Microelectrodes for Scalable Spatially Oversampled Neural Recording," *IEEE Transactions on Biomedical Engineering*, vol. 63, pp. 120–130, Jan. 2016.

[128] Schwarz, D. A., Lebedev, M. A., Hanson, T. L., Dimitrov, D. F., Lehew, G., Meloy, J., Rajangam, S., Subramanian, V., Ifft, P. J., Li, Z., Ramakrishnan, A., Tate, A., Zhuang, K. Z., and Nicolelis, M. A. L., "Chronic, wireless recordings of large-scale brain activity in freely moving rhesus monkeys," *Nature Methods*, vol. 11, pp. 670–676, June 2014.

[129] Shai, A. S., Anastassiou, C. A., Larkum, M. E., and Koch, C., "Physiology of layer 5 pyramidal neurons in mouse primary visual cortex: coincidence detection through bursting," *PLoS Comput Biol*, vol. 11, no. 3, p. e1004090, 2015.

[130] Sherman-Gold, R., *The Axon Guide for Electrophysiology & Biophysics: Laboratory Techniques*. Axon Instruments, 1993.

[131] Sigworth, F. J., "Design of the EPC-9, a computer-controlled patch-clamp amplifier. 1. Hardware," *Journal of Neuroscience Methods*, vol. 56, pp. 195–202, Feb. 1995.

[132] Sigworth, F. J., Affolter, H., and Neher, E., "Design of the EPC-9, a computer-controlled patch-clamp amplifier. 2. Software," *Journal of Neuroscience Methods*, vol. 56, pp. 203–215, Feb. 1995.

[133] Stevenson, I. H. and Kording, K. P., "How advances in neural recording affect data analysis," *Nature Neuroscience*, vol. 14, pp. 139–142, Feb. 2011.

[134] Stockslager, M. A., Capocasale, C. M., Holst, G. L., Simon, M. D., Li, Y., McGruder, D. J., Rousseau, E. B., Stoy, W. A., Sulchek, T., and Forest, C. R., "Optical method for automated measurement of glass micropipette tip geometry," *Precision Engineering*, vol. 46, pp. 88–95, Oct. 2016.

[135] Stosiek, C., Garaschuk, O., Holthoff, K., and Konnerth, A., "In vivo two-photon calcium imaging of neuronal networks," *Proceedings of the National Academy of Sciences*, vol. 100, pp. 7319–7324, June 2003.

[136] Stuart, G., Spruston, N., Sakmann, B., and Husser, M., "Action potential initiation and backpropagation in neurons of the mammalian CNS," *Trends in neurosciences*, vol. 20, no. 3, pp. 125–131, 1997.

[137] Suchyna, T. M., Markin, V. S., and Sachs, F., "Biophysics and Structure of the Patch and the Gigaseal," *Biophysical Journal*, vol. 97, pp. 738–747, Aug. 2009.

[138] Sulzer, D., Joyce, M. P., Lin, L., Geldwert, D., Haber, S. N., Hattori, T., and Rayport, S., "Dopamine neurons make glutamatergic synapses in vitro," *The Journal of neuroscience*, vol. 18, no. 12, pp. 4588–4602, 1998.

[139] Sun, Y. J., Kim, Y.-J., Ibrahim, L. A., Tao, H. W., and Zhang, L. I., "Synaptic Mechanisms Underlying Functional Dichotomy between Intrinsic-Bursting and Regular-Spiking Neurons in Auditory Cortical Layer 5," *Journal of Neuroscience*, vol. 33, pp. 5326–5339, Mar. 2013.

[140] Suter, B. A., O'Connor, T., Iyer, V., Petreanu, L. T., Hooks, B. M., Kiritani, T., Svoboda, K., and Shepherd, G. M. G., "Ephus: Multipurpose Data Acquisition Software for Neuroscience Experiments," *Frontiers in Neural Circuits*, vol. 4, Aug. 2010.

[141] Suzuki, T., Kodama, S., Hoshino, C., Izumi, T., and Miyakawa, H., "A plateau potential mediated by the activation of extrasynaptic NMDA receptors in rat hippocampal CA1 pyramidal neurons," *European Journal of Neuroscience*, vol. 28, no. 3, pp. 521–534, 2008.

[142] Swindells, B., "Centenary of the Convention of the Metre," *Platinum Metals Review*, vol. 19, pp. 110–113, July 1975.

[143] Tan, A. Y. Y., Chen, Y., Scholl, B., Seidemann, E., and Priebe, N. J., "Sensory stimulation shifts visual cortex from synchronous to asynchronous states," *Nature*, vol. 509, pp. 226–229, May 2014.

[144] Tasic, B., Menon, V., Nguyen, T. N., Kim, T. K., Jarsky, T., Yao, Z., Levi, B., Gray, L. T., Sorensen, S. A., Dolbeare, T., Bertagnolli, D., Goldy, J., Shapovalova, N., Parry, S., Lee, C., Smith, K., Bernard, A., Madisen, L., Sunkin, S. M., Hawrylycz, M., Koch, C., and Zeng, H., "Adult mouse cortical cell taxonomy revealed by single cell transcriptomics," *Nature Neuroscience*, vol. 19, pp. 335–346, Feb. 2016.

[145] Tsiola, A., Hamzei-Sichani, F., Peterlin, Z., and Yuste, R., "Quantitative morphologic classification of layer 5 neurons from mouse primary visual cortex," *The Journal of Comparative Neurology*, vol. 461, pp. 415–428, July 2003.

[146] Vreeswijk, C. v. and Sompolinsky, H., "Chaos in Neuronal Networks with Balanced Excitatory and Inhibitory Activity," *Science*, vol. 274, pp. 1724–1726, Dec. 1996.

[147] Vlez-Fort, M., Rousseau, C., Niedworok, C., Wickersham, I., Rancz, E., Brown, A., Strom, M., and Margrie, T., "The Stimulus Selectivity and Connectivity of Layer Six Principal Cells Reveals Cortical Microcircuits Underlying Visual Processing," *Neuron*, vol. 83, pp. 1431–1443, Sept. 2014.

[148] Walz, W., ed., *Patch-Clamp Analysis: Advanced Techniques*. Humana Press, softcover reprint of hardcover 2nd ed. 2007 edition ed., Nov. 2010.

[149] Waters, J., Schaefer, A., and Sakmann, B., "Backpropagating action potentials in neurones: measurement, mechanisms and potential functions," *Progress in Biophysics and Molecular Biology*, vol. 87, pp. 145–170, Jan. 2005.

[150] Wilson, C. J. and Park, M. R., "Capacitance compensation and bridge balance adjustment in intracellular recording from dendritic neurons," *Journal of Neuroscience Methods*, vol. 27, pp. 51–75, Feb. 1989.

[151] Woodbury, C. P., "Biochemistry for the Pharmaceutical Sciences," in *Biochemistry for the Pharmaceutical Sciences*, p. 211, Jones & Bartlett Publishers, Mar. 2011. Google-Books-ID: 40Phuq2tw8UC.

[152] Xu, H., Jeong, H.-Y., Tremblay, R., and Rudy, B., "Neocortical Somatostatin-Expressing GABAergic Interneurons Disinhibit the Thalamorecipient Layer 4," *Neuron*, vol. 77, pp. 155–167, Jan. 2013.

[153] Xue, S., Gong, H., Jiang, T., Luo, W., Meng, Y., Liu, Q., Chen, S., and Li, A., "Indian-Ink Perfusion Based Method for Reconstructing Continuous Vascular Networks in Whole Mouse Brain," *PLoS ONE*, vol. 9, p. e88067, Jan. 2014.

[154] Zarrinpar, A. and Callaway, E. M., "Functional Local Input to Layer 5 Pyramidal Neurons in the Rat Visual Cortex," *Cerebral Cortex*, vol. 26, pp. 991–1003, Mar. 2016.